Growth and Characterization of $Cu_2ZnSn(SSe)_4$ Thin Films for Solar Cell Applications

A Thesis

submitted by

Kaushlendra Pandey

(Regd. No. 901612015)

For the award of the degree

of

Doctor of Philosophy

THAPAR INSTITUTE
OF ENGINEERING & TECHNOLOGY
(Deemed to be University)

School of Physics and Materials Science
Thapar Institute of Engineering & Technology, Patiala 147004, India
March, 2022

DEDICATED

TO

MY LOVING GRANDPARENTS AND PARENTS

THESIS CERTIFICATE

I hereby certify that work presented in this thesis entitled “**Growth and Characterization of $Cu_2ZnSn(SSe)_4$ Thin Films for Solar Cell Applications**” in partial fulfilment of the requirement of the award of degree of DOCTOR OF PHILOSOPHY in the School of Physics and Materials Science, Thapar Institute of Engineering and Technology, Patiala is an authentic record of my own work carried out under supervision of Dr. Bhaskar Chandra Mohanty. The matter embodied in this thesis has not been submitted in part or full to any other university or institute for the award of any degree.

Kaushlendra Pandey

This is to certify that the above statement made by the candidate is true to the best of my knowledge.

Research Guide

(Dr. Bhaskar Chandra Mohanty)
Professor
School of Physics and Material Sciences
Thapar Institute of Engineering and Technology
Patiala

ACKNOWLEDGEMENTS

Prima facea, I am grateful to the God for the good health and wellbeing that were necessary to complete this thesis.

I would like to express my sincere gratitude to my advisor, Assoc. Prof. Bhaskar Chandra Mohanty for introducing me to the diverse and dynamic field of photovoltaics. Experimenting with this material calls for multidisciplinary approach, combining chemistry, physics and material science. I am grateful for his support and assistance during my thesis.

Furthermore, I would like to thank Dr. Puneet Sharma, Dr. Bhupendra N. Chudasama and Dr. Anil Arora for being part of my thesis committee, as well as for all the fruitful discussions.

I express my gratitude to Dr. Kulvir Singh, Professor and Head of School of physics and Materials Science.

I am very grateful to Dr. Bhupendra N. Chudasama from Nano medicine Lab, School of Physics and Material Sciences for allowing me to use their equipment for optical measurements and Dr. Poonam Uniyal and Dr. D. P. Singh for letting me use their equipment for electrical measurements.

I would also like to thank Dr. P. Malar from SRM institute of engineering and technology, Chennai and her team for her collaboration during this study. I am also thankful to Dr. Manoj Kumar Chauhan and Mr. Munish Kumar from JIIT, Noida.

I am especially grateful to my laboratory colleagues, Dr. Indu gupta, Dr. Neetu Bansal, Jyoti Jangra, Samarjit Mandal, Neha Saini and Ritika Sharma for their support and assistance to my work.

I thank my friends Dr. Santhosh Kumar Mahadevan, Dr. Gaurav Sharma, Raveena, Dr. Amandeep Kaur, Shivani Jain, Amanpreet, Kaveri, Manju, Pardeep Bhatia and all other friends for their great support throughout the tough times, for being so positive, supportive and helpful.

Lastly, I offer sincere thanks to my grandparents (Shri Krishna Nand Pandey and late Smt. Ram Urehi), parents (Shri Madhaw Ram Pandey and Smt. Neelam Pandey) and other family members and relatives for their love, motivation, encouragement, and unlimited patience throughout my education.

Kaushlendra Pandey

ABSTRACT

Cu_2ZnSnS_4 (CZTS) has emerged as a leading absorber candidate for thin film solar cells over the last few years due to its highly favorable optoelectronic properties. In addition, it has an earth abundant, non-toxic, and inexpensive constituent that promises development of cost-competitive solar cells. However, the formation of the single phase, which is crucial to the performance to the photovoltaic devices, has been found to be a big challenge in CZTS since a single phase exists within a much smaller chemical potential window. The tendency to form binary phases, selective re-evaporation of elements from the film, reaction at contacts, etc. further make it difficult to control the intended composition and the formation of single phase. Consequently, there is extensive ongoing efforts to design synthesis protocols for the fabrication of single phase CZTS with desired properties.

Various physical vapor deposition techniques, especially the sputter deposition one, which is being widely used in the optoelectronics industry, have performed poorly for the CZTS based devices. In this work, efforts have been made to fabricate CZTS thin films by RF magnetron sputtering of a single elementary target. The resulting films were post-selenized at different conditions to obtain $Cu_2ZnSn(SSe)_4$ (CZTSSe) thin films. The proposed route of film synthesis greatly simplifies the process steps in fabrication of these films. Based on the results, reaction mechanism of evolution of kesterite phase has been proposed.

The films grown from a target containing powders of Cu, Zn, Sn and S taken in stoichiometric proportion were always Cu -poor in spite of a large variation in the sputtering and post-deposition sulfurization parameters. This stoichiometric deviation of the precursor film was primarily due to the poor sputter yield of Cu. The Cu-deficiency led to the formation of spurious secondary phases. Cu deficiency in the precursor film was compensated by growing a Cu interlayer between successively sputtered Cu-Zn-Sn-S precursor layers. Inserting Cu-interlayer improved compositional stability through thermally activated diffusion of Cu from this intermediate layer towards both the sides and resulted in the formation of kesterite CZTS even at a modest sulfurization temperature of 500 °C. The obtained phase-pure films have a bandgap of ~1.58 eV and shows excellent photoresponse behavior characterized by increase in current by three orders of magnitude at a bias of 3 V upon white light illumination, typically that required for a potential absorber layer in thin film solar cells.

In an alternate approach, the Cu deficiency was mitigated by preparing a target from elemental powders with 12.5% excess of Cu. By intuitively manipulating the post-sulfurization process carried out in a quasi-open environment using sulfur flakes, single phase CZTS films could be obtained. The influencing mechanism of post-sulfurization process was elucidated from systematic variation in the dwell time, temperature and the sulfur amount. A high temperature or a shorter dwell time yielded a small-grained microstructure associated with the presence of secondary phases. By using the target with excess copper target, phase pure CZTS films with better microstructural features were obtained for sulfurization at 500 °C for 60 min with 1.0 g of sulfur flakes. This film exhibited an optical bandgap of ~1.58 eV indicating its photovoltaic potential. A device in the Mo/CZTS/Ag configuration showed typical features of a Schottky junction. The obtained current-voltage characteristic was analyzed to estimate saturation current, ideality factor and series resistance in correlation with the properties of the CZTS film.

Based on the results of efforts on preparing phase pure CZTS films by inserting a Cu interlayer for films grown from a target of stoichiometric composition or by carefully manipulating the sulfurization process for films prepared from a target containing excess Cu, a single step synthesis route was designed that did not require any post-deposition heat treatment. An elevated substrate temperature of 450 °C during sputter deposition using a single elementary target with excess Cu provided enough energy for the reaction and formation of kesterite phase. These films have an optical bandgap of ~1.6 eV and white light sensitivity >200% at a bias potential of 5 V, highly suitable for photovoltaic and photocatalytic activities. Detailed electro-impedance analyses have been carried out to confirm the p-type conductivity, carrier concentration and a carrier life time.

Finally, the CZTS thin films which were synthesized in a single process step were selenized and the influencing mechanisms of selenization parameters have been established. The process parameters such as selenization temperature, dwell time and selenium amount were found to significantly affect the composition, bandgap, microstructure and the reaction pathway leading to the formation of single phase CZTSSe thin films.

CONTENTS

Title **Page**

CHAPTER 1 INTRODUCTION

CHAPTER 2 EXPERIMENTAL DETAILS

CHPTER 3 FILMS GROWN FROM A TARGET OF STOICHIOMETRIC COMPOSITION

CHAPTER 4 GROWTH OF FILMS FROM A TARGET WITH EXCESS Cu

CHAPTER 5 SINGLE STEP PROCESSING OF CZTS THIN FILMS FROM A TARGET WITH EXCESS Cu

CHAPTER 6 SELENIZATION OF THE CZTS FILMS GROWN BY SINGLE STEP PROCESSING FROM A TARGET WITH EXCESS Cu

LIST OF FIGURES

Figures **Title** **Page**

LIST OF PUBLICATIONS

1. Kaushlendra Pandey, BC Mohanty, A thin Cu interlayer-mediated control of phase evolution of Cu2ZnSnS4 thin films grown by RF magnetron sputtering of a single elementary target with high white light sensitivity; ***Applied surface science*** **539 (2021) 148149**.
2. Kaushlendra Pandey, BC Mohanty, Influencing mechanism of post-sulfurization with sulfur flakes on phase evolution and Schottky diode characteristic of Cu2ZnSnS4 thin films sputter deposited from a single target; ***Solar Energy*** **228 (2021) 333-338**.
3. Kaushlendra Pandey, BC Mohanty, Facile single step synthesis of Cu_2ZnSnS_4 thin films by sputtering from a single target and their electrical characterization; ***J. Alloys. Com.*** **925 (2022), 166657**
4. Kaushlendra Pandey, Jyoti, BC Mohanty, Growth of large grained single phase thin films via controlled selenization of single step RF magnetron sputter deposited Cu2ZnSnS4 layers for photovoltaic applications. (Under preparation).
5. N Bansal, Kaushlendra Pandey, K Singh, BC Mohanty; Growth control of molybdenum thin films with simultaneously improved adhesion and conductivity via sputtering for thin film solar cell application; *Vacuum* 161 (2019) 347-352. *
6. Indu Gupta; Kaushlendra Pandey; Alok K Jain; P. Malar, BC Mohanty; Critical influence of annealing configuration in kesterite phase evolution during growth of Cu2ZnSnS4 thin films from non-toxic environment-friendly solutions; *J. Materials Electronics* (2021) 1-9. *

***.** Is not included in thesis.

LIST OF CONFERENCE PRESENTATIONS

1. Kaushlendra Pandey, BC Mohanty, Substrate Temperature Assisted Growth of Phase Pure Cu_2ZnSnS_4 Thin Films by RF Magnetron Sputtering using a Single Elementary Target for Solar Cell Applications; Poster presented at ***International virtual conference on Frontiers in Manufacturing Technology (FMT 2020)***, 13th-14th Oct. 2020, KIIT, Bhubaneswar, Odisha, India.
2. Kaushlendra Pandey, Kunal Tiwari, P. Malar and Bhaskar Chandra Mohanty, Characterization of Cu2ZnSnS4 thin films grown by RF magnetron sputtering from a single elementary target, Poster presented at ***International Conference on Nanoscience & Nanotechnology – 2019***, 28th – 30th Jan. 2019, Chennai.
3. Kaushlendra Pandey, BC Mohanty, Mo Back Contact for Cu2ZnSnS4 Thin Film Solar Cells; Poster presented at ***International Symposium on Functional Materials (ISFM)-2018***, Chandigarh.

CHAPTER 1
INTRODUCTION

1.1 Energy background

Increasing industrialization concurrent to the modernization of lifestyles of a fast-rising world population has increased the energy demand by many folds and put pressure on the safety and affordability of energy supply. The erosion of energy security and the growing energy needs coupled with the environmental risk stemming from fossil fuel combustion for energy solutions have posed serious challenges for the future. As per the data of the United Nations Intergovernmental Panel on Climate Change (IPCC) which concludes that the only scenarios resulting in a 50 to 85% reduction of global CO_2 emissions by 2050 compared to 2000 levels can limit the long term global mean caused temperature rise to 2.0 to 2.4 °C (un.org). In recent years, photovoltaic has emerged as a key technology that promises to mitigate this energy crisis significantly. However, this can be realized only if the cost of photovoltaic energy can be made competitive, which suggests that we must look out for cost-effective, nontoxic materials and fabrication processes to prepare highly efficient solar cells. In this context, thin film photovoltaic devices have drawn significant interest owing to reduced material utilization and simple cell design. Among these, $Cu(In,Ga)Se_2$ (CIGSSe) and CdTe solar cells have shown very promising record efficiencies of 23.4% and 22.1%, respectively (nrel.gov, Green et al., 2021).

However, this can be realized only if the cost of photovoltaic energy can be made competitive, which suggests that we must look out for cost-effective, nontoxic materials and fabrication processes to prepare highly efficient solar cells. In this context, thin film photovoltaic devices have drawn significant interest owing to reduced material utilization and simple cell design. Among these, $Cu(In,Ga)Se_2$ (CIGSSe) and CdTe solar cells have shown very promising record efficiencies of 23.4% and 22.1%, respectively (Green et al. 2021).

1.2 Cu_2ZnSnS_4 (CZTS) based thin films for solar cell

Despite of the promising thin film technologies of CIGSSe and CdTe, their suitability for large scale production is limited by the rarely abundant elements such as indium and tellurium. Besides, cadmium is a toxic element, which finds limited acceptance. More recently, indium (III) superseded by zinc and tin (II & IV respectively) in CIGSSe, copper zinc tin chalcogenide $Cu_2ZnSn(SSe)_4$ (CZTSSe) has emerged as a promising absorber material. Along with earth abundance, benign, and cost-efficient constituents, CZTSSe have a high absorption coefficient of the order of 10^4 cm^{-1} and a well-tailored direct bandgap (from 1 eV to 1.5 eV) that can resemble with the solar spectrum (Katagiri et al., 2009; Mitzi et al., 2011). Consequently, the CZTSSe turns out to be more economic and sustainable. Over the past few years, the energy conversion efficiency of CZTSSe has shown progress from ~ 6.8 in 2008 to beyond 12% just in a few years (Katagiri et al., 2008; Todorov et al., 2010; Guo et al., 2010; Barkhouse et al., 2012; Li et al., 2012; Scragg et al., 2013; Todorov et al., 2013; Wang et al., 2014). While the performance gap between the more mature CIGS technology and the CZTSSe continues to shrink, the latter one requires more customized approaches based on its anomalies. The metal chalcogenides, for example CIGSSe, exhibits forbearance of structural and electronic defects, and often the defects to the advantage of the device performance. Therefore, it allows some relaxation from the strict requirement of carefully controlled deposition processes to grow these thin films. However, it is not true for the CZTSSe layers. In most cases, the success of the devices has been related to the control of the formation of the phase pure CZTSSe. This itself is a big challenge, especially compared to CIGSSe because of the fact that stoichiometry range for the formation of single phase is very narrow, typically Cu-poor (Cu/(Zn+Sn) = 0.8-0.9) and Zn-rich (Zn/Sn = 1.1-1.4) (Olekseyuk et al., 2004; Wang et al., 2014). The evolution of single phase is quite challenging attributed to the formation of binary phases and re-evaporation of elements from the film that further make it difficult to control the intended composition and the formation of a single phase.

The processing of these films assumes even more importance when we consider the observed large open circuit voltage deficit compared to the more matured CIGSSe and CdTe thin film devices (Liu et al., 2016; Wallace et al. 2017; Polizzotti et al., 2013). This has been suggested to be due to abundant point defects and defect clusters (cationic disordering) and associated band tailing (Mitzi et al., 2013, Gunawan et al., 2014, Chen et al., 2013, Chen et al., 2010a, Chen et al., 2010b, Samji et al., 2016, Samji et al., 2014, Choudhari et al., 2020). The presence of such defects (and the defect pairs) induces the formation of energy levels in the electronic bandgap and for a higher degree of lattice disorder, the tail states at the top of the valence band and the bottom of the conduction band stretch into the bands causing narrowing of the bandgap (Gokmen et al., 2013; Miller et al., 2012; Islam et al., 2015). On the other hand, in the polycrystalline CZTS, the grain boundaries should be of specific type (i.e., a higher surface potential at grain boundaries than that at grains) (Samji et al., 2021, Choudhari et al., 2020) to minimize the recombination at the grain boundaries. Thus, processing of these films require delicate optimization of parameters. Around the globe, researchers are working on designing deposition processes that are simple and cost-competent, yet yield films of intended properties. This thesis aims to develop an inexpensive and simple deposition process through RF magnetron sputtering and understand the dependence of composition, grain size, optical and electrical properties on the process parameter of the resultant thin films.

1.2.1 Crystal structure and phase diagram of CZTSSe

CZTSSe is a quaternary material system that belongs to the I_2-II-IV-VI_4 family of compounds. It has crystal structure analogous to the ternary chalcopyrite $CuInSe_2$ (space group I42d) in which the In is replaced by Zn and Sn (Bernardini et al., 2000; Mitzi et al., 2011). Primarily, CZTSSe exist in two major crystal structures, namely kesterite (space group I4) and stannite (space group I42m). These crystal structures are quite similar, other than the stacking arrangement of the Cu and Zn atoms along the c-axis. However, in both structures, cations have located at tetrahedral sites. The crystal structure and atomic arrangement of the chalcopyrite as well as kesterite and stannite are presented in **Fig.** 1.1a-c. The kesterite structure is more stable than that of stannite due to lower negative formation energy, as reported in the literature (Schorr et al., 2011).

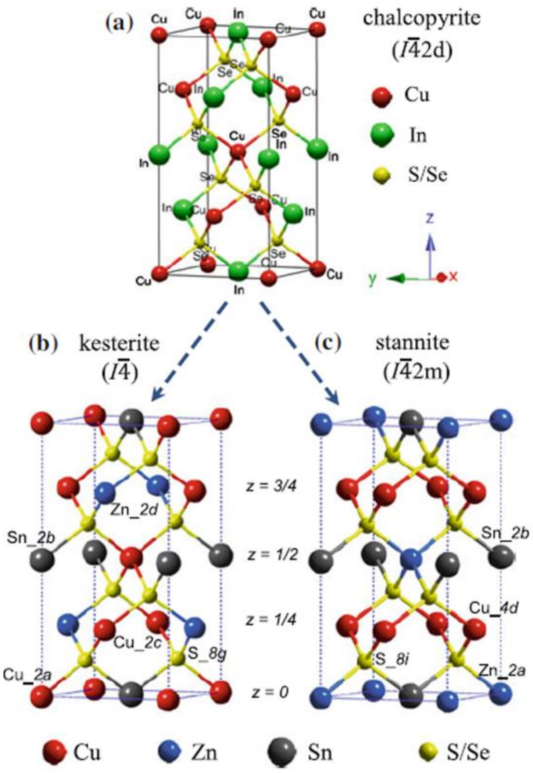

Fig. 1.1: Crystal structure of (a) $CuInSe_2$, (b) kesterite Cu_2ZnSnS_4 and (c) stannite Cu_2ZnSnS_4 [Das et al., 2016].

Irrespective of deposition techniques, the thin films of CZTS are populated by many intrinsic point defects, interstitial defects and antisite defects. In this system, Cu_{Zn} antisite defect is more commonly observed where Cu and Zn atom exchange sub-lattice to provide prompt rise of p- type conductivity to CZTSSe. Therefore, Cu poor and Zn rich stoichiometric composition is required to avoid the existence of the unwanted phases and subsequently, enhance the desired electrical properties as reported (Mitzi et al., 2011).

The evolution of the spurious phases while the formation of the CZTS thin films can be inferred from the ternary phase diagram as shown in Fig. 1.2. It has a very complicated phase space as reported by Olekseyuk et al, which suggests that it is very arduous to control the growth of the secondary phases and defects, owing to its very narrow composition window, marked by (*) in the phase diagram (Olekseyuk et al., 2004). The single phase CZTS can be only formed when the composition lies close to the stoichiometric proportion (Cu:Zn:Sn:S = 2:1:1:4). The small deviation in the composition accelerates the formation of the secondary phases that have detrimental effects on device performance.

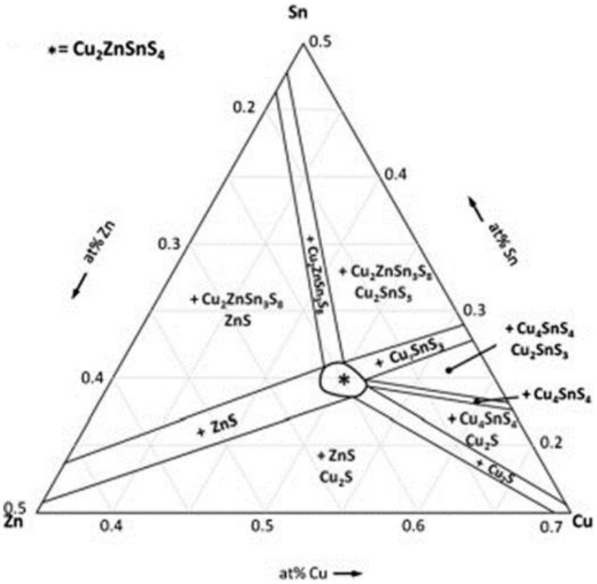

Fig. 1.2: Pseudo ternary phase diagram that shows very narrow region for the formation of CZTS (Olekseyuk et al., 2004).

1.2.2 Progress in efficiency of CZTSSe thin film solar cells

The earliest research reported on the compound CZTS came out in 1978 and dealt with the structure of the natural minerals kesterite and stagnant (Hall et al., 1978). Therein, using the X-ray diffraction (XRD), Hall et al. showed them to be structurally identical but distinct minerals (Hall et al., 1978). In 1988, Ito and Nakazawa (Ito et al., 1988) first reported the photovoltaic response of CZTS. They fabricated a CZTS/$CdSnO_3$ junction on stainless steel sheets, wherein the CZTS layer was grown by argon beam sputtering. They obtained bandgap of 1.45 eV for CZTS thin films (Ito et al., 1988). In 1997, Katagiri et al. fabricated the first device with structure ZnO:Al/CdS/CZTS/Mo/SLG (soda lime glass) and found the open circuit voltage (V_{OC}) to be ~400 mV with an efficiency of 0.66 % (Katagiri et al., 1997). A 2.3 % efficient CZTS solar cell was reported by Friedlmeier in 1997 having similar device structure to the one designed by Katagiri et al. The only difference in Friedlmeier et al. report was that they synthesized CZTS by the sulfidation of co-deposited Cu-Zn-Sn films (Friedlmeier et al., 1997). Furthermore, Katagiri et al. improved the efficiency to 5.45% in 2003 by using an improved sulfidation chamber (Katagiri et al., 2003). In 2008, they found 6.77% by soaking the CZTS films in the DI water that preferentially etched metal oxides in the CZTS film (Katagiri et al., 2008). Mitzi et al. in 2010 reported 9.6% efficiency for solution based CZTSSe solar cells (Todorov et al., 2010). Further the efficiency of device was improved to 12.6%, which is the highest so far (Wang et. al., 2014).

1.2.3 Deposition of the CZTS based thin films

A variety of processing techniques, such as thermal evaporation (Repins et al., 2012), solution-based processes (Barkhhouse et al., 2012; Todorov et al., 2013; Wang et al., 2014), electro-deposition (Ennaoui et al., 2009), sputtering (Scragg et al., 2013; Kim et al., 2014; Lin et al., 2016; Yan et al., 2016; Sun et al., 2018), etc. have been employed to prepare the CZTSSe thin films. The success of a particular deposition technique depends on facile synthesis of single phase films and higher scope for large scale implementation. So far, a solution based process containing hydrazine exhibited the maximum conversion efficiency of 12.6% (Wang et al., 2014). However, the major disadvantage of this process is the use of large amounts of explosive, hepatotoxic (Choudhary et al., 1998)' and carcinogenic hydrazine (Roe et al., 1967).

On the other hand, performance of the physical deposition techniques which have yielded the highest efficiency for CIGS-based devices (nrel.gov), has been poorer (Repins et al., 2012). In particular, sputtering technique, which has been recognized as an industry-friendly route for thin film fabrication for optoelectronic applications has not been successful in the case of CZTS based devices and forms the basis of this thesis. Sputter deposition has been recognized as a clean process (being a vacuum based technique, it leaves little residue unlike solution based methods) to synthesize thin films of various alloys and compounds (Wasa et al., 2005, Lundin et al., 2019). Although the deposition process is complex, it allows to track growth and microstructure of the films. In the optoelectronic industry, wherein large area deposition and up-scalability are required, sputter deposition process has fared well. In literature, this method has been used extensively to deposit not only CZTS but also many other absorber layers in photovoltaic devices. The following sections describe the important developments in fabrication of CZTSSe thin films by sputter based approaches and the motivations behind this work.

1.2.3.1 Sputter deposition of CZTSSe thin films

Sputtering is a physical vapor deposition technique for growing thin films, involving ejection of material from the target (source) onto a substrate. Different types of sputtering methods viz. direct current (DC), radio frequency (RF), reactive as well as hybrid magnetic sputtering used for the deposition of the CZTSSe thin films. Previously reported photovoltaic performance of CZTS/CZTSSe thin films deposited by sputtering has been summarized in a tabular form in Appendix 1.

In 1988, Ito and Nakazawa (Ito et al., 1988) presented first report of deposition of CZTS thin films by argon beam sputtering with a band gap of 1.45eV and stannite structure. Later on, Tanaka et al. fabricated the CZTS films by a technology of hybrid sputtering; they heat treated precursor layers deposited sequentially Cu/Zn/Sn (bottom) in sulfur flux at various temperatures (Tanaka et al., 2005). CZTS phase starts evolving at ~350 °C with a direct bandgap around ~1.5 eV and absorption coefficient better than 10^4 cm^{-1}. For annealing at higher temperatures above 450 °C, there was significant loss of Zn due to its high vapor pressure, and the problem was resolved by replacing Zn in the initial stack by ZnS (Tanaka et al., 2005).

In 2007, Katagiri's group prepared CZTS by sulfurizing precursor layers (580 °C for 3 hrs in H_2S atmosphere) deposited by co-sputtering from Cu, SnS, and ZnS targets (Jimbo et al., 2007). They attained a PEC of 5.74%. Katagiri et al. have also studied the role of the Cu:Zn:Sn ratio on the output of the devices. They suggested that CZTS solar cells with highest efficiency is obtained arround Zn/Sn ≈ 1.25 and Cu/(Zn+Sn) ≈ 0.9 (Katagiri et al., 2009). Additionally, the varying concentration of H_2S from 5% to 20% had minor effect on device properties (Katagiri et al., 2008). Li et al. reactive co-sputtered Cu, Zn, and Sn targets to deposit CZTS films in a 50% H_2S/Ar mixture at 5 mtorr. Film annealing was done at 550 °C and 40 mtorr in the presence of 10% H_2S/Ar mixture. The devices showed V_{OC} of 0.428 V, J_{SC} of 12.40 mA/cm^2 and an efficiency of 3.37%. The authors have co-sputtered $CuSe_2$, ZnS, and

SnS_2 compound targets for depositing CZTS and annealing was done at 580 °C in a SnS and S_2 atmosphere. The incorporation of selenium (i.e., CZTSSe based films) yielded significantly higher efficiency (7.75 %). The authors showed that the CZTSSe films have higher surface potential near the grain boundaries than in the CZTS films (Li et al., 2012). Scragg et al (Scragg et al., 2014) have deposited the CZTS films by reactive DC magnetron co-sputtering (pulsed) followed by annealing of the Cu-Zn-Sn-S precursor layer comprising of Cu: Sn (2:1) alloy and pure Zn targets in H_2S atmosphere. They reported an efficiency of 4.6 %.

Yan et al. in 2018 have reported preparation of CZTS films via co-sputtering of Cu/ZnS/SnS precursor film followed by rapid thermal annealing at 560 °C with SnS and S for 20 min. The film showed the highest efficiency of 11.01% (Yan et al., 2018). In 2019, Temgoua et al. reported 7.1% efficient CZTSSe thin film based solar cells (Temgoua et al., 2019). They fabricated the CZTSSe films by selenizing the precursor films at 600 °C for 1 hr with different Se and S+Se concentrations. The precursor films were grown by co-sputtering of Cu/ZnS/SnS metallic layer. Ma et al., in 2020, have reported 8.2% efficiency from the films prepared by co-sputtering of Cu/ZnS/SnS and subsequently annealed in S atmosphere at 610 °C for 10 min (Ma et al., 2020).

While preparing the CZTSSe thin films from sequential sputtering of multiple targets, a number of researchers have reported the effects of stack sequence, thickness of each layer, and the temperature and duration of selenization/sulfurization on the properties of the eventual films and the photovoltaic characteristics. For instance, Fernandes et al. have studied the effect of stack order on the final quality of CZTS thin films. They found the Zn/Sn/Cu (top) better than Sn/Zn/Cu (top) stack (Fernandes et al., 2009). Fukano et al. concluded that three stack layer (ZnS/Sn/Cu (top)) was better than four stack layer (ZnS/Sn/Cu/ ZnS (top)) while preparing CZTS thin films (Fukano et al., 2013). They reported an efficiency of 7.6% for their devices. In 2009, Zoppi et al. reported CZTSe thin film based solar cells with an efficiency of 3.2% . They prepared the CZTSe films by selenizing (in a mixed Ar and Se atmosphere at 500 °C for 30 min) the sequentially magnetron sputtered of Cu, Zn and Sn layers. They claimed that Cu-poor and Zn-rich absorber layers are required for highly efficient solar cells (Zoppi et al., 2009). Chalapathy et al. showed that the sulphur annealed Cu/ZnSn/Cu precursor stack layer which was sensitive to the annealing temperature (Chalapathy et al., 2011). Kim et al. have used Cu, ZnS and SnS targets to grow CZTSSe thin films in the stacking order of Cu/SnS/ZnS/Mo/glass and the selenization was done for 20 mins at 590 °C to obtain an efficiency of 8.06% (Kim et al., 2014). Li, et al. have grown CZTSSe by DC/RF sputtering from Sn/Cu/ZnS/Sn/ZnS/Cu stack layers and the films were annealed at 300 °C for 20 min in Ar atmosphere followed by selenization at 570 °C for 15 min. By changing the Zn/Sn ratio, an efficiency of 10.2% was achieved (Li et al., 2016).

Son et al. in 2019 have CZTSSe films by sequential deposition of Cu/SnS/ZnS by DC (Cu) and RF (SnS and ZnS) magnetron sputtering. The selenization of as-deposited films were done by rapid thermal annealing with SeS_2 and Se at 250-590 °C. They suggested that temperature played critical role in phase formation as well as on the grain growth of the films. This group reported a champion cell, with 9.47% efficiency (Son et al., 2019). In 2020, Lu et al. have reported 8.4% efficiency using a films grown RF magnetron sputtering from Cu/Zn/Cu/Sn stack metallic layer. After that, the film was annealed at 350-590 °C for different time in S containing environment (Lu et al., 2020). They have suggested that the thickness of Cu layer can control the Cu/(Zn+Sn) ratio. In 2021, Lu et al. fabricated CZTS films by sequential sputtering of Zn/Cu/Sn/Cu. Further, the precursor film was sulfurized at tree step process to enlarge the grain size, primarily at 310 °C for 15 followed by 570 °C for 15 min and then quickly raised temperature upto 600 °C (in 10 sec) for min. In addition to this, CdS layer deposited on CZTS was annealed at 250 to 325 °C for 10 min. They suggested that Cd diffused to the CZTS layer and replaced the Cu atoms, which helped to reduce the interface recombination and band alignment. They have reported 9.75% efficient solar cell through this strategy (Lu et al., 2021). Jeong et al. have prepared CZTSSe thin films by 2-step annealing at 300 °C for 1 hr followed by 520 °C for 7.5 min in S and Se ambience. They prepared the precursor layer in the form of Cu-Zn-Sn stacks by DC magnetron sputtering. The power conversion efficiency was found to 9.82% by altering S/(S+Se) ratio (Jeong et al.,2021).

1.2.3.2 Efforts on single target sputter deposition

Compared to the co-sputtering and sequential sputtering using multiple targets, sputter deposition using a single target can greatly reduce the experimental complexity and appears very lucrative for large scale production. It may possibly yield uniform and smooth films similar to the cases of CIGS (Shi et al., 2011; Frantz et al., 2011). A brief review of the efforts on single target sputtered CZTSSe films has been provided in the followings.

In 2003, Kim et al. have prepared a precursor layer by RF magnetron sputtering from a target containing finely mixed Cu_2S, ZnS and SnS_2 (Seol et al., 2003) and annealed it in Ar + S_2 gas. They reported that it was difficult to maintain the target stoichiometry in the films. In 2013, they have prepared CZTS films by sulfurization of the precursor layer deposited by RF magnetron from a single Cu-Zn-Sn target (Amal et al., 2013). They concluded that sulfurization at 500-550 °C is required for synthesis of a single phase. In 2012, Sun et al. have compared the film properties of the CZTS films by RF sputtering and pulsed laser deposition (PLD) from a sintered CZTS target. The target was prepared by hot pressing at 700^0C for 2 hrs under Ar atmosphere using the powder obtained by solid-state reaction of Cu_2S, ZnS and SnS_2 powders. They reported that the films from sputtering were very poor in Cu (Cu/(Zn+Sn) =0.394) while that from the PLD was Cu-rich (Cu/(Zn+Sn) =1.34). In 2014, Xie et al. fabricated CZTS films, using middle frequency magnetron sputtering by ceramic quaternary target followed by a post sulfurization process at 460 to 580 °C (Xie et al., 2014). They reported the loss of Zn during the sputtering, which made the films poor in Zn, although Zn rich targets were employed. They also reported coexistence of minor SnS phase with CZTS. The films sulfurized at 580 °C had an optical bandgap of ~1.55 eV. Nakamura et al. prepared the precursor of the CZTS thin films by RF magnetron sputtering (Nakamura et al., 2014). The precursor layer was annealed in H_2S (5%) and N_2 atmosphere. The CZTS target was prepared by adjusting the Cu-poor and Zn-rich composition. Lastly the film was annealed at 500°C in order to achieve an efficiency of 4.40%.

In 2015, Dalapati et al. reported solar cell efficiency of 3.07% for CZTS thin films prepared by single target RF sputtering sulfurized with sulfur powder at 500-700 °C for 10 min (Dalpati et al., 2015). Recently, in 2016, Feng et al. reported significant improvement in structural, optical and electrical properties with increases in sulfurization temperature from 400–500 °C in single target RF magnetron sputter deposited thin films (Feng et al., 2016). They reported presence of SnS_2 phase and voids along with the Zn and Sn loss at sulfurization temperature of 550 °C while a solar cell efficiency of 4.4% of CZTS film was obtained when sulfurized at 500 °C. Lin et al. in 2016, reported the preparation of CZTS target by mixing CuS, ZnS and SnS_2 at different weight ratios. They prepared CZTS thin films and fabricated solar cell of highest efficiency of 5.2% (Lin et al., 2016). Lin, et al. in 2017, have deposited CZTS films by a compound target. The film was sulfo-selenized at 570 °C for 1 hr with varying S/(S+Se) ratios. The efficiency obtained from the resultant film was ~ 6.9% (Lin, et al., 2017). Hangtao, et al. have prepared CZTS films by RF magnetron sputtering of a single target. Their efficiency was, however, lower at 3.74% (Cui et al., 2017). Dalapati, et al. in 2017 deposited CZTS by RF-magnetron sputtering by using stoichiometric Cu_2ZnSnS_4 target and achieved an overall efficiency of 4.4% (Dalpati et al., 2017).

Sun et al. in 2018 have grown CZTS films by RF magnetron sputtering using a quaternary target and selenized the resultant CZTS layers at various temperatures in the presence of H_2Se gas. Till now the most efficiency i.e 9.6% was reported by single target sputtered film, selenized at 560 °C (Sun et al., 2018). In 2020, Ren et al. obtained an efficiency of 9.13% for CZTSSe thin film based solar cells. They deposited the CZTS films by co-sputtering by RF magnetron using two quaternary targets with different Cu concentration. The prepared film was selenized in H_2Se ambiance by two step process, primarily, at 400 °C then 520 °C for 20-20 min (Ren et al., 2020). Cheng et al., in 2021 fabricated CZTS thin films via two step selenization a CZTS film grown by RF magnetron sputtering with quaternary target and found a 7.9% efficient CZTSSe solar cells (Cheng et al., 2021). Simya et al. in 2022 have grown CZTS thin films by RF-sputtering using a CZTS quaternary target. After the deposition, the precursor film was in-situ annealed and reported an efficiency of 2.6% (Simya et al., 2022).

One of the major reason of limited success of the single target sputtering relies on the peculiar properties of CZTS itself. Owing to a narrow region of phase stability and low formation energy of constituent binary sulphides, it has been very difficult to obtain phase pure films even from the carefully prepared sputter targets (Mamedov et al., 2017; Nagoya et al., 2010; Katagiri et al., 2001; Persson, 2010). Furthermore, different sputter yield for Cu, Zn, Sn and S makes it very difficult in controlling the congruent transfer of elements from the target to the films in vapor phase.

The formation of CZTS is believed to proceed from the reaction of the binary sulphides as given in Eq. (1.1) facilitated by post-deposition annealing carried out in the sulfur ambience.

$$Cu_2S\ (s) + ZnS\ (s) + SnS_2\ (s) \rightarrow Cu_2ZnSnS_4\ (s) \qquad (1.1)$$

As shown by many groups, (Friedlmeier et al., 1997; Tanaka et al., 2005; Scragg et al., 2014; Seol et al., 2003; Amal and Kim, 2013; Sun et al., 2012; Xie et al., 2014) the composition of the as-deposited film and the annealing determine the reaction pathway and the eventual phase(s) of the film. For instance, for films grown by co-evaporation, a mixture of phases ZnS and Cu_2SnS_3 has been reported, which has been attributed to the poor Cu/(Zn+Sn) ratio (Aydin and Akyuz, 2020). Similarly, in the case of sputter-deposition of films from a quaternary target of CZTS, secondary phases of SnS/SnS_2 were always obtained even after sulfurization at 550 °C when the Cu/(Zn+Sn) ratio was in the range of 0.35-0.38 (Sun et al., 2012; Yoo et al., 2013). This (i.e., presence of secondary phases) is also supported by other studies, for example by Inamdar et al., 2011 and 2012., wherein the deficit of the Cu and Zn content led to the formation of binary sulphide phase like CuS or Sn_2S_3 along with CZTS for deposition from a quaternary CZTS target (Inamdar et al., 2011 and 2012). Based on the phase diagram and the formation energy of the associated compounds, the likelihood of formation of the binary sulphides corresponds to the deviation in the ideal Cu/(Zn+Sn) ratio (Mamedov et al., 2017; Nagoya et al., 2010; Katagiri et al., 2001).

On the other hand, all routes of film synthesis involve the deposition of as prepared film and annealed at temperatures > 500 °C in a sulfur-containing gaseous environment. While in the simple elemental thin films, a post-deposition annealing yields primarily microstructural alterations, the effects thereof in the case of compound thin films are more complex (Dalapati et al., 2015; Wang et al., 2017; Moholkar et al., 2011). For instance, in CZTS, these annealing yields phase transformation in the form of reaction between binary intermediates resulting in eventual kesterite CZTS with a microstructure significantly different from that of the precursor film (Wang et al., 2017; Amal & Kim, 2013; Chen et al., 2013 and 2014). More importantly, owing to the narrow window of single phase and low formation energy of secondary phases, many spurious phases evolve during this post-deposition annealing (Katagiri et al., 2001; Olekseyuk et al., 2004; Nagoya et al., 2010; Persson et al., 2010). Hence, the choice of sulfurization (i.e., post-deposition annealing in sulfur environment) configuration becomes very critical in obtaining single phase kesterite CZTS (Wang et al., 2017; Thota et al., 2017, Gupta et al., 2021).

The effect of the sulfurization parameters during the fabrication of CZTS thin films is reported to be very diverse and significant. For instance, Sun et al. have found that sulfurization of sputter-deposited precursor films at high temperatures around 500 °C in absence of additional chalcogenide leads to evolution of secondary phases like Cu-S, SnS, ZnS, etc (Sun et al., 2018). These secondary phases led to a highly porous microstructure. Contrastingly, sulfurization at 560 °C with sufficient sulfur yielded multiple secondary phases like Cu_xS and ZnS along with CZTS with the resultant film having a cracked microstructure (Sun et al., 2018; Amal & Kim, 2013; Redinger et al., 2011). Thota et al. have reported a microstructure characterized by small sized non-uniform grains for sulfurization at 500 °C in the presence of sulfur for 1 hr, whereas a shorter sulfurization duration (up to 30 min) yielded bi-metallic (Cu_5Zn_8/CuSn) and metal sulfide ($Cu_{2-x}S$/SnS_2) spurious phases (Thota et al., 2017). Similarly, Yoo et al. have reported a non-uniform texture and loosely packed surface with pinholes along with secondary phases like SnS_2, for sulfurization at 440 -550 °C in presence of sulfur source (Yoo et al., 2012; Chalapathi et al., 2015). This observed wide variation in the microstructure of the films and the phases indicates a gap in the understanding of mechanism of evolution of microstructure in preparing single phase CZTS. While the different phases in the Cu-Zn-Sn-S system evolve, an associated evolution of microstructure is expected during the reaction at intermediate stages, which critically influences the eventual microstructure of the films.

The discussion presented above reveals that the annealing parameters are very critical in that they control the reaction path path eventually resulted in formation of CZTS thin films via intermediate reaction between binary and ternary compounds (Olekseyuk et al., 2004; Scragg et al., 2014; Seol et al., 2003; Amal and Kim, 2013). Thus, the annealing process should be delicately controlled for obtaining films with CZTS film with required properties. Therefore, a simple annealing strategy is highly preferred to avoid complex configurations. It is highly recommended to ascertain the influencing mechanisms of the same and rationalize the growth patterns for reliable reproduction of the CZTS films.

Selenium inclusion in the CZTS system is very crucial in that it appreciably improves the grain size and the quality of absorber layer (Wei et al. 2019)**.** It decreases the series resistance as well as open circuit voltage (V_{OC}) deficit that help to enhance the efficiency of the solar cells (Wei. et al., 2019; Minbashi et al., 2020). The inclusion of selenium has remarkable impact on the optical and electronic properties of the CZTSSe films such as bandgap tuning from 1.5 (CZTS) to 1.0 (CZTSe) eV and improvement in V_{OC} as well as short circuit current (J_{SC}) because of reduction in defect density which otherwise act as recombination centers (Minbashi et al., 2020). Therefore, an organized study of selenium incorporation, which can influence the device performance, is of high interest.

1.3 Motivation and objectives

The literature review presented in the preceding sections suggests that the potential of the sputter deposition process has not been fully exploited because of the inherent material peculiarities of CZTS. Although, research is ongoing with the single target sputtering that is a simple and promising technique for large-scale adaptability to prepare the CZTSSe thin films, the highest efficiency reported so far from single target sputtering is only 9.6% (Sun et al., 2018). While post deposition annealing plays a critical role in evolution of the kesterite phase of the films, the annealing process parameters, viz., the temperature, dwell time and sulfur/selenium vapor pressure must be controlled delicately, as evidenced from the reports of evolution of spurious phases and potential loss of volatile compounds. This work proposes the systematic growth of the CZTSSe thin films using a single elementary target by RF magnetron sputtering followed by post deposition annealing. Furthermore, differently with the reported studies that use the toxic H_2S gas, the films in this work were annealed with solid sulfur flakes (Emrani et al., 2013), which make the overall synthesis route more environmental friendly. The results of this investigation can provide comprehensive approach to the understand the growth of phase pure CZTSSe thin films.

The main objectives of this thesis are

- To grow CZTS thin films by RF magnetron sputtering.
- To study the effects of selenization of the prepared CZTS thin films on various properties.
- To elucidate the effects of process parameters on structure, optical and electrical properties of the thin films.

1.4 Outline of the thesis

This thesis is organized in seven chapters. Chapters 1 contains the introduction of the material and literature review. It highlights the key challenges in the fabrication of CZTS films and its impact on solar cells. This chapter provides the advantages of sputtering approach along with the detailed survey from the literature, which supports and provides the path to achieve the objectives.

Chapter 2 describes the experimental details of fabrication of the thin films. It also includes details of the analytical techniques (for example XRD, Raman spectroscopy, SEM, EDS, current-voltage characteristics, impedance spectroscopy, etc.) used to characterize the obtained films.

Chapter 3 highlights the role of composition on the growth of CZTS phase. A very simple and cost-competitive approach to fabricate kesterite CZTS thin films by depositing films using an in-house built sputter target and through compositional manipulation via a thin Cu interlayer has been demonstrated. The films were grown from a target with stoichiometric composition. Consequently, high fractions of spurious phases were always obtained although a large variation in the sulfurization configuration was adopted. This was overcome by inserting a thick Cu interlayer that contributed to enhanced compositional stability through thermally activated diffusion of Cu from the intermediate layer towards both sides and the following reaction even at a modest sulfurization temperature of 500 °C. The obtained phase-pure films were found to have a bandgap of 1.58 eV and very high white light sensitivity, typically that is required for a potential absorber layer in thin film solar cells.

Chapter 4 demonstrates the role of growth of CZTS films by using a single target by intuitively manipulating the target composition and the influencing mechanisms of post-sulfurization process. The results of post deposition heat treatment were elucidated from systematic variation in the dwell time, temperature and the sulfur amount. Based on the obtained results a rational strategy for the growth of phase pure CZTS thin films grown by RF magnetron sputtering of a single elementary target has been proposed. Schottky barrier characteristics of the phase pure films have been studied at room temperature in the Mo/CZTS/Ag configuration that showed typical features of Schottky contact. The current voltage characteristics of the device was analyzed to estimate saturation current, ideality factor and series resistance.

Chapter 5 illustrates the role of substrate heating on the growth of CZTS phase. The post-deposition treatment was completely eliminated by using a high substrate temperature during deposition of films. The thermal energy required for the reaction and formation of kesterite phase was provided via intuitive manipulation of the substrate temperature. A nominally high substrate temperature of 450 °C facilitated reaction in the depositing species that yielded single phase CZTS as confirmed by XRD and Raman analyses. The films had an optical bandgap of ~1.6 eV, highly suitable for photovoltaic and photocatalytic activities. The resultant films exhibited high white light sensitivity (>200% at a bias potential of 5 V). Electrochemical analysis of the device with structure of Mo/CZTS/Electrolyte/Pt was carried out to find type of conductivity and carrier concentration.

Chapter 6 deals with the systematic study of selenium inclusion in the CZTS thin films. The consequences of the variation in the amount of selenium, dwell time and selenization temperature was investigated in detail. It is demonstrated that the Se/(S+Se) ratio that can be well tuned by manipulating the selenization conditions controlled not only the bandgap but also the evolution single phase kesterite thin films.

Chapter 7 summarizes the work carried out and discusses scope for future work.

CHAPTER 2

EXPERIMENTAL DETAILS

This chapter describes the experimental details of fabrication of the thin films and the numerous techniques, for example, X-ray diffraction (XRD), Raman spectroscopy, Scanning Electron Microscopy (SEM), Energy Dispersive X-ray Spectroscopy (EDS), X-ray photoelectron spectroscopy (XPS), current-voltage characteristics, impedance spectroscopy, etc. used to characterize the obtained films.

2.1 Preparation of sputter target for CZTS and CZTSSe thin films

Among the variety of thin film growth methods, deposition by sputtering has been recognized as an industrially attractive route for large area deposition and up-scalability (Wasa et al., 2005, Lundin et al., 2019). As mentioned in Chapter 1, this thesis deals with CZTS thin films grown by RF magnetron sputtering. The sputter target was prepared using elemental powders of Cu (99.9 %, Alfa Aesar), Zn (99.5 %, Spectrochem), Sn (99.9 %, Loba Chemie) and S (99.5 %, Alfa Aesar) taken in the stoichiometric 2:1:1:4 proportion. The powders were mixed by ball milling for 3 hours at 300 rpm in ethanol medium. Subsequently, the powder was dried in a hot air oven for 24 hours at 80 °C. A 2-inch target was prepared by uniaxial pressing of this powder using an indigenously designed 2” die. This as-pressed target was sintered at 300 °C for 60 min. The sintered target was used to deposit the films by RF magnetron sputtering. Figure 2.1a shows the photograph of such a target. However, it was found that the only two rounds of depositions could be completed, as the target unevenly cracked, although the RF power density was as low as 3.7 W/cm^2. The photograph of the cracked target is shown in Fig. 2.1b. The cracking of the sputter target is attributed to the poor thermal stress distribution during the deposition (Delrue et at., 2005; Winnicki et al., 2017). The longevity of the targets, however, could be greatly improved when the sintered target was glued (by indium) to a copper back plate as shown in Fig. 2.1c. In some cases, target with excess Cu amount was prepared. The excess Cu was added to compensate Cu loss during deposition, arises due to discrepancy in the sputter yields of associated element. In certain cases, the as-pressed targets (i.e., the one not sintered) have been used.

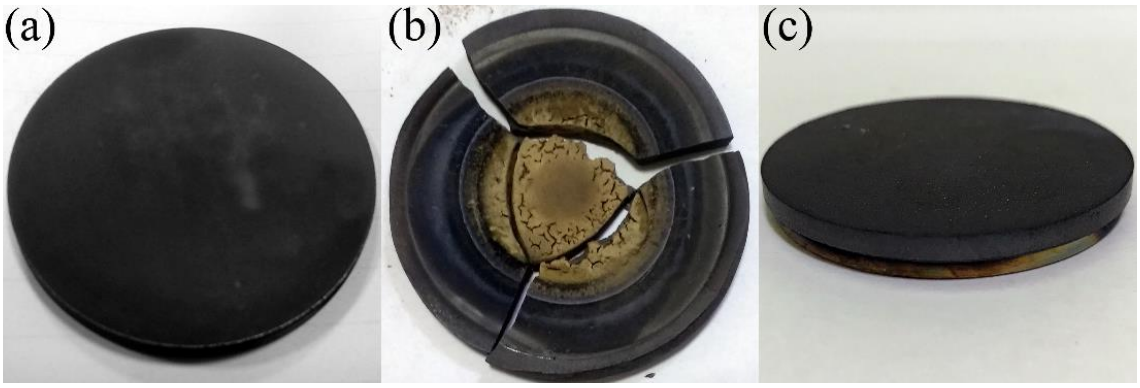

Fig. 2.1: Photograph of (a) a target before use, (b) a cracked target after only two depositions and (c) a sintered target glued with Cu back plate via indium bonding. The Cu back plate provided better heat dissipation that improved the longevity of the target.

2.2 Deposition of thin films

In this work, the absorber CZTS layer was grown by RF magnetron sputtering. The CZTSSe thin films were prepared by post-selenization of the CZTS thin films. The back contact Mo layer was synthesized by DC magnetron sputtering. Thermal evaporation was used to fabricate the top electrode through a shadow mask. The details of films preparation are given in the following sections.

2.2.1 Growth of CZTS and CZTSSe thin films

The films were grown using the prepared target mentioned in section 2.1. During deposition, the sputter parameters like power, working pressure and substrate temperature were varied and the effects thereof were studied. Cleaned soda lime glass pieces (1 inch × 1 inch) held at room temperature were used as substrates. In the present sputter system, the substrates made an angle about 30° with respect to the normal to the target. The distance between the centers of target and substrate was ~5 cm. The substrate holder was rotated at 16 rotations per min about its axis. The chamber was evacuated to base pressure better than 4.0×10^{-6} mbar. The Ar pressure was maintained at 1.0×10^{-2} mbar by a mass flow controller make at 36 standard cubic centimeter per minute (SCCM). The actual photograph of the sputter system is presented in Fig. 2.2.

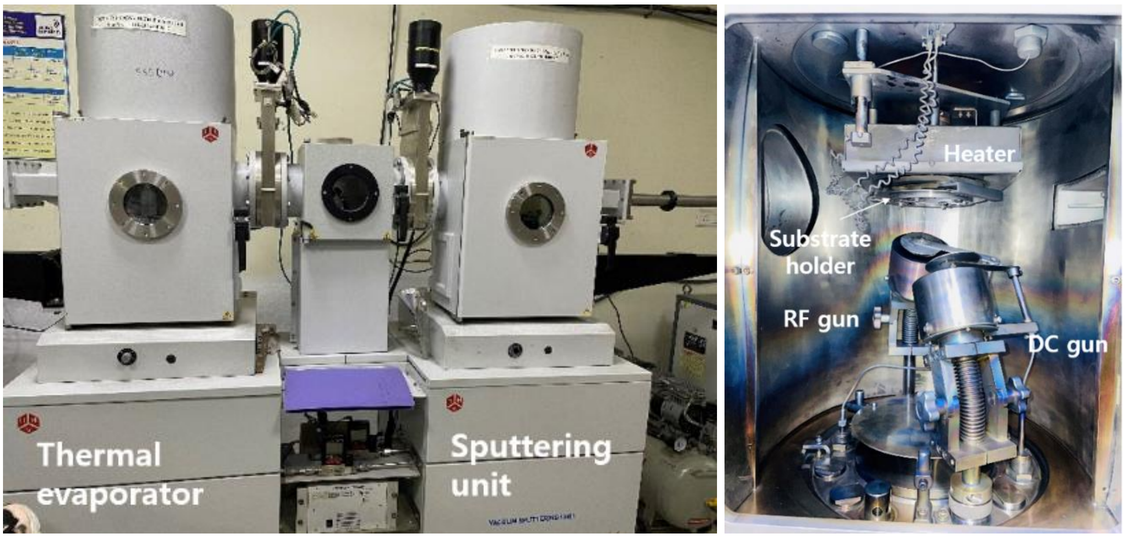

Fig. 2.2: Actual photograph of external and internal view of the magnetron sputtering machine used in this thesis work.

Post-deposition heat treatment was carried out using a tubular furnace. The as-deposited films were sulfurized at temperature ranging from 300-575 °C with different amounts of sulfur taken in a silica crucible. High pure (>99%) argon was used as a carrier gas. During sulfurization, the as-deposited films were kept directly over sulfur flakes. After a specified duration of sulfurization, the heater was switched off and the furnace was allowed to cool naturally. The photograph of deposition and sulfurization setup is summarized in Fig. 2.3.

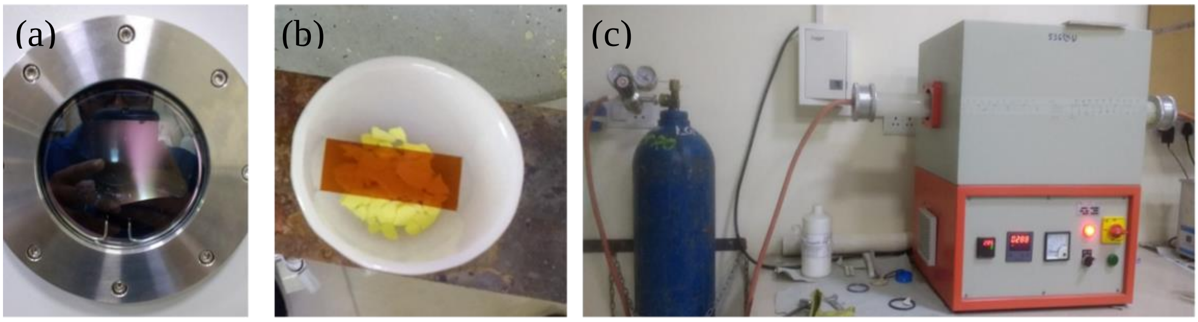

Fig. 2.3: Photograph of (a) deposition chamber during the sputtering process, (b) arrangement of sulfur and the precursor film in a silica crucible for sulfurization, and (c) the furnace and the sulfurization setup.

2.2.2 Deposition of Mo thin films

Molybdenum (Mo) is the most commonly used material as back contact in CIGS and CZTS based thin film solar cells. However, the adhesion of the Mo films to soda lime glass substrate has been an issue. Adhesion of the films can be improved by using a higher Ar pressure during sputter deposition. However, higher Ar pressure induces micro-cracks that results in increased electrical resistivity of the samples (Bansal et al., 2019). We have alleviated this problem by using a bi-layer (Scofield et al., 1995) where the bottom layer was deposited at high pressure (2.6×10^{-2} mbar) to provide better adhesion with the glass substrate followed by a top layer at low pressure (2.6×10^{-3} mbar) for uniformly textured surface. The details of the deposition are given in Ref. (Bansal et al., 2019; 2020). Briefly, the bi-layer structured films were grown by DC magnetron sputtering using Mo target (Tredmann Pvt. Ltd, Taiwan; 99.99%) on soda lime glass substrate (2cm×2cm). The deposition power was maintained at 150 W for 10 min (high pressure) and 20 min (low pressure). In this sputter system, the target was inclined at ~30° with respect normal to the substrate and the target to substrate distance was ~10 cm. Substrate was rotated ~16 rpm about its axis. All depositions were carried out at room temperature.

2.2.3 Deposition of contacts (Al and Ag)

Aluminum (Al) and Silver (Ag) are widely used as a top contact/grid in the CZTS and CIGS thin film solar cells. These materials were also used as contact to study the photosensitivity as well as to form Schottky junction in the Mo/CZTS/Ag or Al structure. The contacts were grown by thermal evaporator using Al ingots and Ag wire as a precursor material. The vacuum chamber was evacuated $> 4 \times 10^{-6}$ mbar. Stainless steel mask was used for the masking the defined area. A quartz crystal thickness monitor was used to measure thickness of the films in-situ.

2.3 Characterization techniques

Various analytical techniques were used to characterize the structural, optical and electrical properties of the prepared films. Brief details of each are given in the followings.

2.3.1 XRD measurements

XRD is a non-destructive technique that is used to determine structure of crystalline solids. It relies on diffraction of the incident X-rays by the materials. Several useful information including that of structure, lattice parameters, crystallite size, strain etc. can be inferred from analysis of the XRD patterns. In the present work, a PanAnalitical X-ray diffractometer with Cu-k_α radiation was used. The crystallite size of the film was estimated by the Debye Scherrer formula (Chandel et al., 2018):

$$d_{hkl} = \frac{0.9\,\lambda}{\beta cos\theta} \quad (2.1)$$

Where d_{hkl}, λ, β and θ is signify the interplanar spacing, wavelength of X-ray, full width at half maxima and angle of diffraction of peaks, respectively.

2.3.2 Raman Spectroscopy

Raman spectroscopy can provide details about chemical structure, phase and crystallinity **(**Fernandes et al., 2011**).** It is based on the interaction of light with a material's chemical bonds. A laser source is used as an excitation source for the Raman scattering in which the incoming light are absorbed and then reemitted with the swing in the frequency known as Raman shift. The Raman shifts comprehends the rotational and vibrational frequency information of the molecules of samples. The frequency changes are occurred from phase to phase, and can be easily detected by the Raman spectroscopy. The shift in energy is the characteristic of the vibrating chemical bonds in a material, and can be used to identify the materials. In the present work, the Renishaw Raman microscope associated with 514 nm excitation wavelength of laser has been used.

2.3.3 SEM and EDS measurements

The surface and cross-sectional morphology of the films have been studied by SEM. This tool is capable of producing high-resolution images of a sample surface. When a high energy electron beam fall on the sample surface, it generates numerous type of signals such as secondary electron, backscattered electrons, characteristic X-rays and transmitted electrons. An inelastic interaction between sample electron and incident photon produce secondary electrons. The SEM system is equipped with the standard secondary electron detector. The energy characteristic X-ray can be measured by EDS and is used to quantify the elements in the sample. This can also measure the distribution of the elements over the surface. For this measurement, we have used a field emission scanning electron microscopy (FESEM) (Hitachi SU8000) for the surface and cross-sectional image of the films. Some of the samples have also been characterized by a Zeiss Sigma 500 system. Thickness of the films was estimated from the obtained cross-sectional image. The EDS measurements was made using Brukers XFLASH 60 system.

2.3.4 XPS measurements

The XPS measurements have been carried out to estimate the surface information and its chemical environment. It is used to differential the chemical bonding that makes this technique unique. The operational principle of this technique is to irradiation of the atoms from the film surface through photon, which ejects the electrons. The kinetic energy of the electrons is correlated to the binding energy as given by eq.

$$KE = hv - BE - \emptyset_s \qquad (2.2)$$

Where hv signify the photon energy and $\emptyset_s$ shows the work function. For our work, we have used a Thermo-Fisher XPS Kα system with Al K_α source.

2.3.5 UV-Vis Spectroscopy

Absorbance (A), transmittance (T) and reflectance (R) of the sample were directly estimated by UV-Vis spectroscopy. The absorption coefficient (α) was calculated by following formula (Fouad et al., 2018; Ghobadi et al., 2013)

$$\alpha = \frac{1}{t}\ln\left[\frac{(1-R)^2}{T}\right] \text{ or } \alpha = 2.303\frac{A}{t} \qquad (2.3)$$

Where A, T, R and t represent the absorption, transmittance, reflectance and thickness of the sample, respectively. The optical band gap of the sample was estimated from the Tauc plot of $(\alpha h\upsilon)^2$ vs hυ plot using the following expression

$$\alpha h\upsilon = A(\alpha h\upsilon - E_g)^m \qquad (2.4)$$

Where A, hυ and m indicate the constant, photon energy and the nature of optical transition. For CZTS, m is equals to ½ because of direct allowed transition. A, T and R were measured using a Shimadzu (UV3600) spectrophotometer equipped with a 150 mm integrating sphere.

2.3.6 Electrical Properties

2.3.6.1 Four probe resistivity measurements

A four probe or van der Pauw method is commonly used to measure the resistivity of the thin film samples. An electrical resistivity of any arbitrary shape and size can be measured accurately by this method (Pauw et al., 1958). In this technique, four-point probes (Ohmic contact) are placed at edge of the sample, as shown in Fig. 2.5. Current is applied in two probes and the potential difference in the other two probes is measured. This process was repeated by changing the polarity simultaneously with vertical and horizontal arrangements.

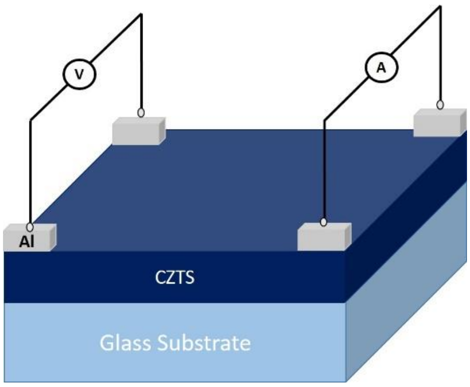

Fig. 2.4: Schematic of electrical resistivity measurements by van der Pauw method.

The resistivity of the thin film sample was calculated using the formula given below (Pauw et al., 1958)

$$\rho = \frac{\pi}{\ln{(2)}} \times R \times t \qquad (2.5)$$

where R is the resistance and t if the thickness of the sample. In this study, we have used a Keithley 2450 source measure unit.

2.3.6.2 Photosensitivity measurement

Photosensitivity of the device was carried out to study the photo response of the absorber layer. A pre-calibrated halogen lamp (equivalent to sun's light) was used to measure the light sensitivity by varying the bias voltage and measured the current, which provides the I-V curve. The dark I-V measurements were also taken to compare the response of the absorber upon illumination. The I-V characteristics were performed by using Keithley 2400 and 2450 source meters. The light source was standardized to 100 mW/cm^{-2} by an optical power meter (Newport).

2.3.6.3 p-n Junction and Schottky junction properties

Dark I-V characteristic of the prepared Mo/CZTS/Ag structure was performed to estimate the electrical parameters of Schottky diode such as ideality factor, saturation current and series resistance. The I-V characteristics were performed by using Keithley 2400 and 2450 source meters.

2.3.7 Electrochemical impedance spectroscopy (EIS) and Mott-Schottky (MS) analysis

EIS is a technique to record the impedance of the system over a range of frequencies. The data obtained by the EIS measurement is often presented in the form of Nyquist (real vs imaginary impedance) or Bode plot (frequency vs magnitude of impedance and phase angle). Impedance is the opposition to the alternating current (AC) flow in a complex system. The opposition to AC or DC is simply resistance if the system is fully resistive. The faradaic impedance of an electrolyte/electrode interface in an electrochemical cell is the combination of electrical resistance and capacitance at that interface. Electrochemical double-layer capacitance describes how an electrode/electrolyte interface behaves like a capacitance. The charge transfer resistance and the double-layer capacitance are included in the equivalent circuit for the redox reaction. Nyquist plot with a potentiostat as well as an impedance analyzer, allows determining the charge transfer resistance, ohmic resistance and double-layer capacitance. Nyquist diagrams are made of several arcs for complex reactions than redox reactions and with mass-transfer limitations.

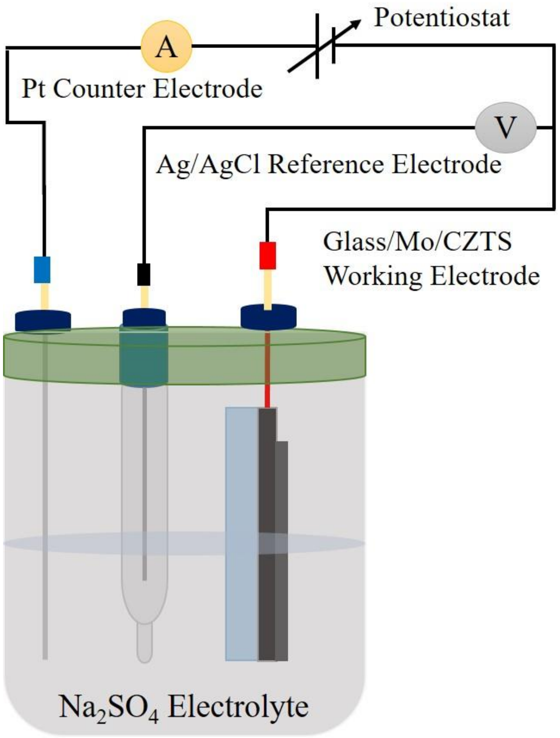

Fig. 2.5: Schematic diagram of electrochemical impedance spectroscopy and Mott-Schottky measurements.

A MS plot describes the reciprocal of the square of capacitance $1/C^2$ versus the potential difference (V) between bulk semiconductor and bulk electrolyte in semiconductor electrochemistry and photovoltaic technology. It was observed that the MS plot is linear in several experimental measurements for the semiconductor/electrolyte junction under applied bias voltage at a fixed frequency. The system properties such as type of semiconductor (p or n), flat band potential and carrier concentration can be estimated from MS analysis. For our measurements, we have recorded the data by using an electrochemical workstation (Biologic VSP 300). A standard three electrode configuration was used where Pt wire and Ag/AgCl in saturated KCl (0.197 V vs normal hydrogen electrode, NHE) were used as counter and reference electrode, respectively.

CHAPTER 3

FILMS GROWN FROM A TARGET OF STOICHIOMETRIC COMPOSITION

Deposition of single phase kesterite CZTS thin films by a cost-competitive method has been found to be very challenging due to a narrow region of phase stability and low formation energy of the secondary phases, as discussed in Chapter 1. The deviation in the composition leads to the co-existence of the spurious phase such as Cu_2SnS_3, Cu_4SnS_4, SnS, Cu_2S, ZnS and etc., which have detrimental effects on the performance of the solar cells. Thus, the composition of the film should be controlled to avoid the evolution of secondary phases. While sputter growth of thin films, especially by the deposition from a single target, appears very attractive, the formation of secondary phases therein must be suppressed. This chapter deals with a very simple and cost-competitive approach to fabricate kesterite CZTS thin films using an in-house built sputter target and through compositional manipulation via a thin Cu interlayer.

As presented in the experimental section (Chapter 2), a 2-inch diameter single elementary target was prepared using elemental powder of Cu, Zn, Sn and S taken in stoichiometric 2:1:1:4 proportion. The as-pressed target was sintered at 300 °C. The sintered target was glued by indium to a copper base plate (Fig. 2.1c). The chamber was evacuated to base pressure better than 4.0×10^{-6} mbar. The Ar pressure was maintained at 1.0×10^{-2} mbar. The post-deposition heat treatment was carried out using a tubular furnace. The as-deposited films were sulfurized at 500 °C for 60 min in the Ar ambient at atmospheric pressure. Heating profile and a schematic diagram of the typical sulfurization configuration are shown in Fig. 3.1a and b. The as-deposited films were placed directly over sulfur flakes taken in a silica crucible during the sulfurization process. After 60 minutes of sulfurization, the heater was switched off and the furnace was allowed to cool naturally.

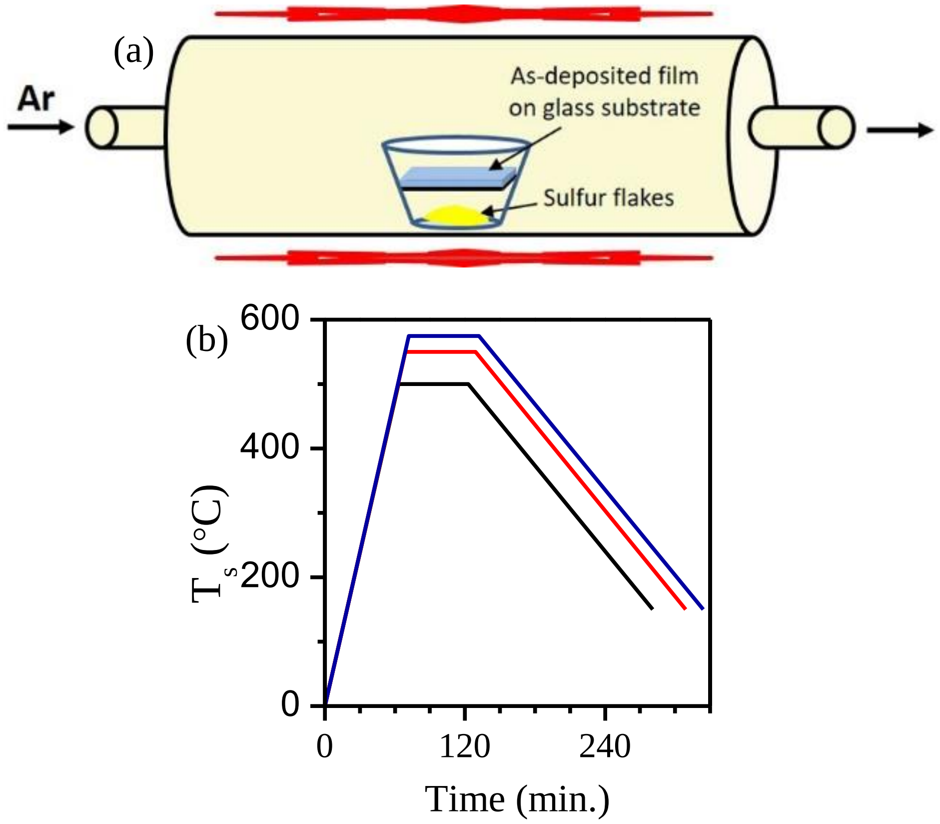

Fig. 3.1: (a) Schematic diagram of the sulfurization setup, where the sulfur and the as-deposited film were placed in a silica crucible and (b) heating profile for sulfurization with ramp rate 8°/min.

3.1 Structural characterization

3.1.1 Effect of sputtering power

Films were grown at different RF power namely at 50, 75 and 100 W. The deposition time (120 min for 50W, 75 min for 75W and 30 min for 100W) was varied to obtain films of similar thicknesses. All films were sulfurized at 500 °C (typical temperature required to the phase evolution of CZTS) for 60 min with 1.0 g of sulfur. Fig. 3.2a depicts typical XRD patterns of the films grown at different powers. While the observed peaks at 28.44 and 47.34° could be possibly attributed to the diffraction from (112) and (220) planes of kesterite CZTS (JCPDS file: 26-0575), the intense peaks at ~26.5 and 33.8° correspond to secondary phases. The minor peak at 51.7° in the case of 50 and 75 W samples are also attributed to the secondary phases. However, the film grown at high power (100 W), loses its crystallinity, caused by re-sputtering or re-evaporation of the target ingredients (Dalapati et al., 2015). Additionally, the formation of the secondary phases during sulfurization might be due to the compositional disparity from the stoichiometric proportion in the films, associated due loss of volatile elements at high temperature (Scragg et al., 2011). Hence, 75 W power was opted to carryforward the further optimizations. The thickness of the films was estimated from cross-section micrograph as shown in Fig 3.2b. The thickness of the film (deposited at 75W) was about 700 nm.

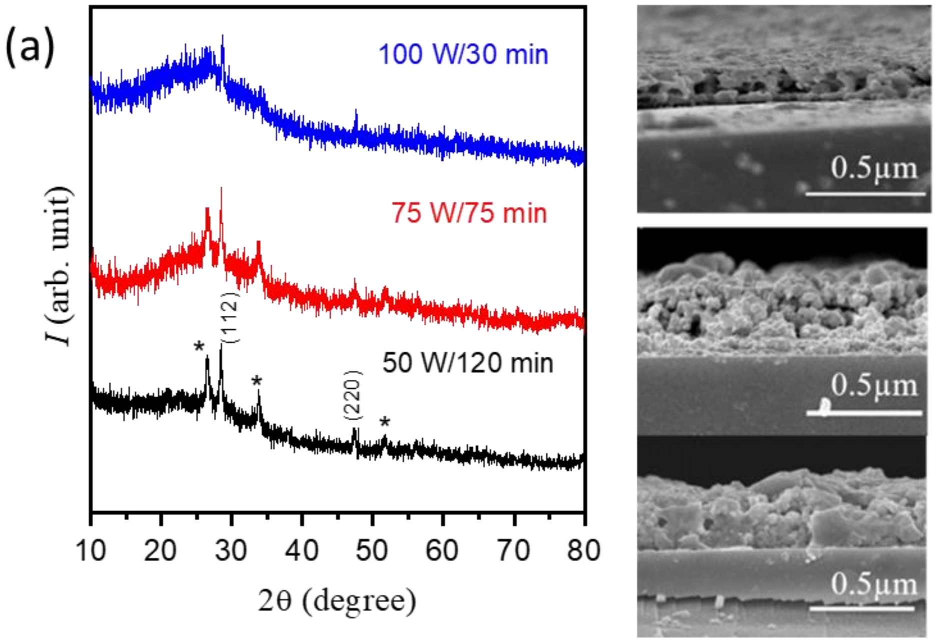

Fig. 3.2: (a) Typical XRD patterns and (b) cross-sectional micrographs of CZTS films grown at 50, 75 and 100 W for 120, 75 and 30 min. The asterisk (*) shows secondary phases (Please refer to text for details). All films were sulfurized at 500°C for 60 minutes with 1.0 g of sulfur.

3.1.2 Effect of sulfurization temperature and sulfur quantity

The as-deposited film grown with a RF power of 75 W was devoid of any crystalline phase as identified from the broad hump in the XRD pattern (Fig. 3.3a). The film had a uniform featureless surface, as revealed from the FESEM image (Fig. 3.3b). The thickness of the film was estimated to be about 700 nm from the cross-sectional FESEM image shown in Fig. 3.3c.

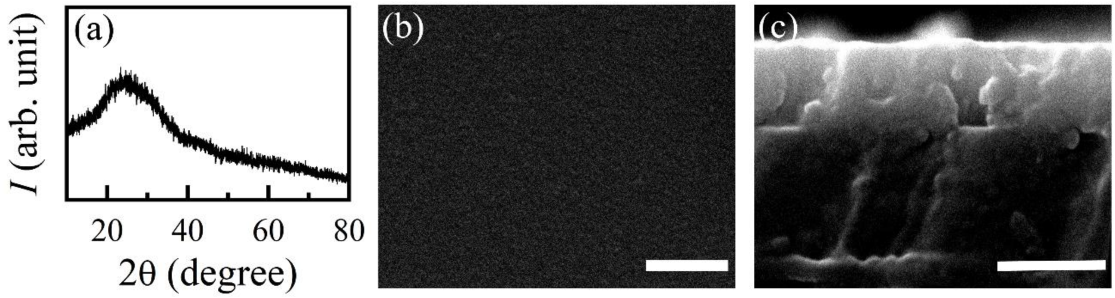

Fig. 3.3: (a) Typical XRD pattern, (b) surface microstructure and (c) cross-sectional FESEM image of the as-deposited film grown at 75 W. The scale bar in the micrographs corresponds to 1µm.

These as-deposited samples were sulfurized as per the heating profiles depicted in Fig. 3.1. Upon sulfurization at 500 °C, sharp peaks at ~26.5°, 28.5°, 34.0°, 38.0°, 47.5°, 51.8° and 56.3° suggesting well crystallized nature of the film appeared in the corresponding XRD pattern (Fig. 3.4a). The peaks at 28.5°, 38.0°, 47.5° and 56.3° are identified with (112), (211), (220) and (312) planes of CZTS (JCPDS file: 26-0575), respectively. It may be noted that due to overlapping of various Bragg peaks from CZTS with those of ZnS (JCPDS file: 3-65-5476) or cubic Cu_2SnS_3 (JCPDS file: 1-89-2877), it is very difficult to ascertain the peaks unambiguously. For example, the peaks at 28.5°, 47.5° and 56.3° can also be ascribed to (111), (220) and (311) peaks of ZnS or (111), (220) and (311) of cubic Cu_2SnS_3. The two peaks at 26.5° and 51.8° are identified with (021) and (221) planes of SnS (JCPDS file: 3-065-3875) (Li et al., 2017; El kissani et al., 2016; Emrani et al., 2013; Sun et al., 2018)or (100) and (103) planes of ZnS (wurtzite) (El kissani et al., 2016). The other peak at 34.0° is identified as (211) of SnS (JCPDS file: 3-065-2610). This clearly shows the presence of secondary phases in the sample. When the sulfurization temperature was increased, the nature of the XRD pattern did not change. Sharp peaks at 2θ values similar to those in the 500 °C-sulfurized sample were obtained. The results suggest that in spite of heat treatment at a temperature as high as 575 °C, it was not possible to obtain single phase CZTS. This is in contrast to many earlier reports wherein phase pure films were obtained at similar temperature range (He et al., 2013, Emrani et al., 2013; Sun et al., 2018; Jiang et al., 2018; Dalapati et al., 2015; Yang et al., 2015; Gupta et al., 2019). It may be noted that since sulfur would sublime at ~160 °C (denoted in Fig. 3.1b), the reaction of the sulfur with the precursor film during the initial phase of heating cycle followed by grain growth at later stage is expected (Olgar et al., 2019; Sun et al., 2018). More importantly, the presence of sulfur vapor during the high temperature annealing has been shown to have critical influence on the eventual phase of the films (Sun et al., 2018; Jiang et al., 2018; Wang et al., 2017). Considering the quasi-open environment of sulfurization in the present case, it is highly unlikely that sufficient sulfur pressure was maintained during the entire course of sulfurization. To verify that the observed results were indeed due to the insufficient amount of sulfur, additional experiments were carried out by significantly varying the sulfur amount in the crucible during the sulfurization process. The XRD patterns of the samples sulfurized via profile (i) in Fig. 3.1b are shown in Fig. 3.4b. The patterns are very much similar to the ones presented in Fig. 3.4a, suggesting the presence of the secondary phases.

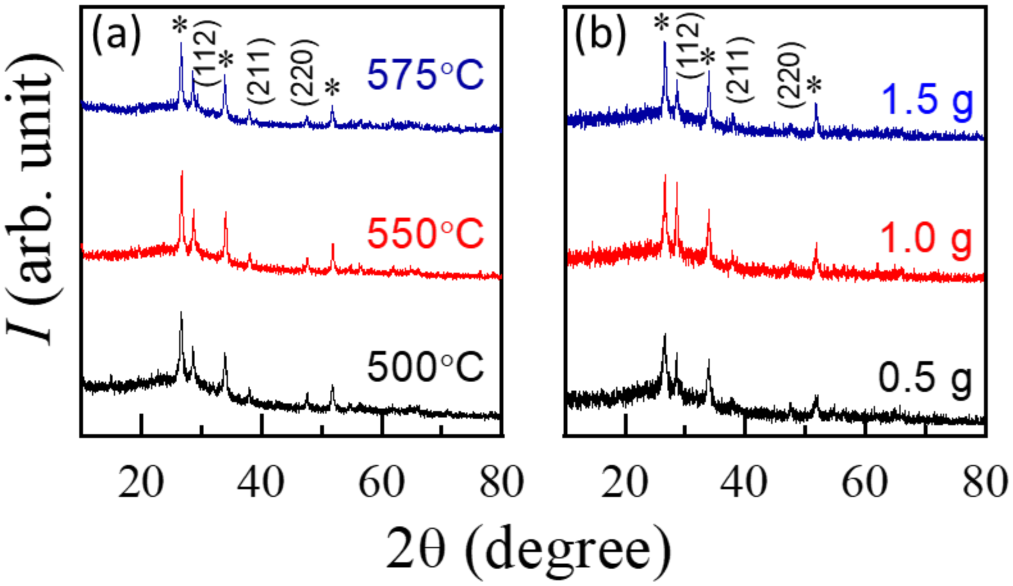

Fig. 3.4: Typical XRD patterns of the films sulfurized at (a) different sulfurization temperatures with 2.0 g sulfur (b) 500 °C with different amounts of sulfur in the sulfurization crucible. The asterisk (*) shows secondary phases (Please refer to text for details)..

3.1.3 Effect of sulfurization time

The precursor films were sulfurized at 500 °C (typical temperature required for phase evolution of kesterite CZTS) for different durations, namely 15, 30, 60 and 120 mins with 1.0 g sulfur. Figure 3.5 shows the typical XRD patterns of the films. As shown in this figure, irrespective of the reaction time, all of the films displayed similar diffraction patterns. In each pattern, diffraction peaks at 28.44°, 47.31° and 56.17° were observed corresponding to the CZTS (JCPDS 26-0575) compound. However, there were peaks at 26.5, 33.7 and 52.0°, which are attributed to the secondary phases as described in the previous section.

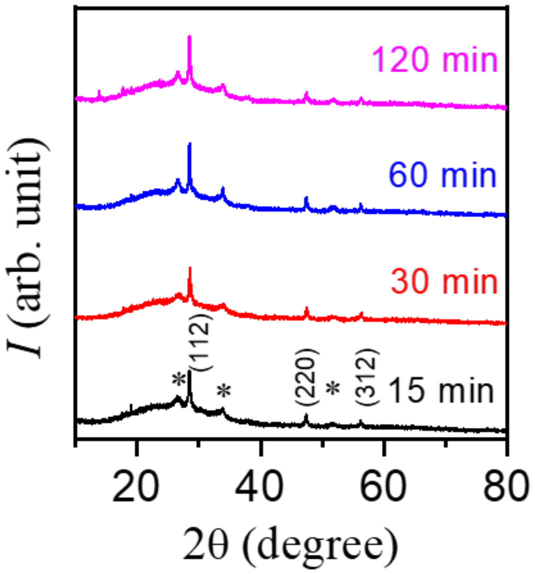

Fig. 3.5: Typical XRD patterns of CZTS films sulfurized at 500 °C for different durations with 1.0 g sulfur. The asterisk (*) shows secondary phases (Please refer to text for details)..

3.2 Compositional analysis

Based on the observed results, (i.e, despite a high temperature, time and a large variation in the sulfur amount, the XRD patterns remained the same and single-phase films were not obtained), the composition of the films is thought to a possible reason for the same (Scragg et al., 2011; Olgar et al., 2019; Thota et al., 2017; Ren et al., 2017; Sun et al., 2018; Sun et al., 2018; Dalapati et al., 2015; Redinger et al., 2011; Tanaka et al., 2010). The composition of the as-deposited and sulfurized films was estimated from the EDS analysis of the samples measured at multiple points (at least four) on sample surface and is shown in Fig. 3.6. As shown in the figure, all the films (as-deposited and sulfurized ones) were highly Cu-poor. The Cu/(Zn+Sn) and Zn/Sn ratio in the films decreased considerably than that in the target, which is in agreement with earlier reports of other research groups (Sun et al., 2012; Aydin et al., 2020; Yoo et al., 2013; Inamdar et al., 2011,2012 & 2013; Scragg et al., 2011; Olgar et al., 2019; Thota et al., 2017; Ren et al., 2017; Emrani et al., 2013; Sun et al., 2018; Jiang et al., 2018; Dalapati et al., 2015; Redinger e al., 2011). Some of these compositions are also highlighted in the figure. Considering the narrow phase stability region of CZTS (Nagoya et al., 2010; Katagiri et al., 2001; Olekseyuk et al., 2004), such a Cu-deficiency prevented the growth of phase pure films. The observed Cu-deficiency in the films is attributed to the poor Cu yield compared to that of Zn and Sn during the sputtering process [Sigmund et al., 1969]. The sputter yield is greatly dependent on the mass ratio of target atom to incoming ion, energy and angle of incident ion as well as the binding energy of target elements. Among Cu, Zn and Sn, Cu has the highest surface binding energy and the lowest atomic mass, leading to poor Cu amount in the films (Sigmund et al., 1969).

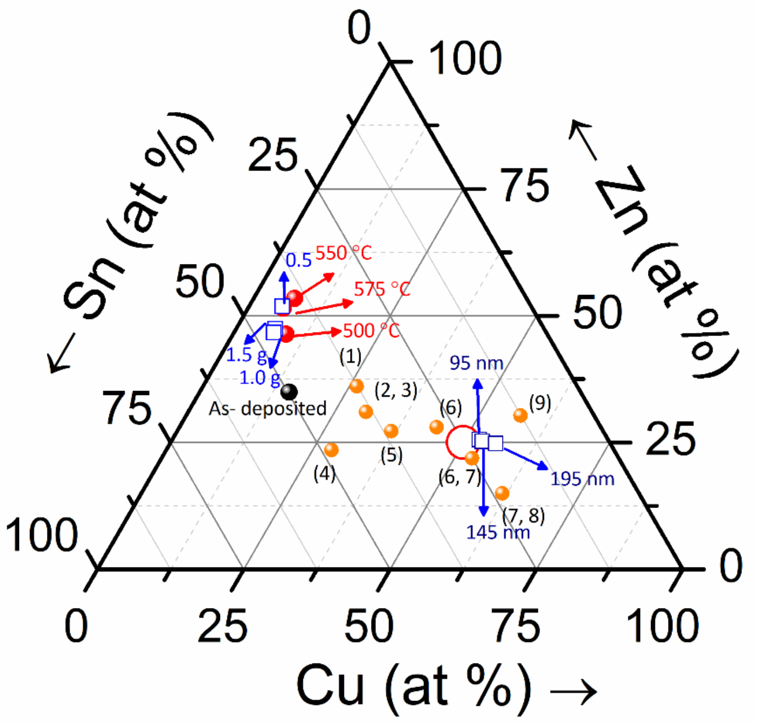

Fig. 3.6: Pseudo-ternary phase diagram showing composition of the films, as estimated by EDS. The black dot depicts the as-deposited sample, the red dots show the samples sulfurized at different temperatures with 2.0 g of sulfur, blue open squares show the sample sulfurized at 500 °C with different amounts of sulfur in the sulfurization crucible. The royal-blue open squares represent composition of the films grown with varying thickness of Cu interlayers. The stoichiometric composition is marked by open red circle. The orange color dots represent the compositions of samples reported by other groups (1: Dalapati et al., 2015; 2: Yang et al., 2015; 3: Inamdar et al., 2012; 4: Emrani et al., 2013; 5: Jiang et al., 2018; 6: Sun et al., 2011; 7: Inamdar et al., 2013; 8: Olgar et al., 2019; 9: Redinger et al., 2011).

3.3 Effect of a Cu-inter layer on the phase evolution

3.3.1 Structural characterization

The composition of the as-deposited film and hence the eventual sulfurized films was significantly changed via growth of a thin Cu interlayer sandwiched between two CZTS layers by DC magnetron sputtering (DC power of 75 W, Ar pressure of 1.0×10^{-2} mbar). The impact of the amount of additional Cu was studied in detail by varying the thickness of the Cu interlayer. Figure 3.7a depicts typical XRD patterns of samples containing a Cu interlayer of varying thickness. Compared to the sample grown without the Cu interlayer and sulfurized in identical condition, i.e., at 500 °C for 60 min with 1.0 g of sulfur (Fig. 3.4b), there are progressive changes in the patterns as the thickness of the Cu interlayer increased. A close look at the peaks also revealed that the crystallinity of the samples increased with increase in thickness of the interlayer. For the nominal thickness of ~95 nm of the interlayer, a Bragg peak at about 26.5° corresponding to (021) plane of SnS (JCPDS file: 3-065-3875) (Li et al., 2017; kissani et al., 2016; Emrani et al., 2013; Sun et al., 2018) or (100) plane of ZnS (wurtzite) (kissani et al., 2016) was observed. This suggests the persistence of the spurious phases in the films. However, intensity of this peak significantly decreased when the thickness of the Cu interlayer was increased to 145 nm. With further increase in Cu thickness to ~195 nm, this peak of the secondary phase disappeared completely, suggesting the growth of phase pure kesterite. Further confirmation of the phase purity of the sample was made from the analysis of the Raman spectrum of the sample, as shown in Fig. 3.7b. The figure shows two strong peaks centered around 285 and 333 cm^{-1}, which are attributed to the A1 symmetry from vibration of sulfur atoms corresponding to the kesterite CZTS (Fernandes et al., 2011).

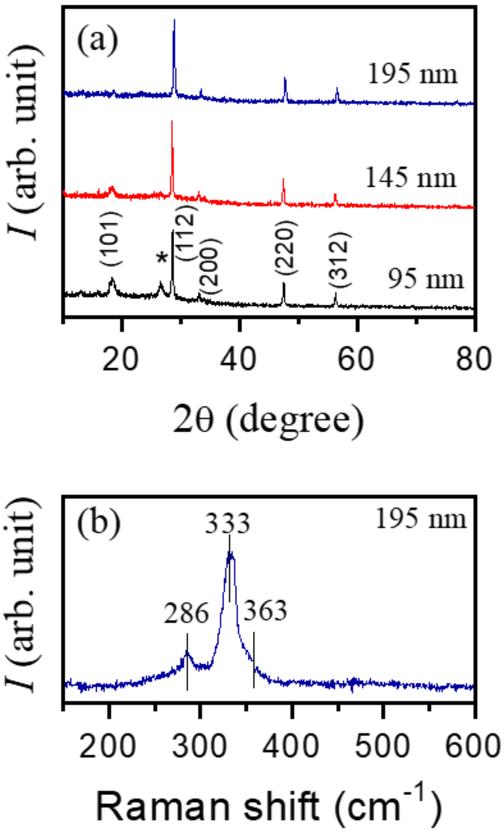

Fig. 3.7: (a) Typical XRD patterns of films grown with varying thicknesses of the Cu interlayers. The symbol (*) denotes impurities phase (Please refer to text for details).; (b) Raman spectrum of the film grown with ~195 nm thick Cu interlayer.

3.3.2 Microstructural characterization

For a direct observation of the impact of the Cu interlayer, cross-sectional micrographs of the sample (i.e., grown with 195 nm thick Cu interlayer) before and after sulfurization were obtained and are presented in Fig. 3.8a and 3.8b, respectively. The thickness of the as-deposited and sulfurized films was estimated through cross-sectional micrograph, which is found to be is ~700 nm and ~1.1 µm, respectively. While a clear sandwich structure is observed in the as-deposited sample, the demarcation for the intermediate Cu layer is completely lost upon sulfurization at 500 °C. Apparently, there is no segregation at the middle. This is indicative of the thermally activated diffusion of Cu from the intermediate layer towards both sides and reaction, which culminated in the growth of a homogeneous film. For this film, a highly uniform surface (Fig. 3.8c) characterized by densely-packed particulates of size of ~300 nm was observed. Similar observation of uniform distribution of elements has been reported earlier for the CZTS films grown by sulfurization of metallic stacks (Emrani et al., 2013). As disucussed in the followings, the observed microstructure and the phase purity of the film is believed to stem from the improved compositional stability provided by the additional Cu layer.

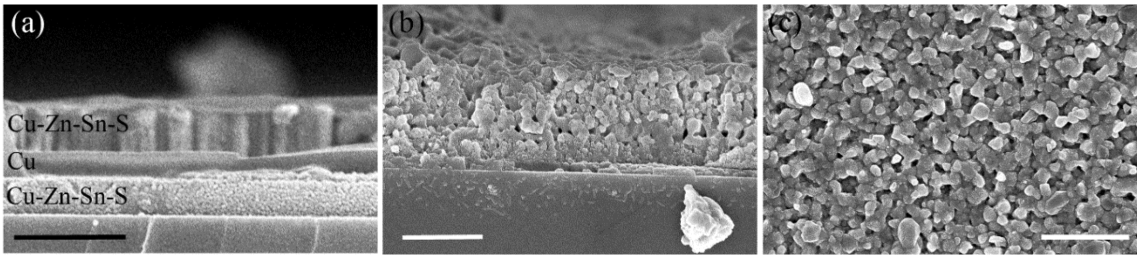

Fig. 3.8: Cross-sectional micrograph of the (a) as-deposited film and (b) the film sulfurized at 500 °C with 1.0 g of sulfur. These films were grown with a Cu interlayer of thickness of ~195 nm. Note that the clear sandwich structure seen in (a) is completely lost in (b), indicating thermally activated diffusion of Cu from the intermediate layer towards both sides and reaction. (c) Surface micrograph of the sulfurized film. The scale bar in FESEM micrographs corresponds to 1 µm.

A mechanism of phase evolution in these films is proposed on the basis of the results of compositional analysis of the films. The elemental composition of the film estimated from the EDS measurements for the samples with varying thickness of the Cu interlayer is shown in Fig. 3.9a. The phase-pure sample was found to be Cu-rich with an average Cu/(Zn+Sn) ratio of 1.25 in contrast to 0.18 obtained for the film without any Cu interlayer. It appears that the improved Cu/(Zn+Sn) ratio drives the reaction pathway leading to the formation of CZTS phase (Inamdar et al., 2013; Olgar et al., 2019; Sun et al., 2011). This is best reflected in Fig. 3.9b where the relative intensities of the secondary phase and CZTS peaks at 26.5° and 28.5°, respectively in the XRD patterns is plotted according to the Cu/(Zn+Sn) ratio in the films. As expected, the relative intensity dropped to zero when the thickness of the Cu interlayer was ~195 nm. The evolution of the kesterite phase in the present case, as mentioned above, is schematically summarized in Fig. 3.9c.

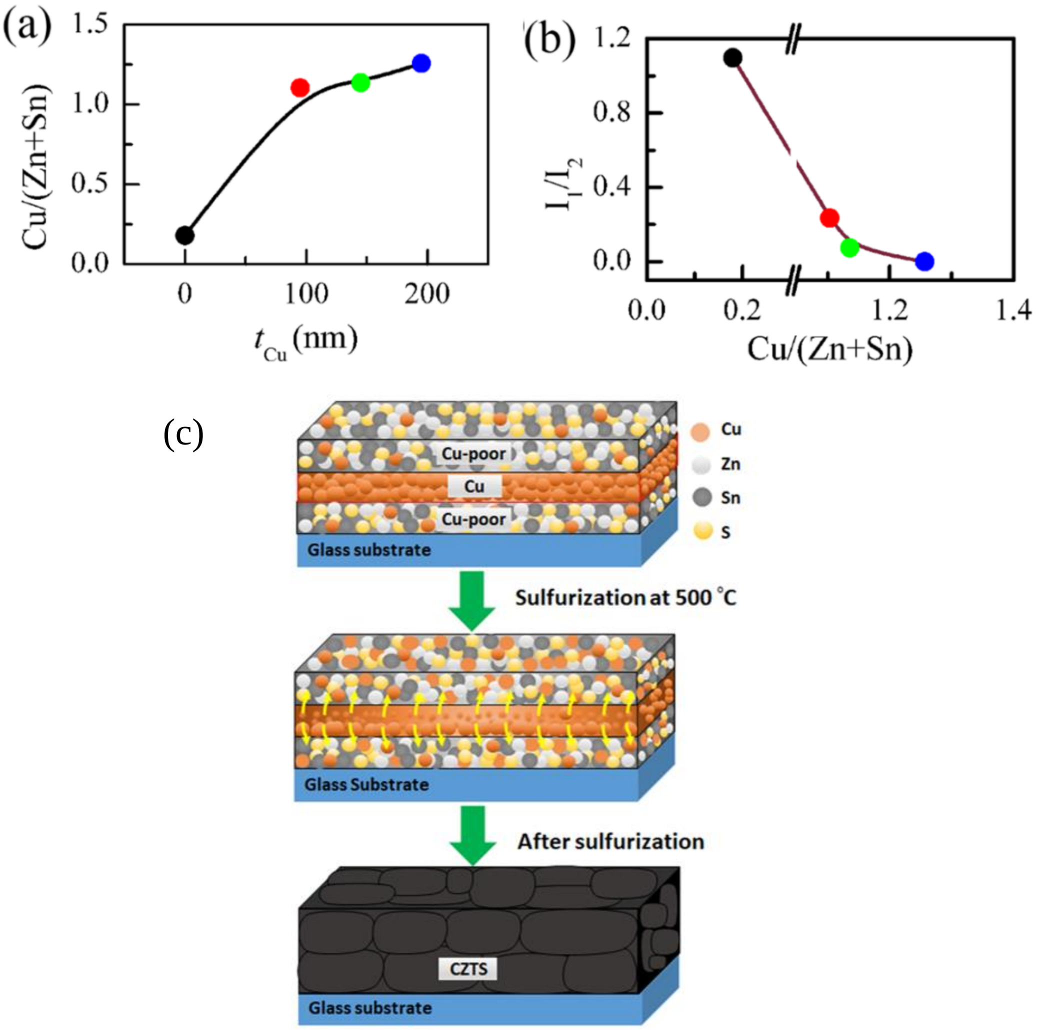

Fig. 3.9: (a) Variation of the Cu/(Zn+Sn) versus the thickness of the Cu interlayer (t_{Cu}); (b) Relative intensities of the secondary phase and the kesterite CZTS XRD peaks at 26.5° and 28.5° as a function of Cu/(Zn+Sn); (c) A schematic representation of the growth mechanism of the phase-pure films facilitated by the Cu interlayer. During sulfurization, Cu out-diffuses into the adjacent Cu-poor regions leading to the formation of a uniform kesterite layer.

3.3.3 Electrical and optical properties of films grown with a Cu interlayer

Figure 3.10a shows the variation in electrical resistivity of the samples measured using the van der Pauw method. The resistivity continuously decreased by an order of magnitude with the increase in the thickness of the Cu interlayer, suggesting strong influence of the secondary phases on the conductivity of the samples (Ren et al., 2020). For example, the secondary phase of tin sulfide, whose presence in our samples have been indicated from the XRD patterns, has high resistivity (Krishnan et al., 2019). Thus, as the fraction of secondary phases decreased in the samples, the overall resistivity of the sample decreased. For the phase-pure film, i.e., the one grown with 195 nm thick Cu interlayer, resistivity was found to be 3.0×10^{-2} Ω-cm, which is similar to the value reported by several other groups (Krishnan et al., 2019; Henry et al., 2016; Tang et al., 2018).

The bandgap of this phase-pure film was estimated using the Tauc's plot of $(\alpha h\nu)^2$ vs hν where α is the absorption coefficient. Using transmittance (T) and reflectance (R) of the films, shown in Fig. 3.10b and c, the absorption coefficient α was calculated as $\alpha = (1/t)\ln[(1-R)^2/T]$ where t is the thickness of the sample. The bandgap of the film was determined to be ~1.58 eV, consistent with the earlier report (Sripan et al., 2017).

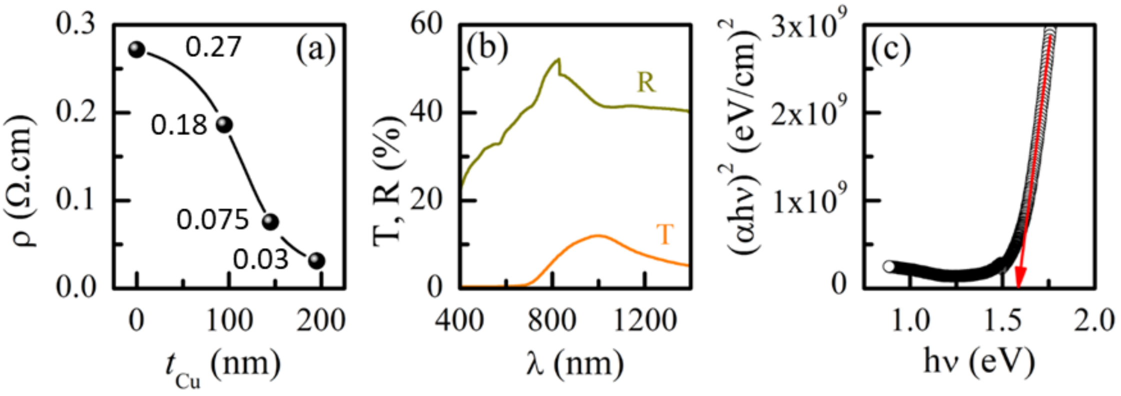

Fig. 3.10: (a) Electrical resistivity as a function of thickness of the Cu interlayer (t_{Cu}); (b) Typical transmittance (T) and reflectance (R) of the phase-pure film (i.e., film grown with ~195 nm thick Cu interlayer) and (c) the corresponding Tauc plot of $(\alpha h\nu)^2$ vs hν.

3.3.4 I-V characterization of the phase pure CZTS thin film

The photoresponse behavior of this phase-pure CZTS thin film was studied to determine its suitability for use as an absorber layer. Figure 3.11a shows the device configuration for the photoresponse studies. The semi log-linear voltage - current characteristics of the phase-pure film, i.e., the one grown with 195 nm thick Cu interlayer, under dark and white light (AM 1.5G, 100 mW/cm^2) illumination are shown in Fig. 3.11b. The sample showed significant improvement in current upon white light illumination. For example at a bias voltage of 3 V, the current increased by about three orders of magnitude from 9.6×10^{-3} mA in dark to 10.0 mA in illumination. The obtained result is consistent with the earlier reports (Rawat et al., 2016; Henry et al., 2017 & 2020; Devi et al., 2019; Gupta et al., 2019). For instance, Rawat et al. (Rawat et al., 2016) have reported 80% enhancement in photosensitivity at 1.0 V in Bi doped Cu_2ZnSnS_4 thin films, while Henry et al. (Henry et al., 2017) presented an increment of ~21.8% at same bias. Similarly, Aruna Devi et al. (Devi et al., 2019) have showed around 60% improvement in the photosensitivity in a CZTSSe thin film gown by selenization of nanocrystal ink. For solution processes CZTS thin films Gupta et al. (Gupta et al., 2019) have reported a similar change in current upon light illumination. More recently, Henry et al. (Henry et al., 2020) have shown a change of 140% in the photosensitivity in a thermally evaporated CZTSe thin film. The obtained results thus indicate good quality of the films comparable to the ones reported in literature.

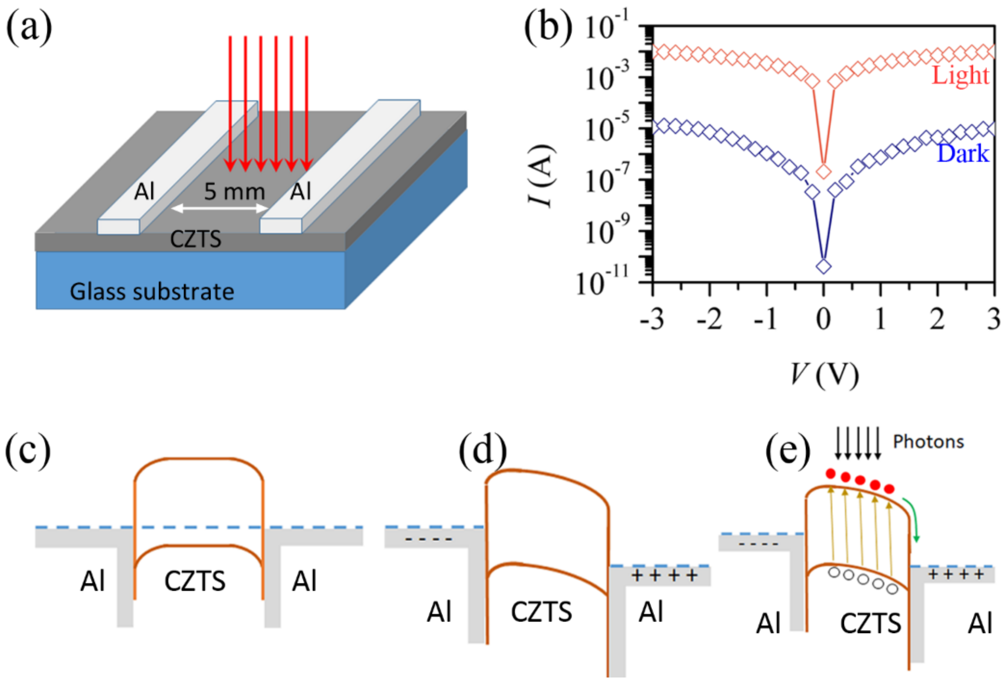

Fig. 3.11: (a) Device configuration for the testing the photoresponse behavior of the phase-pure thin films; (b) Semi log-linear voltage - current characteristics of the phase-pure films under dark and white light (AM 1.5G, 100 mW/cm^2) illumination; Energy band diagrams of the Al/CZTS/Al structure in (c) dark without bias, (d) dark with bias and (e) white light illumination with positive and negative bias.

The underlying mechanism of the remarkable photoresponse behavior of the prepared films is illustrated by a schematic diagram of the band structure at the interface, as shown in Fig. 3.11c-e. When Al and the p-type CZTS come in contact with each other (at no bias and in dark condition, Fig. 8c), transfer of charge carriers occurs due to difference in the work function of Al (Φ_{Al} = 4.06–4.26 eV (Gupta et al., 2019; Lide et al., 2005) and the Fermi level of CZTS (E_F = 4.5 eV (Pandiyan et al., 2017)) that resulted in the formation of a depletion region in

CZTS. When a bias is applied, tilting of the bands leads to an asymmetric band profile across the length of the metal-semiconductor-metal device (Fig. 3.11d) [Tung et al., 2014; Skromme et al., 2003; Baca et al., 1997]. Under illumination and a bias, photons induce electron-hole pairs in CZTS, which are separated and collected by the built-in electric field at the contact and by the applied external field. As illustrated, the resulting band profile (Fig. 3.11e) promotes the separation of the holes and electrons, and their transport and collection at the contacts leading to an enhanced photocurrent.

3.4 Characterization of Ag/p-CZTS/Mo based Schottky junction

Using the above obtained phase pure film (i.e., the one grown with 195 nm thick Cu interlayer), a Schottky junction was fabricated. The junction was made in the form of Glass/Mo/CZTS/Ag structure. The Mo films are typically used as a bottom electrode in the CZTS based solar cells. The typical XRD pattern of the CZTS film grown on Mo coated glass substrates is shown in Fig. 3.12a. The Bragg's peaks at 18.24, 23.16º, 28.47º, 33.03º, 47.35º and 56.19º are attributed to the (101), (110), (112), (200), (220) and (312) planes of CZTS (JCPDS file 26-0575), respectively. This is similar to the result obtained on the glass substrates (Fig. 3.7a), suggesting growth of kesterite CZTS phase. Two other peaks at 40.52º and 73.59º are identified as (110) and (211) planes of cubic Mo (JCPDS file 01-089-5156). Figure 3.12b presents a cross-sectional electron micrograph of the films suggesting coherent interface of the CZTS film on Mo/Glass. It may be noted that formation of a MoS_2 layer during synthesis of CZTS layer on Mo films has been reported by many researchers (Chen et al., 2015). Although it was not possible to detect the MoS_2 layer from the XRD patterns or from the cross-sectional FESEM images, formation of a very thin MoS_2 layer during the high temperature sulfurization process cannot be ruled out.

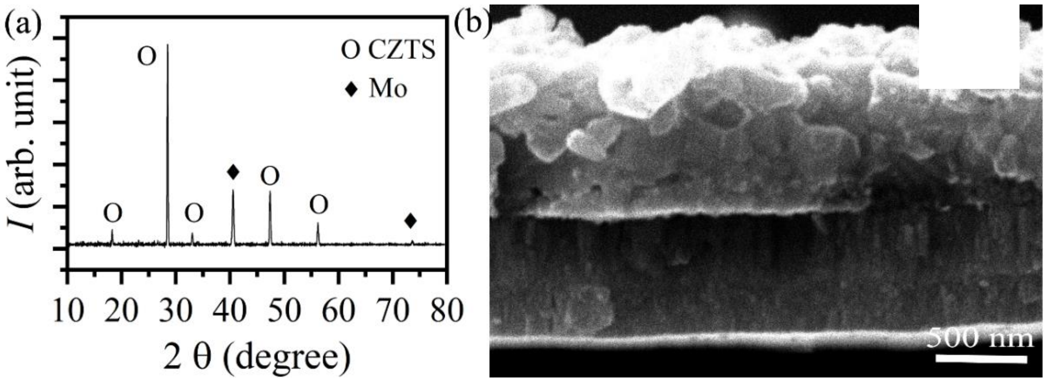

Fig. 3.12: (a) Typical XRD pattern and (b) cross-sectional FESEM image of the CZTS film grown on Mo coated glass substrate.

Figure 3.13 shows the typical dark I-V curve of the Glass/Mo/CZTS/Ag structure. The figure showed a large current in the first quadrant while current remained very low in the fourth quadrant, typical of a Schottky junction. The observed I-V curve is understood on the basis of formation of a Schottky junction between CZTS and Ag. When Ag and the p-type CZTS come in contact with each other (at no bias and in dark condition), the difference in the work function of Ag (Φ_{Ag} = 4.26 eV [Nakayama et al., 1996]) and the Fermi level of CZTS (E_F = 4.5 eV (Katagiri et al., 2005) resulted in the formation of a Schottky barrier. This result is similar to the reported ones (Boutebakh et al., 2017; Atasoy et al., 2019), which indicates the good quality of the prepared CZTS thin films. Furthermore, the saturation in the reverse bias characteristics shows that defect assisted generation or tunnelling mechanism does not exist (Atasoy et al., 2019). The device configuration for the I-V measurement is presented in the inset of Fig. 3.13.

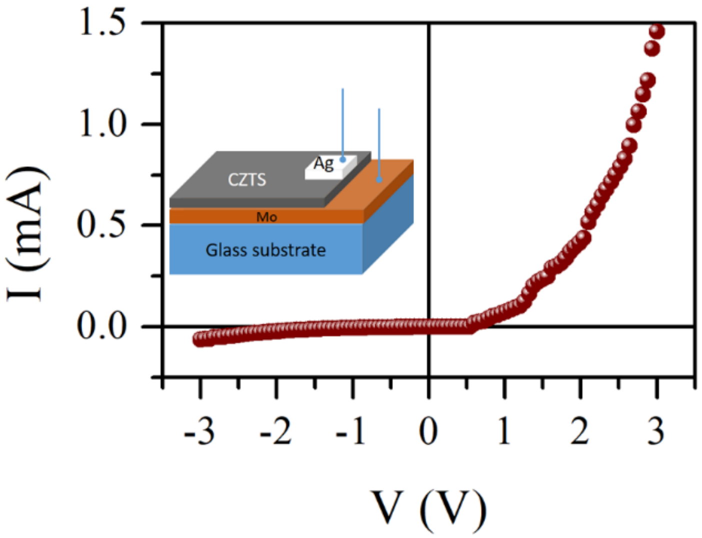

Fig. 3.13: Device configuration and current-voltage characteristics of the Ag/p-CZTS/Mo based Schottky junction grown on glass substrates at room temperature.

In summary, a simple strategy of depositing uniform CZTS thin films with very high white light sensitivity for potential integration in thin film solar cells has been shown. The strategy includes a thin Cu interlayer-mediated control of kesterite phase evolution in the precursor film grown by RF magnetron sputtering of a single elementary target. The films grown without the Cu-interlayer were drastically Cu-poor despite the stoichiometry of the target. Consequently, high fractions of spurious phases were always obtained although a large variation in the sulfurization configuration was adopted. This was overcome by inserting a 195 nm thick Cu interlayer that provided improved compositional stability through thermally activated diffusion of Cu from the intermediate layer towards both sides and the following reaction even at a modest sulfurization temperature of 500 °C. The obtained phase-pure films were found to have a bandgap of 1.58 eV and very high white light sensitivity, typically that required for a potential absorber layer in thin film solar cells.

CHAPTER 4

GROWTH OF FILMS FROM A TARGET WITH EXCESS Cu

Although synthesis of phase pure CZTS thin films using single target by sputtering technique, appears very attractive, growth of secondary phases arising as a consequence of stoichiometric deviation stemming from variation in sputter yield of the target elements (especially Cu) remains a challenge (Chapter 3). Sputtering deposition from a target with stoichiometric composition always yielded impure phases in spite of wide variation in the sulfurization parameters (Chapter 3). In order to compensate the Cu loss due to its poor sputter yield, a sputter target with excess Cu was prepared. This chapter deals with films prepared from a target containing 12.5% excess Cu.

It may be mentioned here that all routes of synthesis of CZTS thin films involve a two-step process, i.e., deposition of a precursor film followed by its annealing at temperatures > 500 °C in a sulfur-containing gaseous environment. The process parameters during annealing such as dwell time, temperature and sulfur amount, play a very important role in the evolution of phase and microstructure of the CZTS films. As outlined in the Chapter 1, for the phase formation of CZTS, high temperature (~500 °C) annealing required. However, annealing at such high temperature may lead to loss of volatile elements that may result in significant deviation from the intended composition. Consequently, this may hinder the CZTS phase formation and enhance the growth of multiple secondary/ternary phases. These secondary phases may lead to a highly porous microstructure, which is not desirable for photovoltaic application. Alternatively, many groups have suggested that the loss of the volatile elements can be suppressed by maintaining sufficient partial sulfur pressure during high temperature annealing (Scragg et al., 2011; Sun et al., 2018). In this chapter, the influencing mechanism of post-sulfurization process on phase evolution has been elucidated from systematic variation in the dwell time, temperature and the sulfur amount.

A single elementary target was prepared by using powders of elemental Cu, Zn, Sn and S. An excess amount by 12.5% of Cu was taken. The excess amount of Cu in the target was taken to compensate the Cu loss during sputtering of target with stoichiometric elemental proportions arising due to variation in sputter yield of elements (Pandey and Mohanty, 2021). The details of the target preparation are mentioned in the Chapter 2. The CZTS films were deposited on soda lime glass (SLG) substrates at room temperature by RF-magnetron sputtering using the as-pressed targets. For all depositions, a base pressure lower than $4.0\times10^{-}$

^{6} mbar, was achieved. Argon was admitted to maintain a working pressure of 1.0×10^{-2} mbar. Deposition was carried out at constant RF power of 75 W. The thickness of the film was about 600 nm. These precursor films were sulfurized at 500 and 550 °C for durations of 10, 30 and 60 minutes in a tubular furnace. Sulfur flakes were used as sources of sulfur and the sulfurization was carried out in the presence of flowing argon. Figure 4.1 shows the sulfurization configuration and the heating profile.

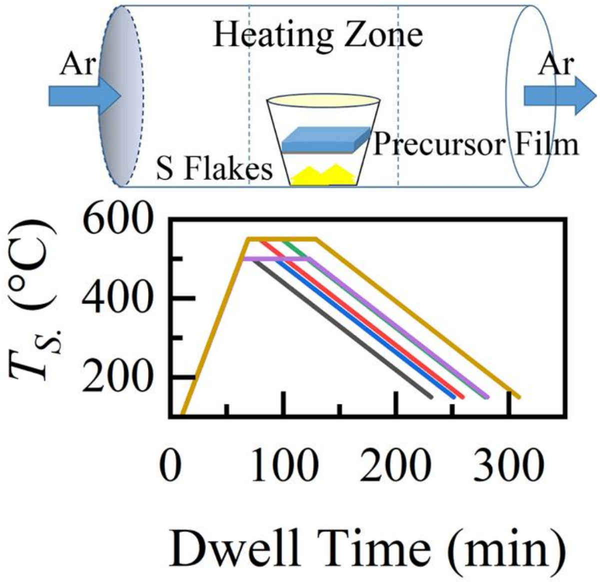

Fig. 4.1: Schematic diagram of configuration and heating profile for the sulfurization of precursor thin films at 500 and 550 °C for different dwell times.

4.1 Phase evolution in thin films

The evolution of phase and crystallinity of the CZTS thin films are strongly dependent on the sulfurization parameters such as dwell time and temperature (Fernandes et al., 2013; Olgar et al., 2019, Olgar, 2019; Emrani et al., 2013). While a sulfurization temperature > 500 °C is typically desired, (Katagiri et al., 1997; Jiang et al., 2018; Zhang et al., 2013) the required dwell time varies greatly depending on the precursor film composition. For example, Thota et al. reported the growth of phase pure CZTS films from sulfurization of sputtered metallic stacks for 120 mins at 500 °C (Thota et al., 2017). On the other hand, Dalapati et al. prepared films of similar quality for sulfurization for 10 min at same temperature (i.e., sulfurization at 500 C) (Dalapati et al., 2015). For our work, Figures 4.2a and 4.2b show comparative XRD patterns of the films sulfurized at 500 and 550 °C for 10, 30 and 60 minutes with 1.0 g of sulfur. For a dwell time of 10 min at 500 °C, several sharp peaks indicating well-crystallization of the film were obtained. The peaks at 28.5°, 38.0°, 47.5° and 56.3° are identified with (112), (211), (220) and (312) planes of kesterite CZTS (JCPDS file: 26-0575), respectively. The additional peaks, namely at 26.5, 34.0 and 51.8° correspond to secondary phases and are marked by an asterisk (*) in the XRD pattern. For instance, the peaks at 26.5° and 51.8° are identified with (021) and (221) planes of orthorhombic SnS (JCPDS file: 3-065-3875) (Sun et al., 2018) or (100) and (103) planes of ZnS (wurtzite) (JCPDS file: 01-072-0162) (kissani et al., 2016). The other peak at 34.0° is identified as (211) of orthorhombic SnS (JCPDS file: 3-065-2610). When the sulfurization duration was increased, the intensity of the peaks corresponding to the secondary phases decreased progressively and the peaks disappeared completely for sulfurization for 60 mins at 500 °C (Fig. 4.2a). The progressive decrease in the secondary phases can be seen from Fig. 4.4a wherein the intensity ratio (I_1/I_2) of the secondary phase peak at 26.5° to the (112) peak of CZTS (at ~28.5°) with the sulfurization duration has been plotted.

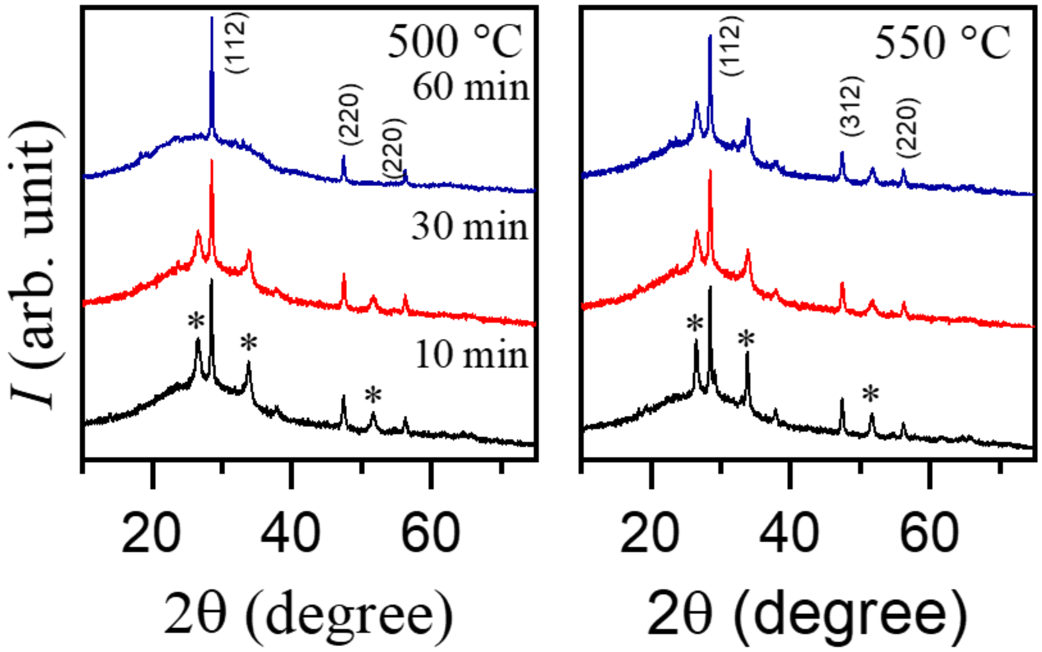

Fig. 4.2: Typical XRD pattern of the films sulfurized at (a) 500 and (b) 550 °C with 1 g of sulfur flakes for different dwell time. The symbol (*) represents secondary phases (Please refer to text for details).

The phase purity of the sample (i.e., the one sulfurized for 60 min at 500 °C) was further confirmed from the Raman spectrum shown in Fig. 4.3. The spectrum reveals two strong peaks at around 285 and 332 cm^{-1} corresponding to the A1 symmetry of kesterite phase (Fernandes et al., 2011). A small shoulder at 363 cm^{-1} that also corresponds to CZTS phase is also noticeable. A photograph of this film is presented as inset to Fig. 4.3.

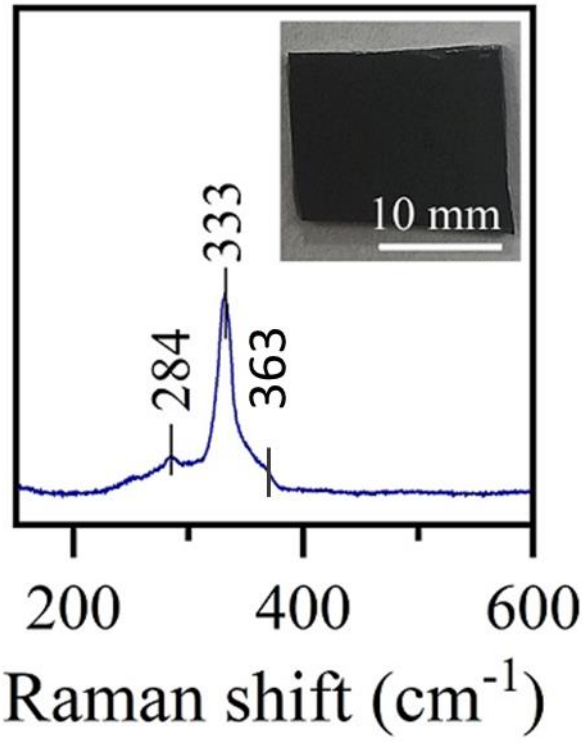

Fig. 4.3: Raman spectrum and photograph (inset Fig. 4.3) of the phase pure thin film (i.e., the film annealed at 500 °C for 60 min with 1 g of sulfur).

On the other hand, sulfurization at 550 °C yielded secondary phases irrespective of the dwell time (Fig. 4.2b). Although the intensity ratio I_1/I_2 decreased considerably for increase in dwell time from 10 to 30 min, there was marginal decrease thereafter (Fig. 4.4a). The persistence of secondary phases even after sulfurization at such a high temperature and for a longer duration is quite surprising, considering many available reports of growth of phase pure films for sulfurization in similar conditions (He et al., 2013; Gupta & Mohanty, 2019; Chalapathi et al., 2015).

This result, against the expected accelerated reaction between the binary/ternary compounds to yield kesterite phase at higher sulfurization temperature and dwell time, is most likely due to the deficiency of sulfur, which might have caused a decomposition reaction (Scragg et al., 2011). Sun et al. suggested that deficiency of the chalcogenide and/or volatile elements in the system may lead to the evolution of the binary/ternary phases (Sun et al., 2018). For the shorter sulfurization time at 500 °C, the system was found sulfur deficient (S/(Cu+Zn+Sn) = 0.85 as shown in Fig 4.4b, which resulted in the growth of metal sulphide phases. With further increase in sulfurization time, this ratio improved and for 60 min of sulfurization, the S/(Cu+Zn+Sn) ratio reached to the approximate stoichiometric value of 0.98, which yielded the growth of kesterite CZTS. It suggests that a short sulfurization duration is not sufficient for homogeneous mixing of metallic precursor with sulfur and their reaction (Fernandes et al., 2013; Thota et al., 2017; Olgar, 2019).

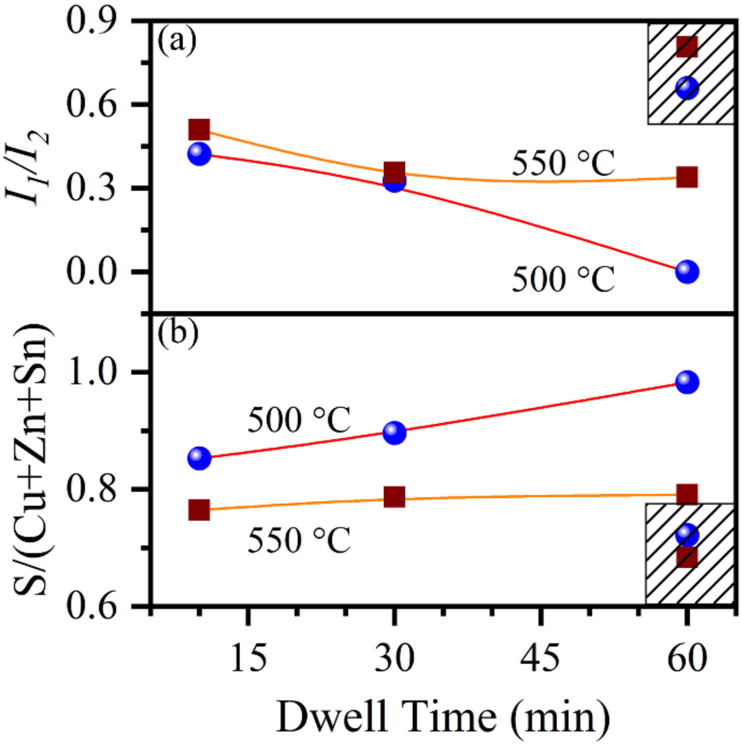

Fig. 4.4: Variation in the (a) XRD peak intensity ratio (I_1/I_2) of secondary phase (I_1) at 26.5° and kesterite CZTS (I_2) at 28.5° and (b) S/(Cu+Zn+Sn) as a function of dwell time of the films sulfurized at 500 and 550 °C with 1.0 g of sulfur flakes. The shaded portion represents the same for films sulfurized at 500 and 550 °C with 0.5 g of sulfur flakes. Composition of the films was determined by EDS analysis carried out at multiple points of the sample surfaces.

In the case of sulfurization at 550 °C, the S/(Cu+Zn+Sn) ratio is significantly lower than the stoichiometric proportion. With increase in dwell time from 10 to 60 min, the S/(Cu+Zn+Sn) ratio increased marginally from 0.76 to 0.79. It is believed that with 1.0 g of sulfur, sulfurization at 550 °C proceeds mainly in an S-deficient environment, which prevents the sustained formation of CZTS (Ren et al., 2017; Redinger et al., 2011). The other possible reason of the evolution of secondary phases at this stage might be due to the loss of volatile element like Sn that led to the decomposition reaction (Sun et al., 2018; Jiang et al., 2018). Sun et al. have also reported that the rate of decomposition may be accelerated at elevated temperature and the resulting films would contain SnS, Cu-S and ZnS phase along with the CZTS (Sun et al., 2018).

In order to verify that sulfur deficiency is the plausible cause of the presence of the secondary phases, additional experiments were carried out with 0.5 g of sulfur flakes as sulfur source. Figure 4.5 shows XRD patterns of the films sulfurized as 500 and 550 °C for 60 min, but with 0.5 g of sulfur flakes. Multiple peaks corresponding to spurious phases were obtained for both the samples that validates our hypothesis of strong interdependence of sulfur amount, sulfurization temperature and duration. The peak intensity ratio I_1/I_2 (Fig. 4.4a) was 0.65 for sulfurization at 500 °C while that for 550 °C was 0.80. It is worth noting that these values are significantly higher than the values obtained for the samples sulfurized with 1.0 g sulfur (0 vs 0.65 at 500 °C and 0.4 vs 0.8 at 550 °C). As expected, the S/(Cu+Zn+Sn) ratio was very poor (i.e., 0.72 for 500 °C and to 0.68 for 550 °C), as noted from Fig. 4.4b.

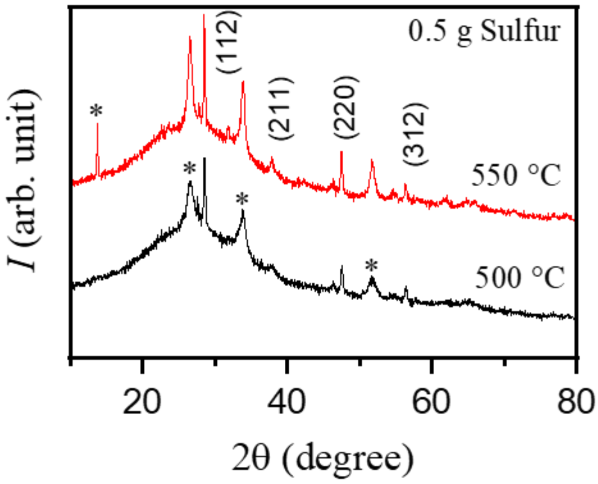

Fig. 4.5: Typical XRD pattern of the films sulfurized at 500 and 550 °C with 0.5 g of sulfur flakes for 60 min. The symbol (*) represents secondary phases (Please refer to text for details).

It might appear that Cu-deficiency (as prepared from a stoichiometric target) does not make CZTS a good absorber. In fact, Cu poor and Zn rich condition in CZTS is beneficial for high efficiency thin film solar cells. One of the major issues in the CZTS based devices is the large V_{oc} deficit, which has been attributed to the abundant point defects (especially, antisite defects) and associated band tailing. The processing of the CZTS films can be designed to reduce some antisite defects. For example, growing films in Cu-poor and Zn-rich conditions can reduce the Cu_{Sn} and Sn_{Zn} antisite defects and their clusters. However, owing to a narrow range of single phase stability in the Cu-Zn-Sn-S phase diagram, the composition cannot be very far from the stoichiometric one. Films grown from a stoichiometric target were extremely Cu-poor (as shown in Fig. 3.6). In such Cu deficiency, it was very difficult to prepare phase pure films (for example, Fig. 3.4 and 3.5), and hence required intervention in terms of an additional Cu layer (Chapter 3) or excess Cu in the target (Chapter 4).

4.2 Surface feature of the films

Figure 4.6 shows surface microstructure of the corresponding films (i.e. films sulfurized at 500 and 550 °C with 1 g of sulfur for various durations). It is interesting to note that although the XRD patterns were almost similar, except the one sulfurized at 500 °C for 60 min with 1.0 g of sulfur, surface of the films shows very contrasting features. Since the typical growth process of CZTS includes reaction between binary sulfide phases, the eventual microstructure of the films is decided by the phase segregation (Amal & Kim, 2013; Wang et al., 2017; Yoo et al., 2012; Kumar et al., 2019). The film sulfurized at 500 °C with 1.0 g sulfur for 10 min showed a highly porous film (Fig. 4.6a). The presence of Zn and Sn sulphide phases in the film causes the agglomeration or segregation of the nano particles on the top surface, as reported (Tumbul et al., 2021; Thanh et al., 2014; Chalapathi et al., 2015; Sun et al., 2018). The presence of secondary phases in addition to kesterite CZTS, as determined by XRD analysis, is believed to be responsible for the observed porous microstructure of the films. By increasing the dwell time to 30 min, although the films get densified, severe porosity is still retained. Dwelling time of 60 min (that yielded phase pure films), however, resulted in a very different microstructure. A smooth and denser uniform microstructure is observed this film (inset to Fig. 4.6c). The average particle size is found to be about 100 nm. On surface, pin hole-like features are observed which are responsible for the voids inside the films as seen from the cross-sectional image (inset to Fig. 4.6c). The overall thickness of this film is ~800 nm.

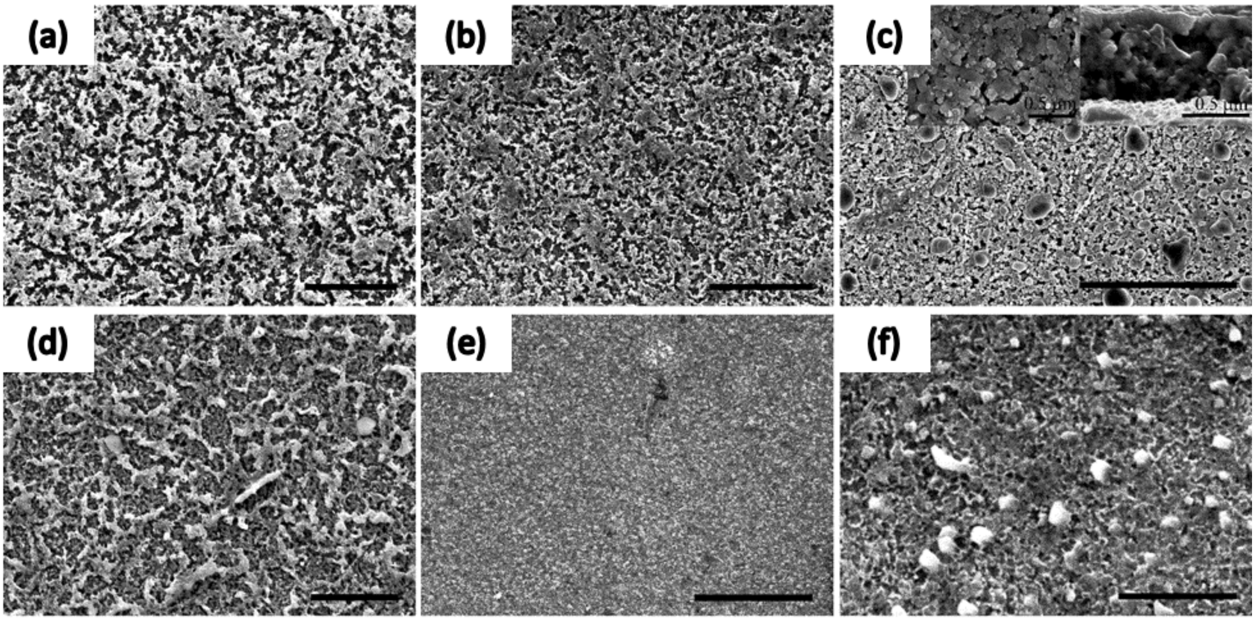

Fig. 4.6: Surface micrographs of the films sulfurized at (a-c) 500 °C and (d-f) 550 °C for 10, 30 and 60 min with 1.0 g of sulfur flakes. The inset to (c) shows the cross-sectional and magnified view of the surface micrograph. The scale bar in (a-f) corresponds to 5 µm.

The trend of evolution of microstructure with dwell time for the samples sulfurized at 550 °C is however very different from that of the 500 °C - sulfurized samples. A surface characterized by connected ridge-like features was observed for the sample sulfurized for 10 min at 550 °C. Thota et al. have suggested that high sulfurization temperature for lesser duration led to the formation of phase pure kesterite with better microstructure, (Thota et al., 2017) which however is not the case in the present work. The volumetric contraction arising from the evaporation of volatile products led to the enhancement of the voids and cracks in film upon increasing the sulfurization temperature from 500 to 550 °C (Kissani et al., 2016). With increase in dwell time, the films gets densified. A compact surface covered with very fine particles was observed for the 30 min-sample. With further increase in the sulfurization duration to 60 min, the partially segregated particles and voids are observed on the film surface as shown in Fig. 4.6f.

4.3 Electrical and optical properties of the phase pure film

The presence of the secondary phases was found to have clear signature in the measured electrical resistivity of the samples. Figure 4.7 shows the variation in electrical resistivity with dwell time for the film sulfurized at 500 and 550 °C. As expected, with decrease in the fraction of the secondary phases, the resistivity of the films decreased. The resistivity of phase pure

CZTS film was determined to be 0.21 Ω-cm, which is similar to the earlier reported values (Henry et al., 2016).

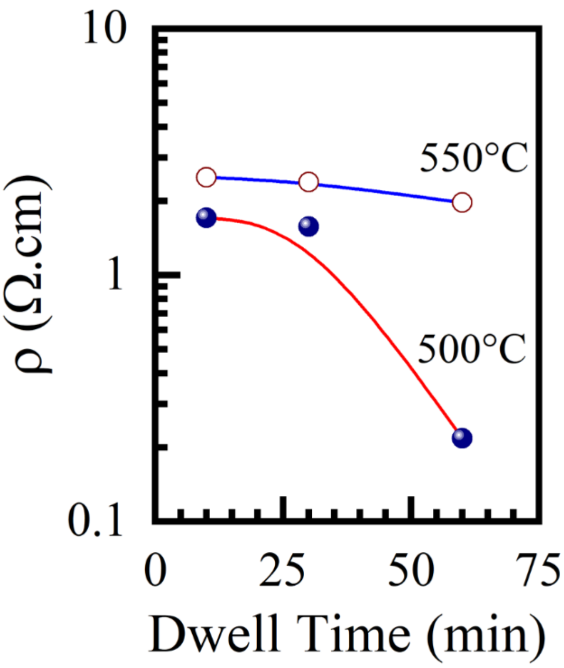

Fig. 4.7: Variation in electrical resistivity with dwell time for sulfurization at 500 and 550 °C with 1.0 g of sulfur flakes.

The optical bandgap of this phase pure sample was found to be 1.58 eV, as estimated from the Tauc plot of $(\alpha h\nu)^2$ versus hν (Fig. 4.8), where α is the absorption coefficient and hν is the incident photon energy. The values of absorption coefficient α was determined from the transmittance (T) and reflectance (R) of the film measured in the range of 300 -1400 nm. The obtained bandgap value is typical of the CZTS thin films reported earlier (Henry et al., 2016; Sripan et al., 2017; Pandey & Mohanty, 2021).

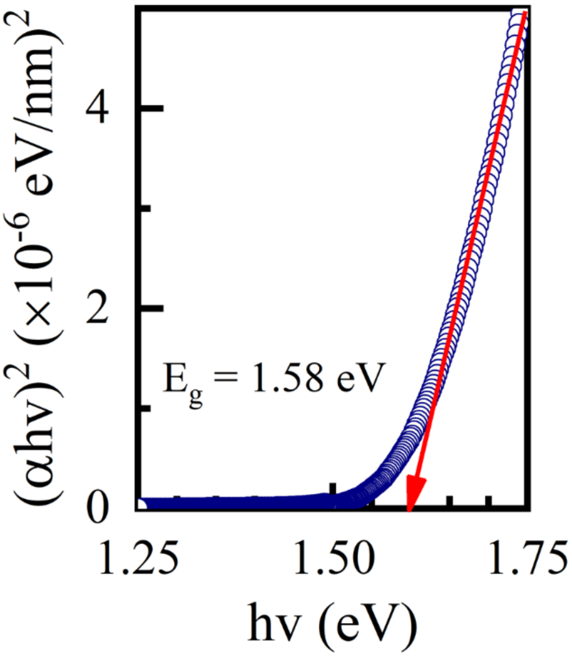

Fig. 4.8: Tauc plot of $(\alpha h\nu)^2$ versus hv of CZTS film sulfurized at 500 °C for 60 min.

4.4 Current- Voltage (I-V) characteristics of Ag/ p-CZTS junction

A junction between the phase pure CZTS and Ag was fabricated on Mo coated glass substrate. The device configuration is given as inset to Fig. 4.9. Figure 4.9 shows the characteristic *I-V* curve of the device that depicts a non-linear relationship revealing a Schottky contact between Ag and CZTS. However, the observed I-V curve suggests considerable deviation (for larger applied bias) from that of an ideal Schottky contact due to the presence of series resistance R_s induced by the Ag/CZTS interface, and hence the classical expression for the I-V characteristic can't be adapted for the given case. Incorporating R_s, the expression for current can be given as (Sze et al., 2021):

$$I \approx I_s \exp\left(\frac{q(V-R_sI)}{\eta kT}\right) \qquad (1)$$

where I_s is the saturation current, η is the ideality factor, T is the absolute temperature, k is the Boltzmann constant and R_s is the series resistance. For small current region in forward bias, the current is order of the saturation current, and hence the product R_sI becomes negligible. Therefore, the value of I_s can be calculated by extrapolating the linear region of the forward bias semi log *I-V* curves to the zero applied voltage (V = 0) (shown in Fig. 4.10), which yields I_s = 6.5 µA. The slope of the linear region of this curve provides an estimate of $q/\eta kT$, i.e., $\eta = \left(\frac{q}{kT}\right)\left(\frac{1}{d\,lnI/dV}\right)$. The value of η at room temperature (~295 K) was determined to be 4.5. The obtained value of η is, however, much larger than the ideal value ($1< \eta < 2$) predicted on the lines of thermionic emission based conduction mechanism. Higher ideality factors have been reported earlier for heterojunctions including those of CZTS thin films and for p-n junctions Boutebakh et al., 2017; Shah et al., 2003; Ben-Chorin et al., 1995; Jing-Jing et al., 2010; Gopal et al., 2015; Liao et al., 2018; Servaites et al., 2011; Gezgin et al., 2019).

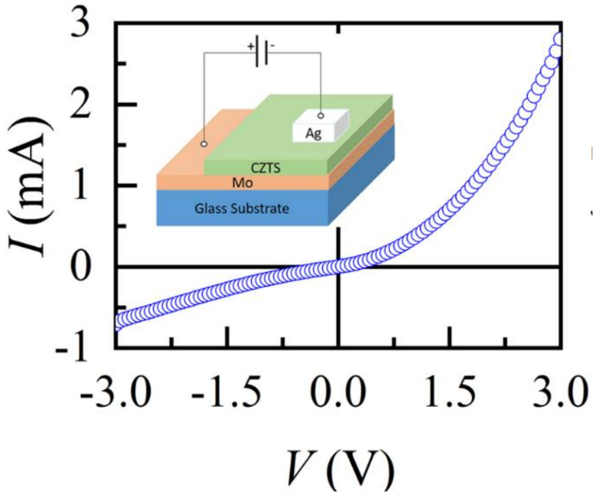

Fig. 4.9: Device configuration (inset) and typical I-V curve of Ag/p-CZTS/Mo based Schottky junction.

The higher values of ideality factor stem from the quality of the junction and the current conduction mechanism. For example, when the contact is not Ohmic (as expected from the work function differences between Ag and CZTS in this case), the heterojunction can be modeled as a series of diodes and resistors in series, wherein the ideality factor can be considered as sum of ideality factor of the individual diodes (Shah et al., 2003). On the other hand, presence of pinholes and cracks might lead to low shunt resistance and hence a large leakage current, which yields a high ideality factor (Gopal et al., 2015; Liao et al., 2018; Servaites et al., 2011; Gezgin et al., 2019). Defect states in the semiconductor bandgap may also be one of the reasons of high ideality factor (Werner et al., 1991). It is believed that one or more of the above mentioned factors are operational in the present work that drives the ideality factor to such a high value.

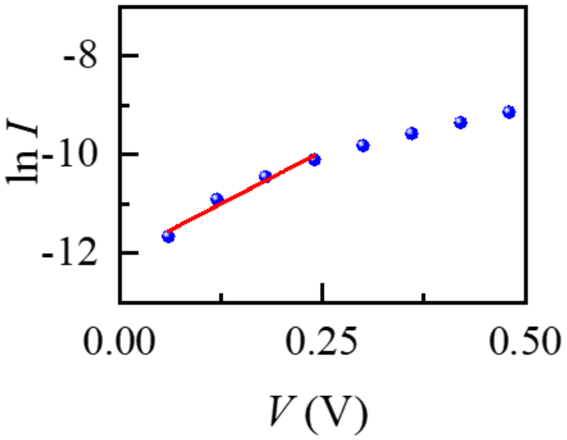

Fig. 4.10: Linear region of the logarithm of current ln (I) vs forward bias voltage (V) plot of Ag/p-CZTS/Mo based Schottky junction. The solid line indicates the linear fit to the data points at low forward bias voltage.

It may be noted here that series resistance R_s cannot be estimated directly from the conventional method of analysis of the current-voltage characteristics given in Eq. (1). One can find in literature that the series resistance is determined by approaches suggested by Norde (Norde, 1979) and by Cheung and Cheung (Cheung & Cheung, 1986). However, Norde's method works well when $\eta = 1$, and hence cannot be applied in the present case. On the other hand, Cheungs' method requires that the plot of d*V*/dln(*I*) vs current (*I*) remain linear. In our case, the plot shows a non-linear character for the range of measured values of *I*. The inapplicability of the Cheung's method suggests that the fabricated device considerably differs from a simple metal-semiconductor Schottky junction. Nevertheless, the series resistance R_s of the device was estimated, at least qualitatively, from the dynamic resistance calculated as R_i = d*V*/d*I* (Fig. 4.11). As seen from Fig. 4.10, the semi log I- V characteristic deviates significantly from linearity at higher values of forward bias. This suggests that the series resistance becomes increasingly dominant at higher forward bias voltages due to higher voltage drop IR_s in Eq. (1). Thus, we have used R_i vesrus *V* plot to estimate the series resistance. As expected, at higher forward bias voltages, R_i becomes nearly independent of applied voltage and may correspond to the value of series resistance R_s of ~431 Ω.

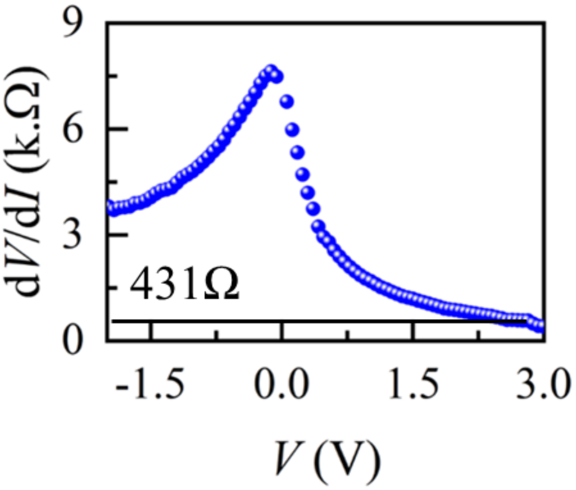

Fig. 4.11: Bias-dependent resistance (dV/dI) vs applied voltage (V) graph of Ag/p-CZTS/Mo based Schottky junction.

In summary, we have shown the growth of phase pure kesterite CZTS thin films by RF magnetron using a single elementary target followed by post-sulfurization. The effect of sulfurization temperature, dwell time and sulfur amount on the phase and microstructural evolution of the films has been studied. As confirmed from XRD and Raman measurements, phase pure CZTS is obtained for sulfurization at 500 °C for 60 min with 1.0 g of sulfur in a quasi-open environment. Electrical resistivity and the bandgap of the phase pure CZTS film were 0.21 Ω.cm and ~1.58 eV, respectively, which are similar to the reported value. I-V measurement of a device of Mo/CZTS/Ag configuration showed typical features of Schottky contact. Analysis of the current voltage characteristic of the device from the conventional thermionic emission model revealed saturation current, ideality factor and series resistance to be 6.5 µA, 4.5 and 431 Ω, respectively.

CHAPTER 5

SINGLE STEP PROCESSING OF CZTS THIN FILMS FROM A TARGET WITH EXCESS Cu

In the previous chapter, it was shown that the phase pure CZTS thin films can be prepared by RF magnetron sputtering from a single elementary target containing excess Cu followed by sulfurization at 500 C for 60 min with 1 g of sulfur. The studies revealed a very critical dependence of phase evolution on sulfurization parameter. In this chapter, we have shown that the post-deposition annealing process can be completely eliminated by using a high substrate temperature during deposition of the precursor films. Substrate temperature is a key growth parameter, which can affect the composition, phase and morphology of the film due to the increase surface mobility of the arriving atoms. The thermal energy required for the reaction and phase formation can be provided via intuitive manipulation of the substrate temperature that can assist to the formation of the kesterite phase. According to the reported literature, the films grown at substrate temperatures $T_s \leq 300$ °C had issues of crystallization (Jheng et al. 2014) whereas $T_s \geq 500$ °C resulted in decomposition of the films yielding secondary phases (Emrani et al., 2013). Thus, an optimum substrate temperature can facilitate the growth of CZTS thin films and forms the basis of this chapter.

The thin films were grown by RF magnetron sputtering using a single elementary target (2 inch diameter) containing 12.5% excess Cu. During deposition the substrate temperature varied from 200 to 500 °C. More details of preparation of the target and sputtering configuration have been discussed in the Chapter 2. The deposition was carried out at a RF power of 75 W for a duration of 75 min. The chamber was evacuated to a base pressure better than 4.0×10^{-6} mbar. High purity (>99.9%) Ar was admitted to the chamber and the working pressure was maintained at 4.5×10^{-3} mbar. After deposition, the heaters were switched off and the substrate holder was allowed to cool naturally in the presence Ar. The substrates were taken out of the chamber once the substrate holder was cooled to room temperature for further characterization.

5.1 Evolution of single phase CZTS

Reaction pathway and hence, the kesterite phase evolution during the synthesis of CZTS thin films is strongly influenced by the heat treatment process (Nguyen et al., 2015; Katagiri et al., 2001; Olekseyuk et al., 2004; Olgar et al., 2019; Ren et al., 2017; Scragg et al., 2011). While the post-deposition sulfurization facilitates reaction of elements/binary compounds in the precursor film to form CZTS, (Ren et al., 2017; Scragg et al., 2011) the effects of the in-situ heat treatment in the form of elevated substrate temperature during the deposition are inherently complex. A suitably high substrate temperature will provide the depositing species thermal energy that may possibly lead to the formation of CZTS as the layer grows on the substrate (Jheng et al., 2014). In the present case, deposition of films at substrate temperatures (T_s) up to 300 °C were devoid of any crystalline phase, as evidenced from the XRD patterns (Fig. 5.1a). This is in contrast to the earlier reports of growth of kesterite CZTS films at substrate temperatures as low as 200 °C (Jheng et al., 2014). On the other hand, deposition at 400 °C yielded crystalline phases as characterized by two peaks at 28.5° and 31.0° (Fig. 5.1a). These peaks were identified with the (112) plane of CZTS (JCPDS file: 00-026-0575) and (112) plane of Cu_4SnS_4 (JCPDS file: 00-029-0584). With increase in substrate temperature to 450 °C, the secondary phase peak (i.e., the one at 31.0º) completely disappeared and two additional peaks were induced at 47.3° and 56.3°. These peaks are attributed to the (220) and (312) planes of CZTS (JCPDS file: 00-026-0575), respectively, suggesting the growth of phase pure CZTS thin films. Upon further increase in the substrate temperature to 500 °C, a few additional peaks appeared at ~26.6°, 31.0°, 44.0° and 52.1°. The peaks at 26.6°, 31.0°, 44.0° and 52.1° are due to the (111), (200), (220) and (311) of CuS_2 (JCPDS file: 03-065-4850) or (220), (112), (611) and (323) of Cu_4SnS_4 (JCPDS file: 00-029-0584) phase. The peaks at 26.6° and 52.1° may also be ascribed to the (100) and (103) planes of ZnS (wutzite). The appearance of these several peaks corresponding to the secondary phases is believed to stem from the possible decomposition of the CZTS due to higher thermal energy associated with an increased substrate temperature, as prescribed in Eq. (1) (Scragg et al., 2011)

$$Cu_2ZnSnS_4\,(s) \Leftrightarrow Cu_2S\,(s) + ZnS\,(s) + SnS\,(s) + \tfrac{1}{2}\,S_2\,(g);\ SnS\,(s) \Leftrightarrow SnS\,(g) \qquad (1)$$

It is also evident from reports of many groups, who have shown that a higher sulfurization temperature or higher duration leads to the decomposition reaction resulting in the growth of spurious phases (Weber et al.,2010; Sun et al., 2018).

A qualitative measure of phase purity of the films was carried out by plotting the peak intensity ratio corresponding to the CZTS phase (peak at 28.5º) and the secondary phase peak (peak at 31.0º) as shown in Fig. 5.1b. As expected, the relative intensity ratio decreased to zero when the substrate temperature T_s was increased from 400 to 450 °C, which however increased to 1.2 upon increasing T_s to 500 °C.

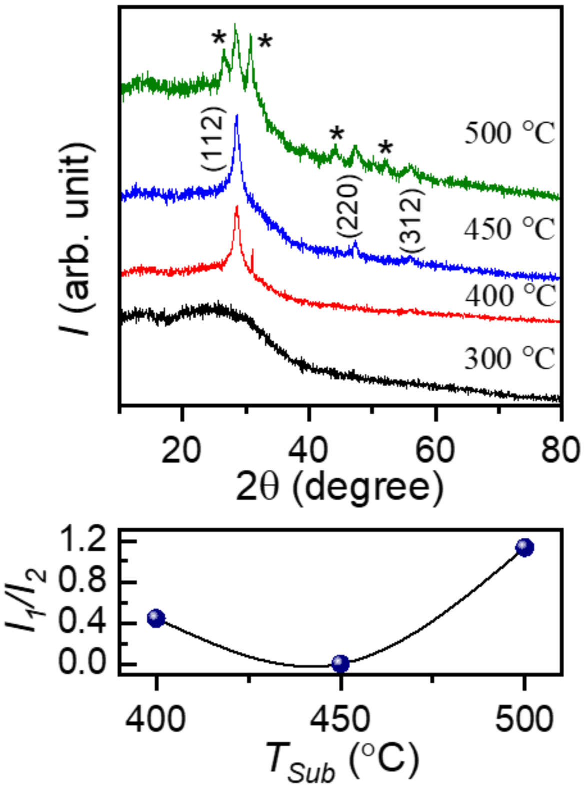

Fig. 5.1: (a) Typical XRD patterns of the films grown at substrate temperature of 300, 400, 450 and 500 °C, respectively and (b) relative intensities of secondary phase at 31° and (112) peak of CZTS from the XRD patterns with respect to substrate temperature. The asterisk (*) shows secondary phases (Please refer to text for details)

Raman spectroscopy was carried out to further confirm the phase purity of the film grown at T_s = 450 °C. The spectrum shown in Fig. 5.2 is characterized by a small peak at 284 cm^{-1} and two super imposed peaks at 334 and 363 cm^{-1}. These peaks clearly indicate the formation of kesterite CZTS (Fernandes et al., 2011).

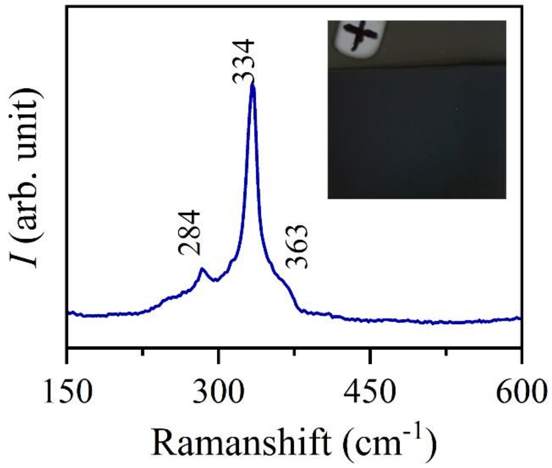

Fig. 5.2: Raman spectrum of the phase pure CZTS film grown at T_s = 450 °C. The actual photograph of the film is presented in the inset.

5.2 Surface feature of the films

The surface microstructure of the films grown at substrate temperature of 300, 400, 450 and 500 °C are presented in the Fig. 5.3a-d. All films showed a dense crack-free microstructure albeit significant differences in the surface features of the films grown at different substrate temperatures. The film deposited at 300 °C exhibited a non-uniform surface microstructure characterized by crystallites of two different sizes (Fig. 5.3a). With increase in substrate temperature, the number density of larger crystallites decreased rapidly and a uniform microstructure was observed. For example, for the films grown at 450 °C (Fig. 5.3c), a smooth and very uniform surface microstructure was observed. A higher processing temperature i.e. 500 °C led to formation of finer crystallites (Fig. 5.3d), possibly due to decomposition reaction of the CZTS (Scragg et al., 2011; Sun et al., 2018).

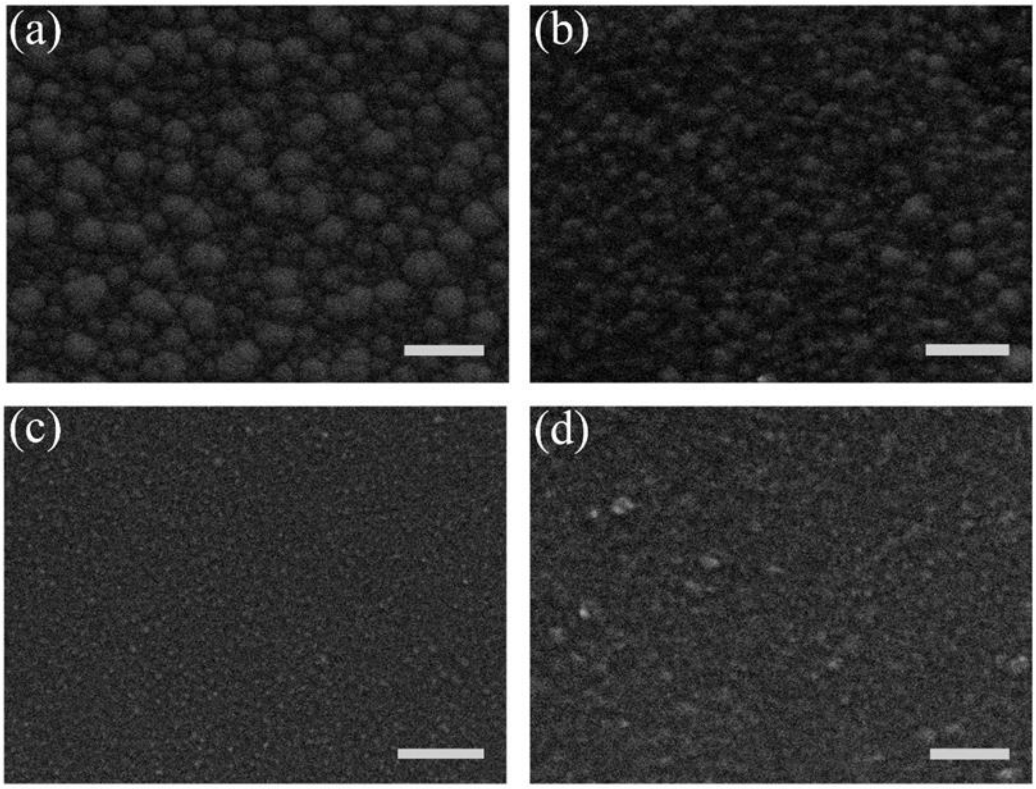

Fig. 5.3: (a-d) Representative SEM images of the films grown at substrate temperature of 300, 400, 450 and 500 °C, respectively. The scale bar in the SEM images corresponds to 500 nm.

5.3 Optical properties of the film prepared at 450 °C

The bandgap of this phase pure film was estimated from the Tauc's plot of $(\alpha h\nu)^2$ vs $h\nu$ (Fig. 5.4), where α is the absorption coefficient and hν is the photon energy. The absorption coefficient was calculated from the measured transmittance and reflectance curves of the films. The extrapolation of the linear region in the $(\alpha h\nu)^2$ vs $h\nu$ plot yielded the bandgap to be ~1.6 eV, which is similar to the values reported earlier (Malerba et al., 2014; Henry et al., 2017).

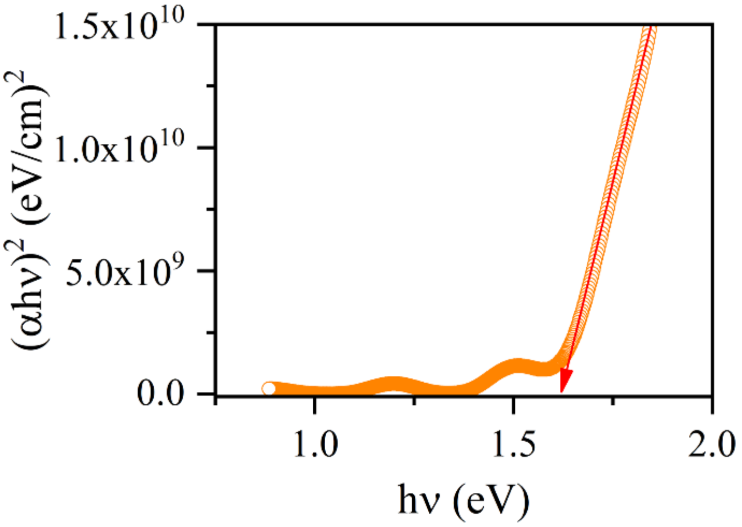

Fig. 5.4: Tauc's plot for the band gap calculation of the phase pure CZTS film grown at T_s = 450 °C

5.4 Photosensitivity of the films

The photo-response behavior of the films grown at various substrate temperatures is shown in Fig. 5.5. The photosensitivity *S* was evaluated from *S* = (I_{light} – I_{dark}) / I_{dark}, where I_{dark} and I_{light} are the dark current and current in illumination condition, respectively. The value of sulfur were found to be ~ 0.6, 210 and 0.1 for the films deposited at 400, 450 and 500 °C, respectively at a bias voltage of 5 V. The poor performance of the films grown at 400 and 500 ºC is due to prompt recombination of electron-hole pairs generated due to light illumination, which may be most likely due to the presence of secondary phases and poor surface microstructure of the grown films (Mitzi et al., 2011; Sun et al., 2016). On the other hand, the films grown at 450 °C exhibited a higher photosensitivity. The significant increase in current after light illumination is attributed to the generation of free carriers because of absorption of incident photons. The increase in the holes in the presence of light enhanced the conductivity of the CZTS films (Henry et al., 2017). The obtained result is similar to the previously reported ones (Henry et al., 2017; Mitzi et al., 2011; Sun at al., 2016).

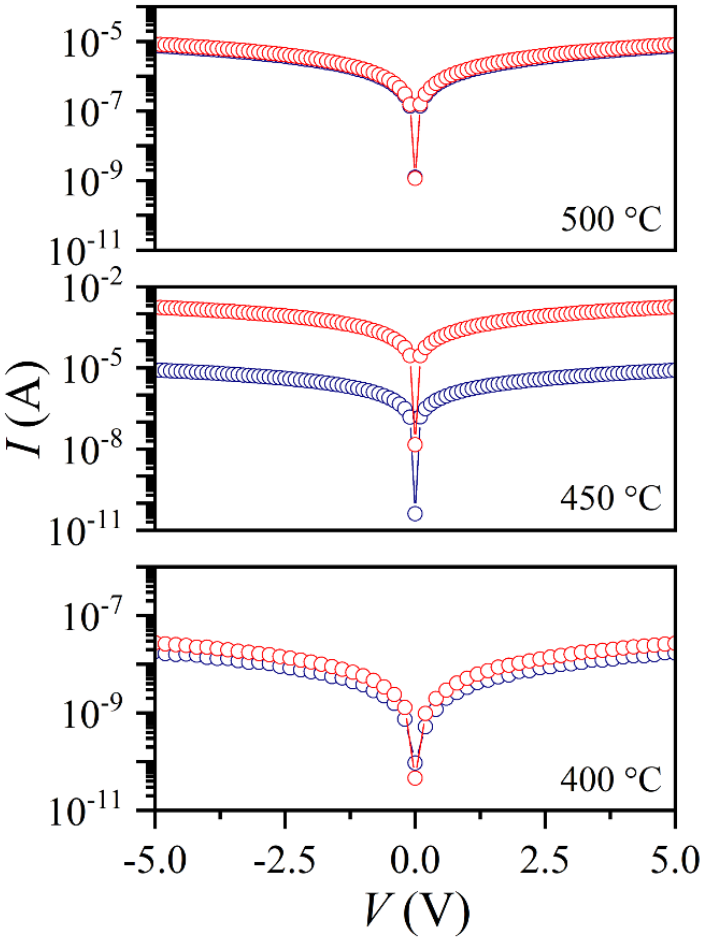

Fig. 5.5: Semi-log I-V characteristics under dark and illumination (AM 1.5, 100 mW/cm^2) conditions of the films grown at different substrate temperatures. The blue and red symbols corresponds to the dark and white light illumination conditions.

5.5 Performance of a Mo/p-CZTS/Ag device

A device in the form of Mo/CZTS/Ag structure using the phase pure CZTS films (i.e., the one grown at 450 ºC) which was prepared on glass substrate. Fig. 5.6a presents a typical XRD pattern of CZTS thin film on the Mo coated glass substrate. This is similar to the pattern obtained for the films grown directly on the glass substrates (Fig. 5.2a) other than the two Mo peaks, suggesting growth of phase pure CZTS. Figure 5.6b shows the corresponding cross-section SEM image of the CZTS film grown on Mo/Glass.

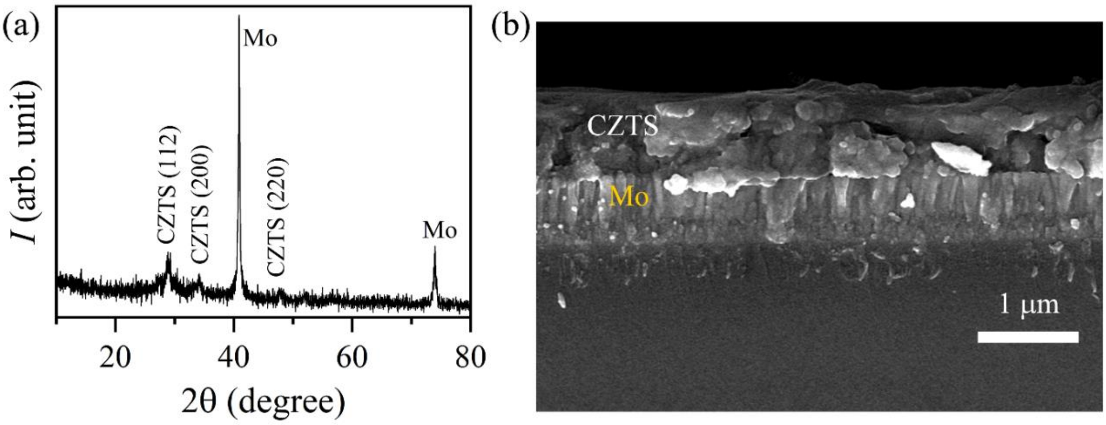

Fig. 5.6: (a) Typical XRD pattern and (b) cross-sectional SEM image of the CZTS film grown on Mo coated glass substrate at T_s=450 °C.

Figure 5.7 shows a typical dark I-V curve of the device. It shows large current in the first quadrant while the current remained very low in the fourth quadrant. The observed rectifying behaviour is because of the formation of a Schottky contact between CZTS and Ag arising due to the difference in the Fermi level of CZTS (E_F = 4.5 eV) and the work function of Ag (Φ_{Ag} = 4.26 eV) (Boutebakh et al., 2017).

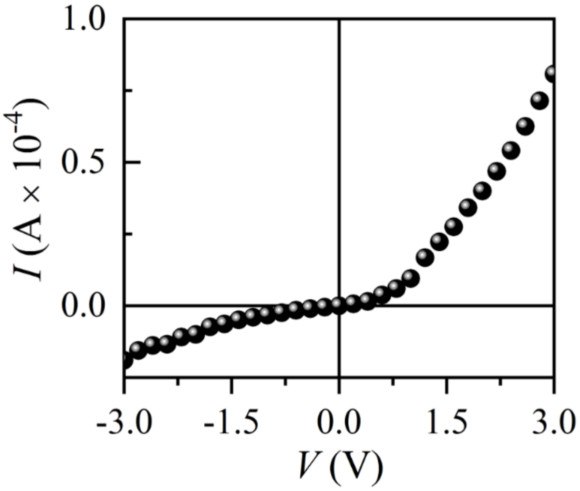

Fig. 5.7: Current-voltage characteristics plot of Mo/CZTS/Ag based Schottky junction at room temperature under dark conditions of the films grown at T_S = 450 ºC.

The obtained I-V curve was used to determine the diode parameters. The dark shunt conductance G (Hegedus et al., 2004) was calculated to be 3.7×10^{-3} mS from the dI/dV vs V plot as shown in Fig. 5.8. It may be noted that a dark shunt conductance < 1 mS is highly desirable for efficient solar cells (Hegedus et al., 2004).

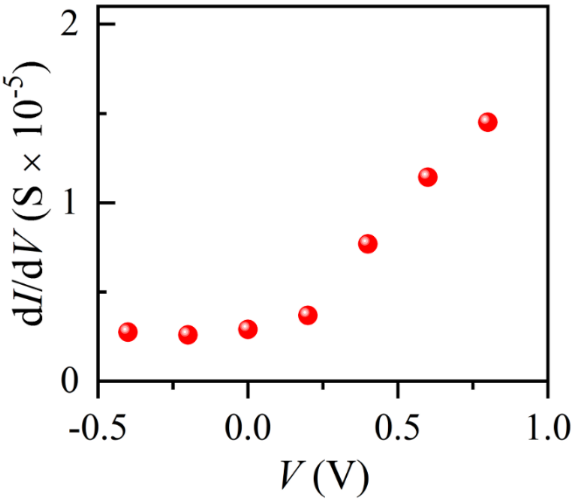

Fig. 5.8: Shunt characterization plot of dI/dV vs applied voltage (V) of Mo/CZTS/Ag based Schottky junction at room temperature under dark conditions of the films grown at T_S = 450 °C.

In order to estimate the value of series resistance, we have plotted the bias dependent resistance dV/dI vs V (Fig. 5.9) (Pür et al., 2012). It is observed that the dynamic resistance of the diode changes with the applied voltage. However, at a higher voltage, the value of dV/dI remained nearly independent of the voltage, which represents the value of series resistance R_S (~3.8 kΩ).

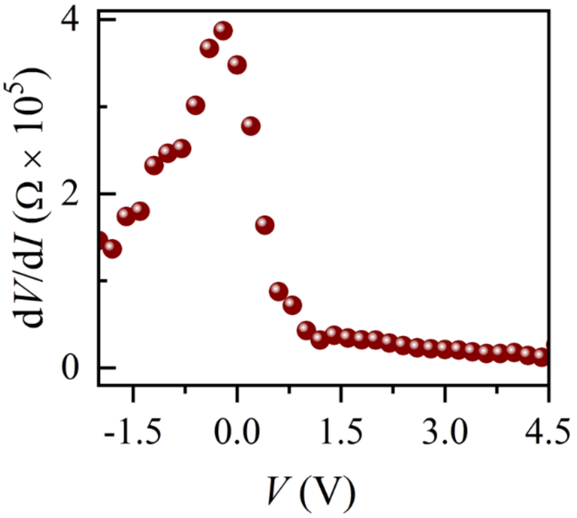

Fig. 5.9: Bias dependent resistance dV/dI vs applied voltage (V) plot of Mo/CZTS/Ag based Schottky junction at room temperature under dark conditions of the films grown at T_S = 450 °C.

Furthermore, the I-V characteristics of the Mo/CZTS/Ag device was analysed using the conventional thermionic emission theory, mentioned in Eq. 2 [Sze et al., 2021]

$$I \approx I_s \exp\left(\frac{q(V-R_s I)}{\eta kT}\right) \qquad (2)$$

where I_s is the saturation current, η is the ideality factor, k is the Boltzmann constant, T is the absolute temperature and R_s is the series resistance. For small current region in forward bias, the current is order of the saturation current, and hence the product $R_s I$ becomes negligible. Therefore, the value of I_s can be calculated by extrapolating the linear region of the forward bias semi log *I-V* curves to the zero applied voltage (i.e V = 0) (shown in Fig. 5.10), which yields I_s = 0.32 µA. The slope of the linear region of this curve provides an estimate of $q/\eta kT$. The value of η at room temperature was determined to be 8.5. Such a high value of the ideality factor against the expected value of 1 is similar to the ones often reported in literature and is attributed to the presence of pin holes and cracks formed on the film surface, which cause low shunt resistance in the diode resulting in a leakage current (Yiğit Gezgin et al., 2019; Servaites et al., 2011; Liao et al., 2018). Another possible reason of large ideality factor may be the poor Ohmic metal/CZTS contact. When the contact is not Ohmic, the junction can be modelled as a series of diodes and resistor (Shah et al., 2003), and the ideality factor is the sum of the ideality factors of all diodes. Boutebakh et al. gave the same possible reason for the measured ideality factor of 10.5 for the CZTS/Ag device (Boutebakh et al., 2017). Jing- Jing et al. have also explained the calculated 18.8 ideality factor for the ZnO:Al/(p)Si heterojunction (Jing-Jing et al., 2010).

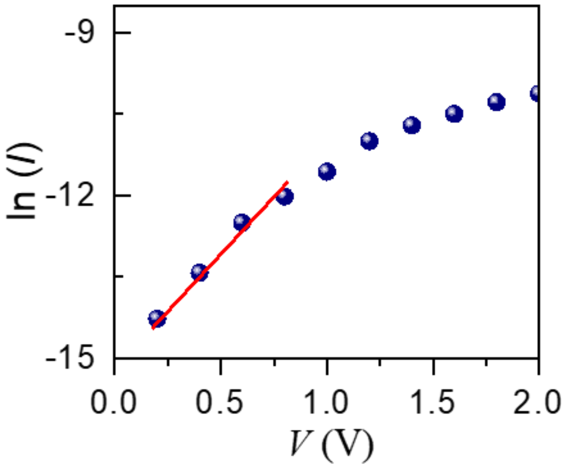

Fig. 5.10: Logarithm of current ln(I) vs the forward bias voltage (V) plot of Mo/CZTS/Ag based Schottky junction at room temperature under dark conditions of the films grown at T_S = 450 ºC.

5.6 Impedance spectroscopy of the phase pure CZTS film

Electrochemical-Impedance spectroscopy (EIS) and Mott-Schottky (MS) measurements were carried out by a standard three electrode configuration where Pt wire and Ag/AgCl in saturated KCl (0.197 V vs normal hydrogen electrode, NHE) were used as counter and reference electrode, respectively. The phase pure CZTS thin films (i.e the one grown at 450 °C) on Mo-coated glass slides were used as a working electrode. The preparation of the Mo thin films has been detailed in Chapter 2. The surface area of the working electrode dipped in the electrolyte was ~0.63 cm^2. A neutral solution of 0.1 M Na_2SO_4 with 7.2 pH was used as electrolyte. The EIS measurement was performed under potentiostatic condition in the frequency range of 5 MHz to 1 Hz and using a 10 mV sinusoidal potential. The impedance parameters were obtained by fitting the measured data by Z-fit using EC Lab software (Bio-Logic). The MS measurement was taken at 10 kHz frequency at applied potential of -1 to +1 V with 10 mV AC amplitude. The applied potential (V vs. Ag/AgCl) values were converted into reversible hydrogen electrode (RHE) scale for an easy comparison to hydrogen evolution by using the following equation: (Guan et al., 2014)

$$E_{RHE} = E_{Ag/AgCl} + 0.059\ pH + E^0_{Ag/AgCl} \ldots\ldots\ldots.\ (3)$$

Where $E^0_{Ag/AgCl}$ = 0.197 V at room temperature and $E_{Ag/AgCl}$ is experimentally observed value. All measurements were carried out in the dark.

Figures 5.11a and b show the frequency dependence of real and imaginary part of calculated capacitance. The inset to Fig. 5.12a shows the measurement configuration. The real and imaginary part of capacitance were calculated using the following relations (Taberna et al., 2003)

$$C'(\omega) = \frac{-Z''(\omega)}{w|Z(\omega)|^2} \qquad (4)$$

$$C''(\omega) = \frac{Z'(\omega)}{w|Z(\omega)|^2} \qquad (5)$$

where Z’ and Z” are the real and imaginary part of measured impedance, respectively, ω is a angular frequency and $|Z|$ is the magnitude of the impedance spectrum. The observed behaviour of the CZTS film electrode is similar to the ones reported by others (Patil et al., 2016).

Figure 5.11c shows the Nyquist analysis plot of the sample in the frequency range of 1 Hz to 5 MHz. The symbols denote the experimental data whereas the solid line indicates the fitting using a circuit model as shown in inset to Fig. 5.11c. As noted from the figure, the modelling yielded an excellent fit to the data points. The plot consists of a semicircle in the high frequency region (5 MHz to 10 kHz) and a straight line in the lower frequency range (up to 1 Hz). The arc in the high frequency regime occurred due capacitance of space charge region (C_2) along with its resistance component (R_2). These components arise due to the contact of semiconductor and electrolyte (Ge et al., 2017). The linear component at low frequency region reveals the ionic diffusion in the electrolyte occurring in the nearby of the semiconductor-electrolyte interface, which is typically modelled by a Warburg elements (W_3) (Patil et al., 2016; Ge et al., 2017; Lopes et al., 2010). Our modelling yielded values of R_1, R_2 and C_2 to be 26.32 Ω, 230.4 Ω and 0.63 nF, respectively.

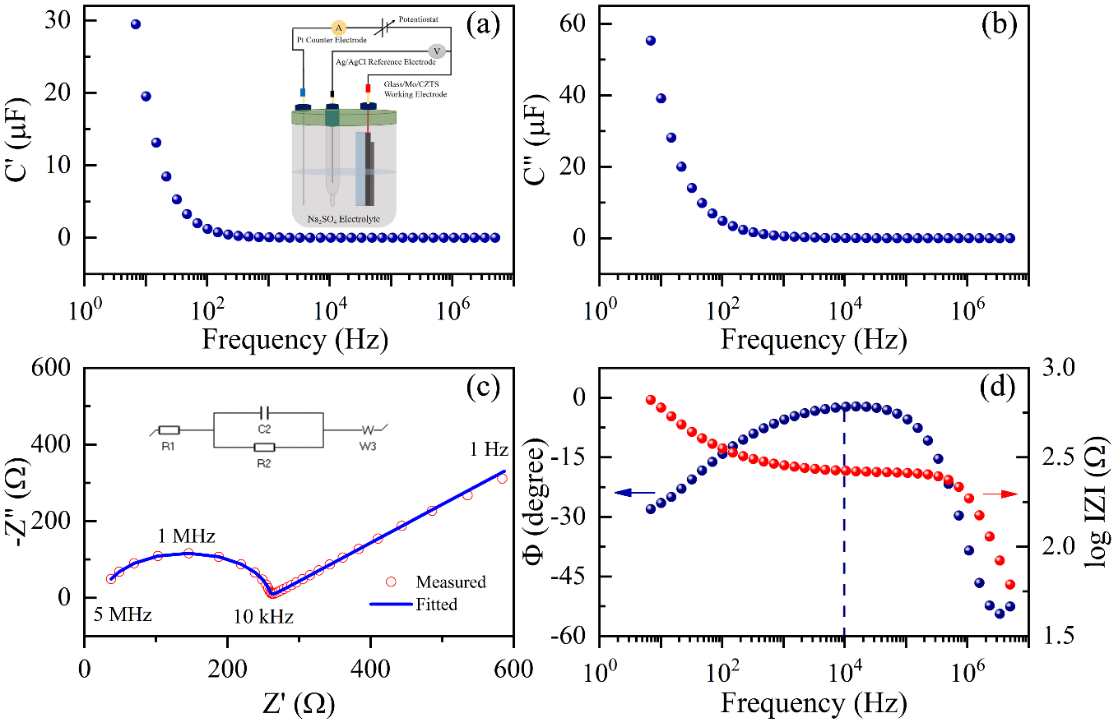

Fig. 5.11: Calculated frequency dependent (a) real and (b) imaginary part of capacitance, (c) measured and fitted nyquist plot in the frequency range from 5 MHz to 1 Hz using a 10 mV sinusoidal potential. The fitting data was obtained from the measured data by Z-fit using EC Lab software (red circular symbol) and (d) Bode phase plot of phase pure CZTS film grown at 450 °C substrate temperature: 0.1M Na_2SO_4 with pH=7.2. The measurement configuration and fitted circuit are presented in inset of (a) and (c), respectively.

Figure 5.11d shows Bode plot associated with the CZTS electrode. The Bode plot provides the information of the electron life time inside the electrode-electrolyte transition (Patil et al., 2016; Demir et al., 2021). The observed negative phase angle suggests a superior electrochemical behaviour (Swami et al., 2014). The resistance of the CZTS electrode sharply dropped at higher frequencies, characterized by a distinct change in the slope (Patil et al., 2016). The carrier lifetime τ_r in an electrode is determined by using the following formula, (Swami et al., 2014; Hauff et al., 2019)

$$\tau_r = \frac{1}{2\pi f_{max}} \qquad (6)$$

In the present case, the f_{max} of CZTS film is estimated to be ~10^4 Hz yielding a carrier lifetime of ~17.5 μs, which is comparable to the reported value for CZTS films (Khanra et al., 2018). The carrier lifetime is correlated to the carrier recombination rate, i.e., higher is the lifetime, lower will be the carrier recombination loss. Consequently, more number of electrons can be transferred to the electrolyte to produce H_2, for example in water splitting applications (Swami et al., 2014).

5.7 Mott-Schottky analysis of the phase pure CZTS film

The capacitance – voltage measurement was carried out at 20 kHz under an applied DC bias voltage (vs RHE) and is shown in Fig. 5.12a. The capacitance decreases exponentially upon reverse bias voltage from a fix polarization potential. The trend shows that the bias voltage can enlarge the depletion region and shrink the capacitance of the cell as given below (Sze et al., 2021)

$$W_d = \frac{A\varepsilon_0\, \varepsilon_S}{C_S} \qquad (7)$$

$$N_{C-V} = \frac{C^3}{q\varepsilon_0\, \varepsilon_S A^2 \left(\frac{dC_S}{dV}\right)} \qquad (8)$$

where C_S, A, ε_0, ε_s and q stand respectively for capacitance of space charge region (F/cm^2), area of working electrode dipped in the electrolyte, dielectric constant of vacuum (8.854×10^{-12} F/m), dielectric constant of CZTS (~7.0) and electronic charge. Figure 5.12b shows the profiling of space charge density (N_{C-V}) derived from the C-V curve (Eq. 7 and 8). The values of W_d and the corresponding space charge density were estimated to be ~0.17 µm and ~10^{17} cm^{-3}, respectively. It may be noted that the photocurrent depends upon the depletion width. Higher the depletion width, more effective will be the separation of charge carriers; but would result in high resistivity (Wang et al., 2014).

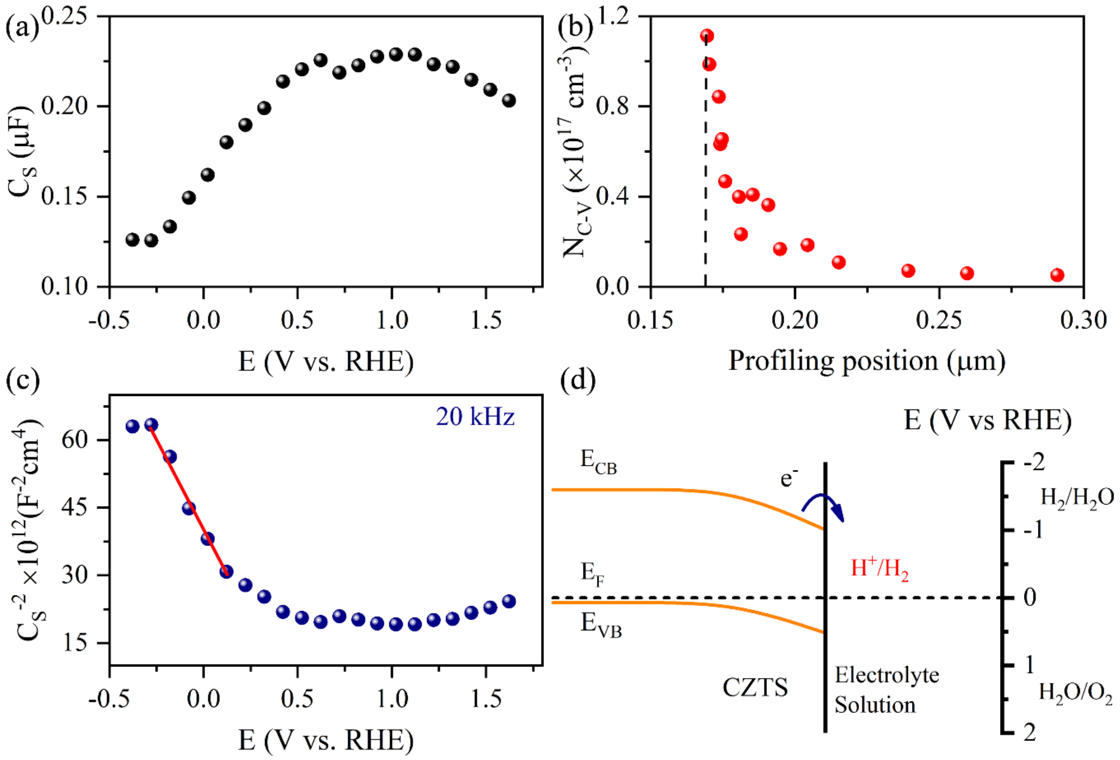

Fig. 5.12: (a) Frequency dependent capacitance versus voltage plot, (b) profiling position (or depletion width) and space charge density derived from capacitance versus voltage curve, (c) frequency dependent Mott-Schottky plot carried out at 20 kHz under applied DC bias voltage and (d) energy band position with respect to water redox potential determined by Mott-Schottky analysis of phase pure CZTS film grown at 450 °C: 0.1M Na_2SO_4 with pH = 7.2.

On the other hand, Mott-Schottky (MS) measurement provides more information about the semiconducting properties of CZTS in contact with the electrolyte. In particular, the conduction type and the flat band potential (V_{FB}) were estimated by applying the Boltzmann statistics to obtain the MS equation [Sze et al., 2021]

$$\frac{1}{{C_S}^2} = \frac{-2}{q\varepsilon_0\, \varepsilon_s N_A A^2}\left(V - V_{FB} + \frac{kT}{q}\right) \tag{9}$$

$$E_{VB} = V_{FB} + \frac{kT}{q}\ln\left(\frac{N_V}{N_A}\right) \tag{10}$$

where C_S, A, ε_0, ε_s, q, N_A, V, V_{FB}, k, T, N_V and E_{VB} stand respectively for the capacitance of space charge region (F/cm^2), area of working electrode dipped in the electrolyte, dielectric constant of vacuum (8.854×10^{-12} F/m), dielectric constant of CZTS, electronic charge, acceptor density, applied potential (vs RHE), flat band potential, Boltzmann constant, temperature (300 K), effective density of states (~10^{19} cm^{-3}) at the valance band edge [Joshi et al., 2012] and valance band position. Figure 5.12c shows the measured MS graph derived from capacitance – voltage profile at 20 kHz to avoid the Warburg and Helmholtz capacitance at low frequencies

(Ge et al., 2017) while estimating the flat band potential and carrier density. As noted from the figure, the MS curve of the CZTS film showed a negative slope that indicates p-type conductivity (Yoshida et al., 2018). The acceptor concentration (N_A) is found as ~6.2×10^{17} cm^{-3} from the slope of the MS plot using Eq. (9). This result is similar to those of Huang et al., who have prepared CZTS thin films by ultrasonic spray pyrolysis techniques followed by sulfurization and have estimated N_A to be order of ~10^{18} cm^{-3} from the EIS measurement (Huang et al., 2013). The flat band potential (V_{FB}) of 0.51 V (vs RHE) was determined by using Eq. (9). Our results are very close to the values reported earlier (Patil et al., 2016; Scragg et al., 2008). Thus, the valance band position (E_{VB}) is determined to be 0.58 V (vs RHE) by Eq. (10). Considering that the band gap of the phase pure CZTS films to be ~1.6 eV, as obtained from the Tauc's plot (Fig. 5.4), the conduction band position was determined to be -1.02 V (vs RHE). Figure 5.12d summarizes the band edge position diagram of the CZTS thin film based on the MS analysis. From an estimation, the fermi level position is 0.072 eV above the valance band maxima of CZTS, which suggests that the E_{CV} is -1.02 V than the hydrogen evolution potential. The obtained results indicate the developed p-type CZTS to work as a potential photocathode for hydrogen evolution (Ge et al., 2017).

In summary, we have prepared CZTS thin films in a single process step by RF magnetron sputtering. The process did not require any post-deposition sulfurization. A nominally high substrate temperature of 450 °C facilitated reaction in the depositing species that yielded single phase CZTS as confirmed by XRD and Raman analyses. The films had an optical band gap of ~1.6 eV, highly suitable for photovoltaic and photocatalytic activities. The resultant films exhibited high white light sensitivity (>200% at a bias potential of 5 V). Electrochemical analysis of the device with structure of Mo/CZTS/Pt/Electrolyte revealed p-type conductivity with flat band potential and carrier concentration of 0.51 V (RHE) and 6.2×10^{17} cm^{-3}, respectively.

CHAPTER 6

SELENIZATION OF THE CZTS FILMS GROWN BY SINGLE STEP PROCESSING FROM A TARGET WITH EXCESS Cu

As discussed in the Introduction Section (Chapter 1), the incorporation of selenium in the CZTS system significantly modifies the bandgap, improves the grain size and the quality of absorber layer. Consequently, the series resistance as well as open circuit voltage (V_{OC}) deficit is reduced, which help to improve the performance of the solar cells (Wei et al. 2019). However, selenization requires post-deposition heat treatment of the samples, which must not decompose the existing CZTS phase. Furthermore, the formation of secondary phases like Zn(S,Se) and $Cu_2Sn(S,Se)_3$ should be prevented because those negatively affect the efficiency of CZTSSe-based solar cells (Wei. et al., 2019; Minbashi et al., 2020). Thus, the process parameters must be delicately controlled so that the CZTS does not decompose into binary/ternary secondary phases (Sun et al., 2018). In this chapter, the CZTS films that were grown in a single step (chapter 5) were selenized and the influencing mechanism of various parameters have been presented. Selenium ingots as source

elenium during the selenization process was used instead of the conventional toxic H_2Se gas, which makes this process environmental friendly.

6.1 Evolution of phase

Figure 6.1a shows the photograph of the phase pure CZTS film (i.e., the one grown at a substrate temperature of 450 °C by RF magnetron sputtering of a target with 12.5% excess Cu) on Mo coated glass slides. For selenization at 500 °C for 60 min with 1.0 g of selenium ingots, the film was completely removed. A dull whitish residue was left on glass substrates (Fig. 6.1b). Although we have not explicitly probed, the dull whitish residue might be due to the formation of a thick MoS_x layer and pealing of the selenide overlayer as a consequence of a large volume expansion. It may be noted that these were the parameters (i.e., time, temperature and amount) earlier used to prepare the phase pure CZTS thin films (chapter 4). The obtained result was contrasting to the results obtained by (Wei et al. 2019). They have reported that the longer duration and high selenium vapor pressure at 500 °C is advantageous for large grain growth (Wei et al., 2019). In order to clarify whether the obtained poor results were due to a prolonged selenization duration, films were prepared at similar condition, but only for 10 min. However, the quality of the films was far from satisfactory, as shown in Fig. 6.1c. The film peeled off at random places leaving a discontinuous patch on the glass slides.

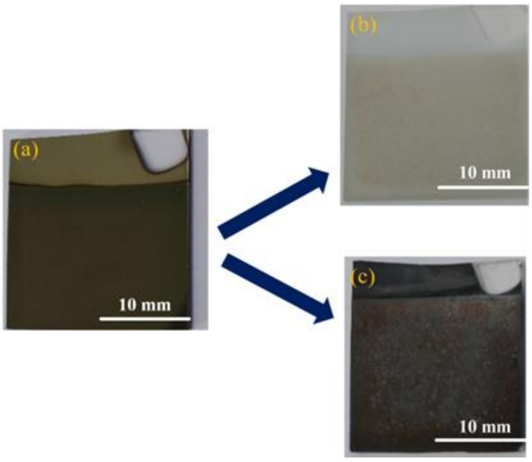

Fig. 6.1: Actual photographs of (a) CZTS film on Mo/glass; the glass/Mo/CZTS film selenized at 500 °C for (b) 60 min and (c) 10 min.

Further experiments were carried out to improve the quality of the films by selenizing at a lower temperature (i.e., 450 °C). The dwell time and the amount of selenium ingot were varied. Figure 6.2a shows the typical XRD pattern of the films selenized at 450 °C for different duration with 1.0 g of selenium. For easy comparison, the pure sulfide film (CZTS without selenization) is also presented. For the film selenized for 60 min, in addition to the two peaks of Mo, multiple peaks were observed at 23.76°, 25.25°, 26.70°, 30.25°, 31.72°, 37.76° and 48.20° (Fig. 6.2a). All the peaks correspond to the Cu_4SnS_4 (JCPDS file: 27-196) phase. It appears that longer duration led to the dissociation of the CZTS phase and did not assist in the formation of CZTSSe phase. In order to ascertain whether a shorter dwell time would result in the growth of phase pure films, selenization for 15 and 10 minutes was carried out. However, in all cases the presence of secondary phases was detected in the corresponding XRD patterns.

Lin et al. have suggested that the Se amount played critical role in the evolution of CZTSSe phase and grain growth (Lin et al., 2017). They found that high Se amount could lead to formation of secondary phase along with voids in the films. Therefore, selenization at 450 °C for 10 min with only 0.25 g of selenium was carried out. The comparison of the XRD patterns is shown in Fig. 6.2b. The XRD pattern of the film shows reflections at 26.55, 27.43, 33.83, 45.37, 46.52, 51.08 and 54.01° (Fig. 6.2b). The peaks at 26.55, 33.38 and 51.08° belong to Cu_4SnS_4 (JCPDS file: 27-196) respectively. However, the peaks at 27.43, 46.52 and 54.01° attributed to the CZTSSe phase.

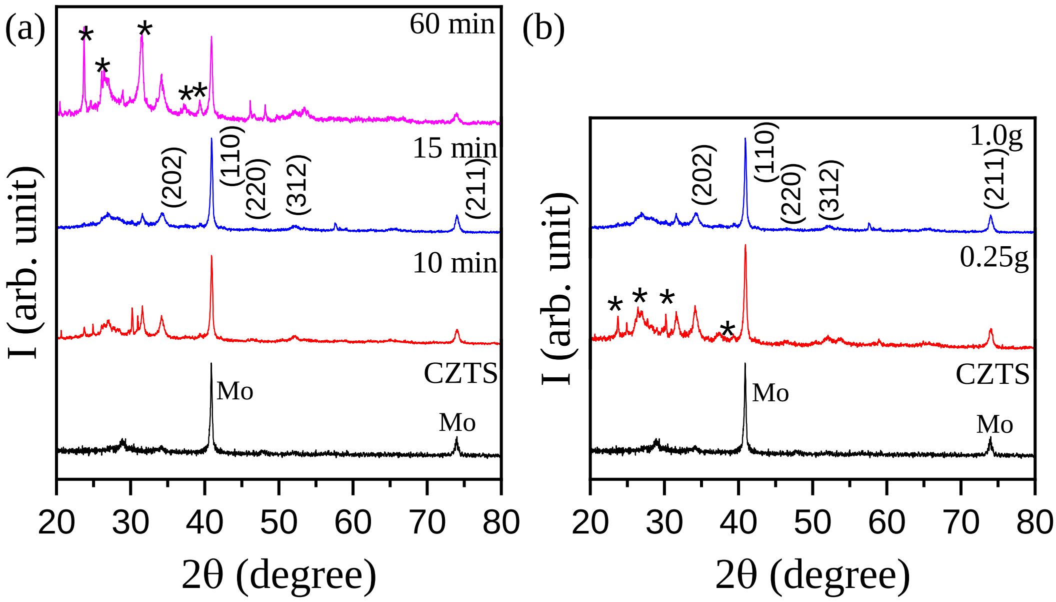

Fig. 6.2: Typical XRD patterns of the films selenized at 450 °C (a) for different durations with 1.0 g of selenium, and (b) for 15 mins with different amounts of selenium. In both panels, the pattern for the CZTS film without selenization is given for easy comparison. The asterisk (*) shows secondary phases (Please refer to text for details)

Many reports have suggested that heating rate can also influence the phase evolution of CZTSSe and associated spurious phases. For example, Chernomordik et al. have reported that fast ramp rate can help in the phase and microstructural evolution of CZTSSe nanocrystal during selenization (Chernomordik et al., 2016). Hence, in contrast to a normal heating (rate of 8 °C/min) as employed above, a fast heating rate was used for the further studies. In such cases, the glass/Mo/CZTS film placed over selenium ingots taken in a silica crucible was introduced to the heating zone in a tube furnace. It is expected that such a setup would allow the reaction in the presence of selenium vapor. Since selenization at 450 °C for durations ranging from 10-60 mins yielded secondary phases, further films were selenized at a marginally higher temperature (i.e., at 500 °C) with a higher ramp rate as mentioned above and for shorter duration (i.e., 5 mins). Fig. 6.3a-b show the XRD patterns of the films selenized at 500 °C for 5 min with different selenium amounts ranging from 0.25 to 0.75 g. The XRD pattern of the pure sulfide film was also added for easy comparison with the selenized films. For the films selenized with 0.25 and 0.5 g of selenium multiple peaks were obtained, which were identified with CZTSSe and Mo-related phases. The peaks at 27.82 and 46.5° are attributed to the (112) and (220) plane of CZTSSe phase (Sun et al. 2018). A small peak at 34.02° matched well with the Mo(S,Se)$_2$ phase (Wang et al., 2017). Two additional peaks at Bragg's position 40.90 and 74.16° belongs Mo (JCPDS file: 3-065-7442). It suggests the formation of phase pure films for selenization of the CZTS films with 0.25 and 0.5 g of selenium at 450 °C for 5 mins. The exact impact of selenization of different durations was understood from the shifting of the peaks in the XRD patterns. Figure 6.3b shows zoomed up region nearer to the (112) peak position. When the sulfur atoms are partially replaced by selenium atoms in the lattice, the Bragg peak is expected to shift towards lower 2θ values due to larger size of selenium. The shifting of the peak in the samples selenized with 0.25 and 0.5 g of selenium towards lower 2θ values confirm the inclusion of selenium in the CZTS. However, for the sample selenized with 0.75 g of selenium multiple secondary phases peaks appeared, which suggest that an optimum amount of selenium is required for growth of single phase CZTSSe thin films on Mo coated glass substrates.

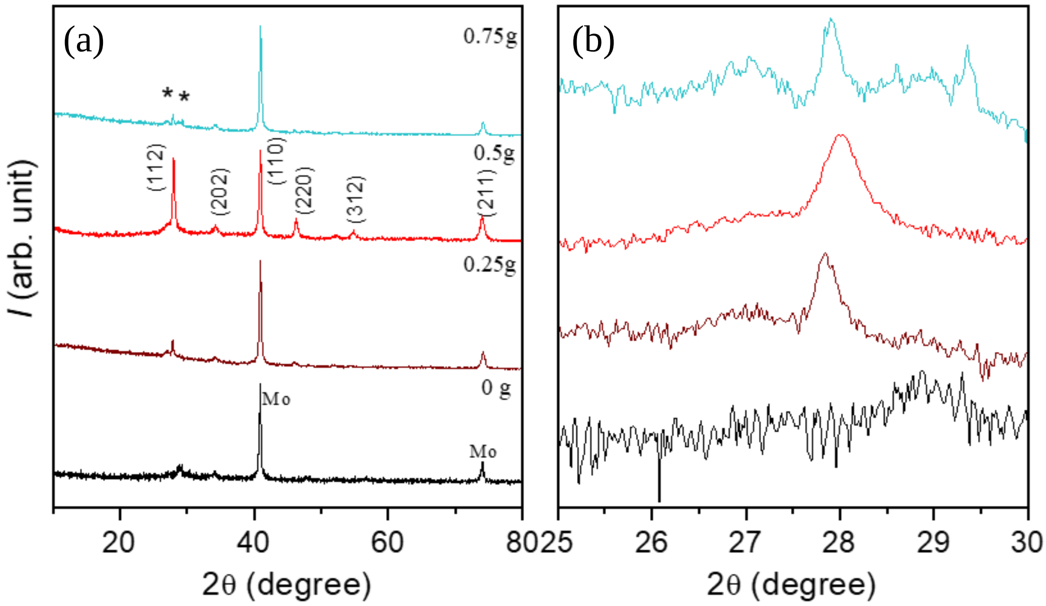

Fig. 6.3: Typical XRD patterns of the (a) pure sulfide and the film selenized at 500 °C for 5 min with different amounts of selenium and (b) zoomed up region near to the highest intensity peak of CZTS. In both panels, the pattern for the CZTS film without selenization (denoted as 0 g) is given for easy comparison. The asterisk (*) shows secondary phases (Please refer to text for details)

The CZTSSe and the associated secondary phases like ZnSe, SnSe, Cu$_2$Sn(S,Se)$_3$ have XRD peaks at similar 2θ values. Thus, additionally Raman spectroscopy has been used to confirm the phase purity of the samples. Fig. 6.4 shows the Raman spectra of the CZTS film without selenization and the films selenized at 500 °C for 5 mins with 0.25 and 0.5 g of selenium. The vertical lines denote the most dominant Raman peaks (A_1 mode) of CZTS and CZTSSe. The peaks at 288 and 335 cm^{-1} belong to the A1 symmetry of CZTS phase (Fernandes et al., 2011). However, the peaks at 195, 241, 262 and 328 cm^{-1} for the sample selenized with 0.25 g of selenium and 203, 237 and 332 cm^{-1} for the sample selenized with 0.5 g of selenium correspond to the CZTSSe phase (Suryawanshi et al., 2017). It may be noted that there is a small peak at ~404 cm^{-1}, which may be due to MoS_x (Chen et al., 2015).

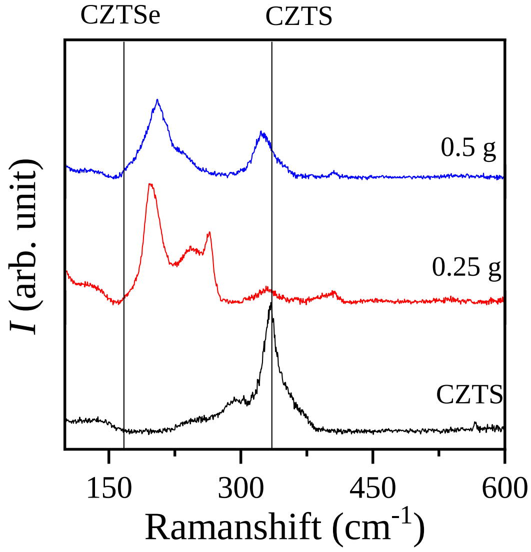

Fig. 6.4: Raman spectra of the pure sulfide films as well as the film selenized at 500 °C with 0.25 g Se for 5 min and 0.5 g Se for 5 min. The vertical lines denote the most dominant Raman peaks (A_1 mode) of CZTS and CZTSSe

Further, the films were selenized for longer duration at 500 °C with 0.5 g of selenium and the corresponding XRD patterns are given in Fig. 6.5a-b. As the selenization duration was increased to 10 min, a new peak was originated at 29.19° which correspond to Cu_4SnS_4 phase (JCPDS file: 00-029-0584), however, in the case of 15 min of selenization, multiple secondary phase peaks instigated. The new peaks at 13.06°, 15.45°, 20.26°, 22.68°, 23.15°, 24.85, 26.30° and 39.28° correspond to the secondary phases. The existence of multiple secondary phases with increasing the selenization time, justifies that high selenization time leads to evaporation of volatile elements at elevated temperature (Zhao et al., 2019). It may also be due decomposition of the CZTSSe phase, when the film selenized for the longer duration in the absence of selenium at elevated temperature for the long time (Sun et al., 218; Zhao et al., 2019).

It may be noted that high solar efficiency has been achieved for selenization with a longer dwell time, as reported in literature (Todorov et al., 2013, Wei et al., 2019, Minbshi et al., 2020). However, selenization configuration has been found to have a profound impact on quality of the films (Gupta et al., 2021). With a quasi-open configuration employed in this work, we found that dwell time of 10 and 20 mins resulted in growth of secondary phases, as evidenced by the XRD and Raman studies. Instead, we could grow films without any secondary phases for 5 min dwell time.

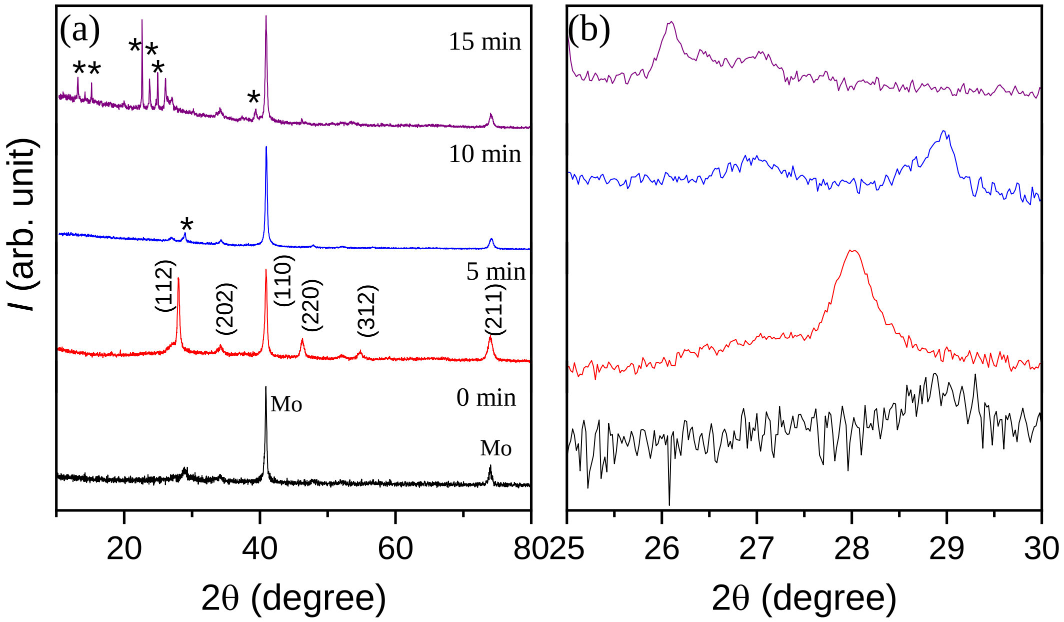

Fig. 6.5: Typical XRD patterns of the (a) pure sulfide and the films selenized at 500 °C with 0.5 g Se for different durations and (b) zoomed up region near to the highest intensity peak of CZTS. The asterisk (*) shows secondary phases (Please refer to text for details)

6.2 Microstructural features of the films

Figure 6.6 summarizes the surface microstructure of the films selenized at various conditions. Initially, for the pure sulfide film, the surface was uniform and densely packed with fine grains. However, the surface particulate size was greatly increased upon selenization. The size was around 450 nm for the film selenized with 0.25 g of selenium at 500 °C. Upon increasing the selenium amount, dissociation of particulates leading to an appearance of cracked surface is observed from the surface micrograph. On the other hand, agglomeration of smaller particulates was observed on the surface along with the voids when selenization time increased from 5 to 15 min. It might be due to volumetric contraction of the grains or the loss of volatile element when the film selenized for the longer time at elevated, caused by decomposition of the films leading to the formation of secondary phase, as evident from the XRD patterns.

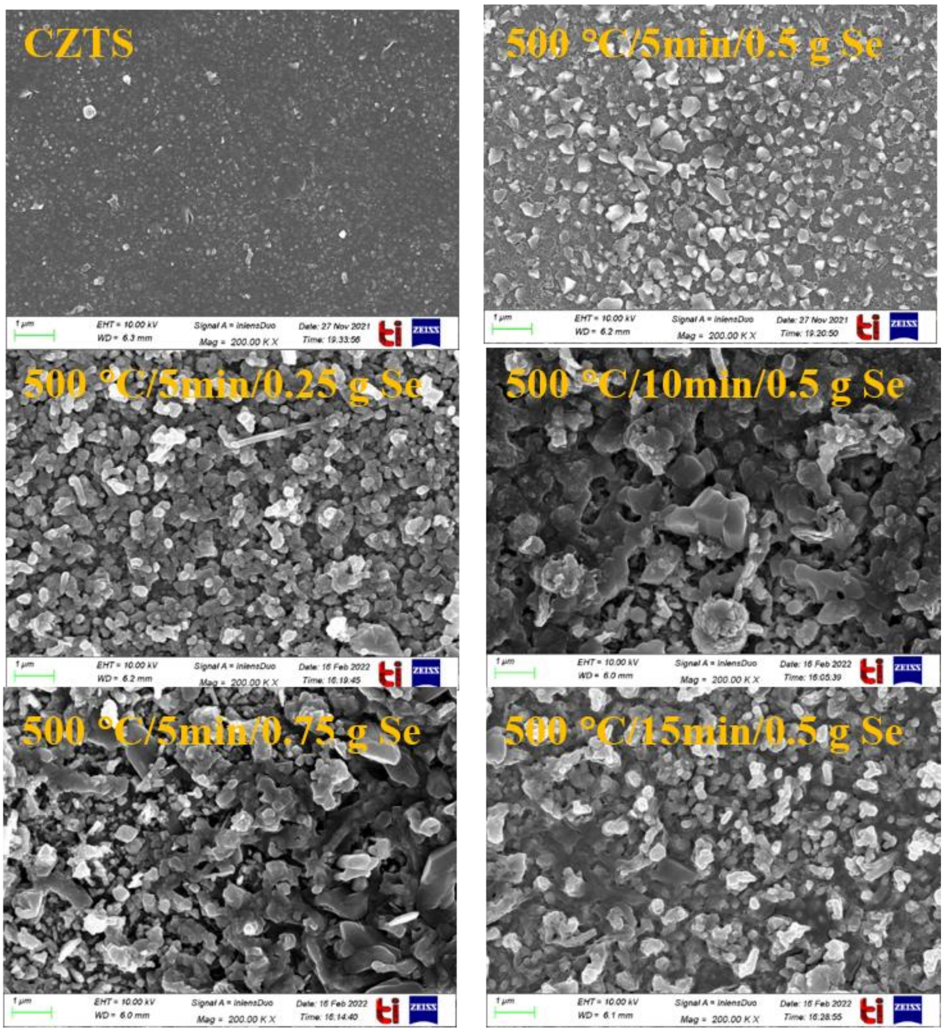

Fig. 6.6: Surface micrographs of the pure sulfide film and films selenized at 500 °C for 5 min with different Se amount and films selenized at 500 °C with 0.5 g Se different duration.

6.3 XPS analysis

Since the film selenized at 500 °C for 5 min with 0.25 g of selenium yielded single phase CZTSSe with reasonable good microstructure, XPS measurement was carried out on this sample. Figure 6.7 shows he core-level XPS spectra for Cu, Zn, Sn, S, and Se. The Cu 2p peaks are located at binding energies of 931.79 and 951.67 eV, with a peak separation value of 19.88 eV corresponding to a Cu^+ state (Suryawanshi. et al., 2014). The Zn 2p peaks appeared at binding energies of 1021.48 and 1044.68 eV, with a peak splitting value of 23.2 eV, which is consistent with the literature values reported for a Zn^{2+} state (Suryawanshi. et al., 2014). The valence state of Sn^{4+} was confirmed by the presence of binding energy peaks at 486.67 and 495.06 eV with a peak splitting value of 8.34 eV (Suryawanshi. et al., 2014). Four peaks of binding energies of 159.85, 161.13, 162.26, and 165.61 eV were observed in the S 2p spectrum (Cho et al., 2013). The peaks at 159.85, 161.13, 162.26, and 165.61 eV are attributed to the S 2p core, which is in accordance with the 160-165 eV range for S in a sulfide state, whereas the latter (165.8 eV) is ascribed to the Se 3p core. The Se 3d spectrum further confirms Se (II) by the presence of peaks at binding energies of 53.53 and 54.36 eV, which is consistent with the literature for Se in a selenide state (Ou et al.,2012). This outcome is well correlated with the XRD and Raman results.

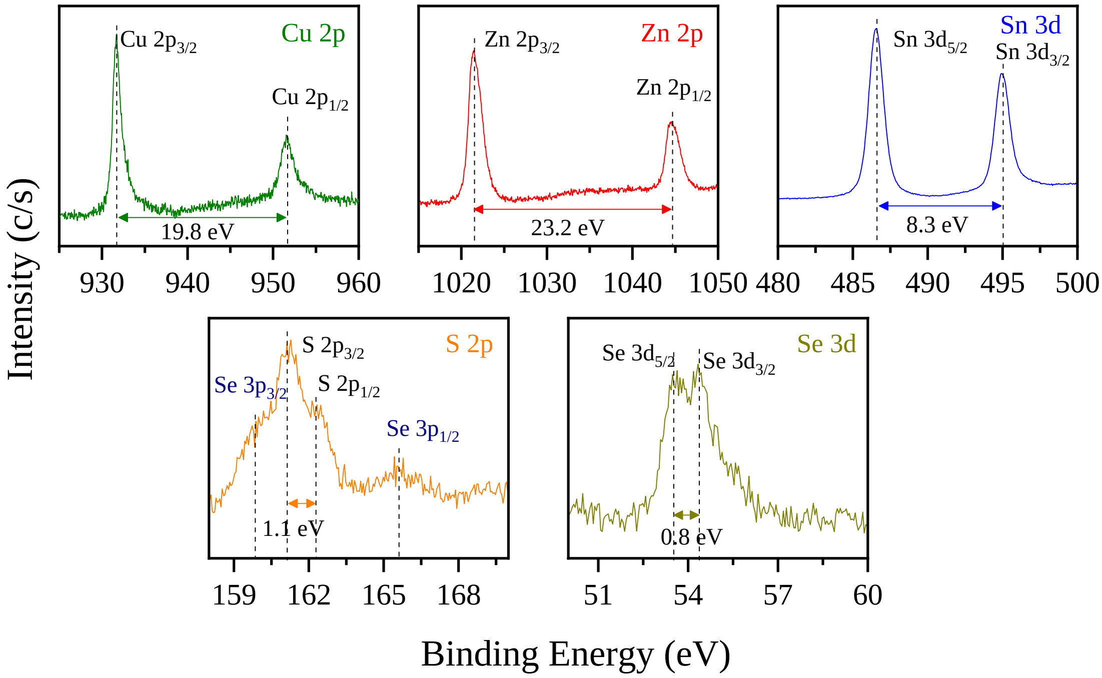

Fig. 6.7: Typical XPS spectra for core level Cu 2p, Zn 2p, Sn 3d, S 2p and Se 3d of the CZTSSe films selenized at 500 °C for 5 min with 0.25 g of selenium.

6.4 Optical properties of the film

The films were grown on Mo coated glass substrate. So, the bandgap of the films cannot be estimated through conventional transmittance and reflectance measurement. Therefore, diffuse reflectance was taken to determine the bandgap of the films. The $F(R_\infty)$ function was calculated from the measured diffuse reflectance of the films using Kubelka and Munk function (Kubelka et al., 1931): $F(R_\infty) = (1-R_\infty)^2/(2R_\infty)$ By replacing α from $F(R_\infty)$ in the tauc relation

($(F(R_\infty)h\nu)^2$ vs hν), bandgap of the films was determined. The deviation in the bandgap with selenium amount and selenization time is shown in Fig. 6.8a and b, respectively. The variation in the bandgap is expected to the inclusion of the selenium into the CZTS film (difference in the S/(S+Se)) (Singh et al., 2015). The bandgap of phase pure CZTSSe film (i.e., the one selenized with 0.25 g of selenium for 5 min at 500 °C) was ~1.18 eV. This value of bandgap for Se containing CZTS thin films is consistent with the earlier reports (Singh et al., 2015). As shown in Fig. 6.8a, the bandgap increased when the selenium amount was increased from 0.5 to 0.75 g during selenization. The increase in bandgap may be due to the presence of secondary phases, as evidenced from the corresponding XRD pattern (Fig. 6.3a). Similarly selenization for more than 5 mins yielded secondary phases (Fig. 6.5a) which resulted in an increase in bandgap (Fig. 6.8b).

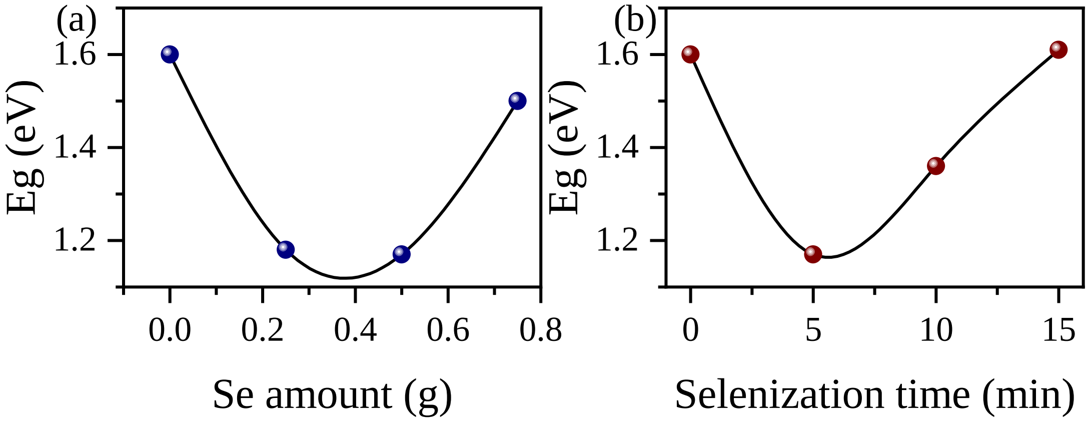

Fig. 6.8: Deviation in the optical band of the films selenized at (a) 500 °C for 5 min with 0.25-0.75 g Se and (b) 500 °C with 0.5 g Se for 5-15 min. For easy assessment band gap of pure sulfide film was also added.

6.5 Electrical properties of the films

Figure 6.9a-b shows the variation in electrical resistivity of the samples with selenium amount and selenization time. The resistivity, as discussed in Chapter 2, is measured using the van der Pauw method. The resistivity initially decreased with increasing selenium amount up to 0.5 g and then sharply increased thereafter. A similar trend was also noted for the variation in the selenium amount during the selenization process. The increased resistivity is due to the presence of the secondary phases at higher selenium amount (Figs. 6.3a) and at longer selenization duration (6.5a). Thus, as the fraction of secondary phases decreased in the samples, the overall resistivity of the sample decreased. For the phase-pure film, i.e., the one grown with

500 °C for 5 min using 0.25 g of selenium, resistivity was found to be 0.21 Ω-cm, which is similar to the values reported by several other groups (Mitzi et al., 2011).

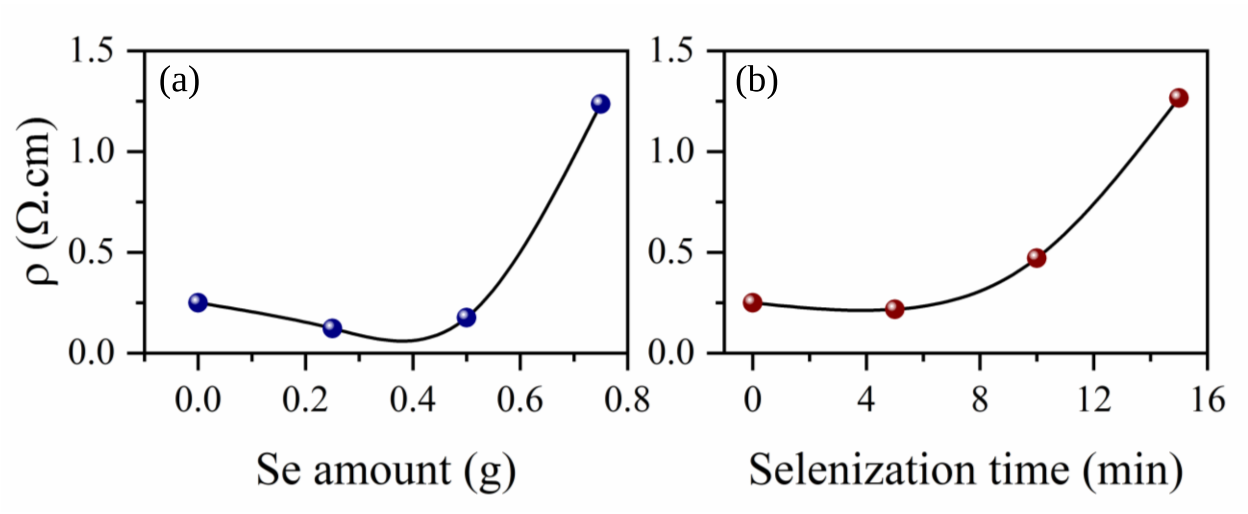

Fig. 6.9: Electrical resistivity of the films selenized at 500 °C (a) for 5 min with 0.25-75 g Se and (b) 0.5 g Se for 5-15 min. For the comparison, the result of pure sulfide film is also included.

6.6 Photosensitivity of the film

The photoresponse behavior of the phase-pure CZTSSe thin film (i.e., the film selenized at 500 °C for 5 min with 0.25 g of selenium) has been evaluated next. Figure 6.10 inset shows the device configuration used for the measurement of photoresponse behavior. The voltage - current characteristics of the film under dark and white light (AM 1.5G, 100 mW/cm^2) illumination are shown in Fig. 6.10. The sample showed significant improvement in current upon white light illumination. For example, at a bias voltage of 2 V, the current increased from 2.26 mA in dark to 10.0 mA in illumination. The photosensitivity was found to be 382% in illumination compared to dark. The obtained result is consistent with the earlier reports (Devi et al., 2019; Henry et al., 2020). Furthermore, for the CZTSSe/Ag junction, very high current in the first quadrant and negligible current in the third current indicate excellent rectifying behavior, typical of a Schottky junction.

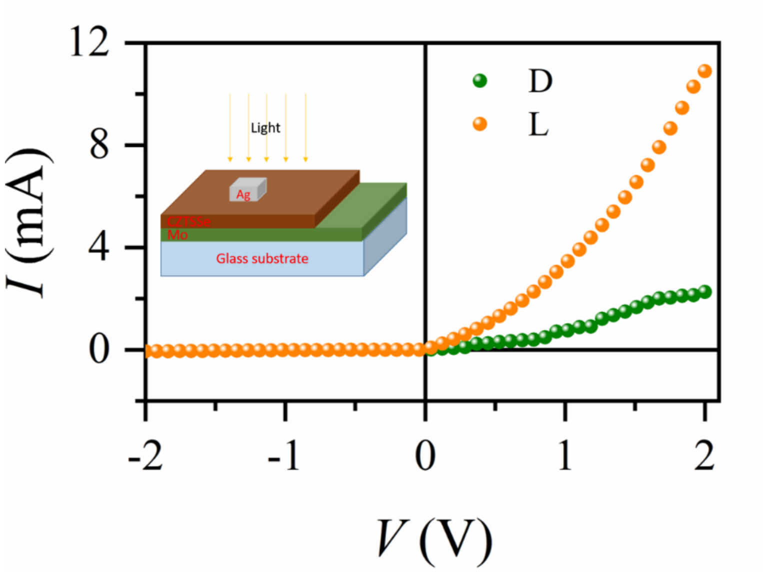

Fig. 6.10: Typical photo response behavior of the CZTSSe films selenized at 500 °C for 5 min with 0.25 g of selenium in dark and under white light illumination.

In summary, we have shown the growth of phase pure CZTSSe thin films by RF magnetron using a single elementary target followed by post-selenization. The effect of selenization temperature, dwell time and selenium amount on the phase evolution of the films has been studied. As confirmed from XRD and Raman measurements, phase pure CZTSSe is obtained for the film selenization at 500 °C for 5 min with 0.25 g Se with a fast heating profile. Electrical resistivity and the bandgap of the phase pure CZTS film were 0.21 Ω.cm and ~1.18 eV, respectively, which are similar to the reported value. I-V measurement of a device of Mo/CZTS/Ag configuration showed typical features of Schottky contact. The phase pure film shows the high photo sensitivity (~382%) upon illumination at 2 V bias.

CHAPTER 7

SUMMARY AND FUTURE SCOPE

The major conclusions of the thesis works are highlighted in this chapter. The work for the future investigation has been also proposed.

In the context of on-going research on thin film photovoltaics, CZTS has emerged as a very promising absorber material. This thesis deals with the growth and characterization of CZTSSe thin films synthesized by RF magnetron sputtering. Considering the narrow phase stability and low formation energy of the secondary phases in the Cu-Zn-Sn-S system, it is of high interest to design an appropriate deposition method to prepare single phase CZTS thin films. While conventionally sequential sputtering or co-sputtering approaches to prepare phase pure films have been used, delicate control on the deposition rate or thickness of the stacks has been required. In this work, a simple cost-competitive approach in the form of deposition from a single target using elemental powders has been demonstrated. It was shown that when a target with stoichiometric composition was used, the resulting films were always Cu-poor, leading to existence multiple secondary phases in spite of a large variation in the deposition and sulfurization parameters. The Cu deficiency was found to be due to its poor sputter yield compared to other elements. This problem was circumvented by growing an intermediate Cu layer sandwiched between two Cu-Zn-Sn-S layers. For a 195 nm thick Cu layer, phase pure CZTS films with appropriate optical and electrical properties were obtained.

Motivated by the above result, a sputter target was prepared that contained 12.5% of excess Cu. Films were prepared using this target and the post-deposition sulfurization parameters including dwell time, temperature and amount of sulfur were iteratively optimized. It was found that these parameters critically affected the evolution of phase and microstructure of the resultant films. Phase pure kesterite CZTS films were obtained by sulfurization at 500 °C for 60 min with 1.0 g of sulfur flakes in a quasi-open environment. Electrical resistivity and the bandgap of the phase pure CZTS film were 0.21 Ω.cm and ~1.58 eV, respectively, which are comparable to the reported values and are favorable for photovoltaic application. A Schottky junction in the form of p-CZTS/Ag junction on Mo coated glass substrates was fabricated and the I-V characteristics were investigated in detail.

Following the successes of preparation of the CZTS thin films by sputtering from an elementary target containing excess Cu followed by post-deposition sulfurization, an intuitive process to mitigate the challenges arising during the sulfurization process was designed.

Kesterite single phase CZTS thin films could be prepared in a single process step by RF magnetron sputtering that did not require any post-deposition sulfurization. A nominally high substrate temperature of 450 °C facilitated reaction in the depositing species that yielded single phase CZTS, as confirmed by XRD and Raman analyses. The films had an optical band gap of ~1.6 eV, highly suitable for photovoltaic and photocatalytic activities. The resultant films exhibited high white light sensitivity (>200% at a bias potential of 5 V). Electrochemical analysis of the device with structure of Mo/CZTS/Pt/Electrolyte revealed p-type conductivity with flat band potential and carrier concentration of 0.51 V (RHE) and 6.2×10^{17} cm^{-3}, respectively.

It was found that the post-deposition heat treatment ambience, especially the selenization process critically influenced the grain growth and properties of the eventual films. In view of that, the CZTS films that were grown in a single step (at 450 °C substrate heating) by RF magnetron using a single elementary target containing 12.5% excess Cu were subsequently selenized. The effect of selenization temperature, dwell time and selenium amount on the phase and microstructural evolution of the films has been studied. A detailed discussion on the influencing mechanism of the selenization processes has been presented. Phase pure CZTSSe is obtained for the film selenized at 500 °C for 5 min with 0.25 g Se with a fast heating profile. Electrical resistivity and the bandgap of the phase pure CZTS film were 0.21 Ω.cm and ~1.18 eV, respectively, which are similar to the reported values. I-V measurement of a device of Mo/CZTS/Ag configuration showed typical features of Schottky contact. The phase pure film shows the high photosensitivity (~382%) upon illumination at 2 V bias.

Although development of a simple approach to fabricate phase pure CZTS and CZTSSe thin films and understanding of the mechanisms of phase evolution have been the main motivations of this work, fabrication of solar cells based on the obtained absorber layers would be the natural extension of this thesis work. Solar cells in the conventional structure of glass/Mo/CZTS/CdS/i:ZnO/ ZnO:Al/Al can be fabricated and the quality of the absorber layers may be further optimized based on the obtained results. While analyzing the performance of the solar cells, the study of reactions at the interfaces and optoelectronic characterization of the layers could be of particular interest.

Appendix 1

Selected reports on efficiency of sputter deposited CZTSSe thin film solar cells

Material	**Synthesis method**	**Chalcogen and method**	**η (%)**	**Year [Ref]**
CZTS	Co-sputtering of ZnS, SnS, Cu	3 hrs at 580^{0}C with H_2S	5.74	Jimbo et al., 2007
CZTS	RF co-sputtering Cu, ZnS, SnS	H_2S (20%) + N_2 at 580^{0}C for 3hrs; treated with DI water	6.77	Katagari et al., 2008
CZTSe	Sequential sputtering of Cu, Zn, Sn	Se vapors at 500^{0}C for 30 min	3.2	Zoppi et al., 2009
CZTS	Reactive sputtering of Cu_2ZnSn target	H_2S plasma	1.35	Liu et al., 2010
CZTS	Sputtering of Cu/Zn Sn/Cu	30 min at 560^{0}C	4.59	Chalapathi et al., 2011
CZTS	Stacked deposition of ZnS (sputtering)/Cu (evaporation) /Sn (evaporation)	30 min in Se atmosphere	6.0	Grenet et al., 2012
CZTS	Reactive co-sputtering of Cu, Zn, Sn in 50% H_2S/Ar mixture	550^{0}C in a 10% H_2S/Ar mixture	3.37	Li et al., 2012
CZTSSe	Co-sputtering of $CuSe_2$, ZnS, SnS_2	At 580^{0}C in SnS+S_2 atmosphere	7.75	
CZTS	Cu, Zn, and Sn layers	100% H_2Se environment for 5 to 30 min duration from 450 to 520^{0}C	7.5	Brammertz et al., 2013
CZTS	Reactive pulsed dc magnetron co-sputtering from Cu/Sn	560-570^{0}C for 10 min in a graphite box with S in a furnace	7.9	Scragg et

	(65:35) alloy and pure Zn targets in H_2S atmosphere			al., 2013
CZTS	RF magnetron sputtering of single CZTS target	500^0C for 2 hrs, H_2S (5%) +N_2	4.40	Nakamura et al., 2014
CZTSSe	Stacked Cu-Zn-Sn-S (RF sputtering)	Se metals in a furnace at 590^0C for 20 min	8.06	Kim et al., 2014
CZTSe	RF sputtering of single elementary target	530^0C for 30 min in N_2 atm with Se pieces	4.16	Jo et al., 2015
CZTSe	RF magnetron co-sputtering of Cu, Zn, Sn target	Selenized at 350- 600^0C for 60 min in graphite box	7.1	Bodeux et al., 2015
		Annealed in three-zone tube furnace		
CZTSSe	Sequential sputtered metallic Zn/Sn/Cu stack	Rapid thermal annealing at 580 ^{0}C for 5 min	7.0	Pawar et al., 2015
CZTSSe	RF/DC sputtering for Cu/SnS/ZnS/Mo stack	Selenization at 570 ^{0}C temperature for 60 min	8.03	Son et al., 2015
CZTS	RF magnetron sputtering of single CZTS target	Sulfurized at 500-700^0C for 10 min.	3.07	Dalapati et al., 2015
CZTSSe	DC/RF sputtering for Mo/Sn/Cu/ZnS/Sn/ZnS/Cu stack	Annealed at 300^0C for 20 min in Ar atmosphere followed by selenization at 570^0C for 15 min.	10.2	Li et al., 2016
CZTSSe	Stacked Cu-Sn-Zn by DC sputtering	540^0C for 10 min in graphite box under N_2 atm	9.24	Gang et al., 2016
CZTS	RF magnetron sputtering from CZTS target	Sulfurized at 400-550^0C for 30 min.	4.4	Feng et al., 2016

CZTSSe	ZnS/S/SnS/Cu sequential/ stack layer sputtering with Cu, SnS & ZnS target	Precursor annealed in furnace with the Se environment	9.1	Kim et al., 2016
CZTS	Co-sputtering of Cu/ZnS/SnS	Sulphurization using Rapid Thermal Processor in S atmosphere	6.6	Yan et al., 2016
CZTSe:Ge	Cu/SnCu/Zn metallic stacks by DC magnetron sputtering, Ge by thermal evaporation	Reactive annealing under Se (100mg) +Sn (5mg) atm at 400^{0}C for 30 min & 1.5 mbar Ar pressure then 550^{0}C for 15 min & 1 mbar Ar pressure	$\geq$10	Giraldo et al., 2016
CZTS	Cu/Zn/Zn Stacked Layer (Sequential Sputtering)	Sulfurization at 590^{0}C for 10 min in presence of sulfur	6.9	Jiang et al., 2016
CZTSSe	DC Sputtering of CZTS target	Annealing range- 400-600^{0}C in presence of Chalcogen vapor or H_2 (S, Se)	9.7	Altamura et al., 2016
CZTSSe	CZTS deposited by compound target using RF magnetron sputtering	Sulfurization/Selenization at 570^{0}C for 1 hrs in N_2 ambient (with different Se/S ratio)	6.9	Li et al., 2017
CZTS	Compound CZTZ target used for sputtering	Sulfurization at 570^{0}C in a sulfur atmosphere for 30 min with the S zone temperature held at 250^{0}C	3.74	Cui et al., 2017
CZTS	Double layer stack by co-sputter Cu/ZnS/SnS precursors	Sulfurization treatment using a Rapid Thermal Processor in a sulfur and SnS containing atmosphere	7.57	Yan et al., 2017
CZTS	2-layers CZTS deposition using Cu, Sn, and ZnS targets by RF magnetron sputtering to form a Cu/Sn/ZnS	Sulfurized at 853^{0}K for 20 min in 20% H_2S and 80% N_2 at atmospheric pressure	9.4	Tajima et al., 2017
CZTS	Reactive co-sputtering using Cu, Zn and Sn target (Cu, Zn by DC-Sput, Sn by Rf-Sput.)	Sulfurization at 570^{0}C for 40 min under S_2 vapor (in Ar atm)	3.72	Li et al., 2017

CZTSSe	RF Sputtering using CZTS quaternary target	Annealing at 560^0C for 10 min in S/Se atm	3.38	Yang et al., 2017
CZTS	Reactive co-sputtering of CuS, Zn, and Sn targets	Annealing at 560^0C for 10 min in presence of S_2 under Ar atm	3.9	Ren et al., 2017
CZTS	RF-magnetron sputtering by stoichiometric Cu_2ZnSnS_4 target	Annealed in a furnace at 600 °C for 10 minutes with S_2 powder	≈4.4	Dalapati et al., 2017
CZTSSe	RF sputtering using quaternary CZTS target	Annealed in furnace at 300-560 °C for 30 min in presence of H_2Se gas	9.6	Sun et al., 2018
CZTS	Co-sputter of Cu/ZnS/SnS precursors	Rapid thermal annealing at 560 °C with SnS and S for 20 min	~11	Yan et al., 2018
CZTS	Co-sputter of Cu/ZnS/SnS precursors	Annealed in S atmosphere at 610 °C for 10 min	8.2	Ma et al., 2019
CZTSSe	Co-sputter of Cu/ZnS/SnS precursors	Annealed at 600 °C for 1 hr with Se and S+Se atmosphere	7.1	Temgoua et al., 2019
CZTSSe	Sequential deposition Cu/SnS/ZnS by DC/RF magnetron sputtering	Rapid thermal annealing at 250-590 °C with SeS_2 and Se	9.47	Son et al., 2019
CZTS	Stacked metallic layer Cu/Zn/Cu/Sn by RF magnetron sputtering	Annealed at 350-590 °C for different time in presence of sulfur	8.44	Lu et al., 2020
CZTSSe	Co-sputtering with two CZTS quaternary ceramic target, contains different Cu	Annealed with H_2Se gas for 400 °C/ 20 min followed by 520 °C/ 20 min	9.13	Ren et al., 2020
CZTS	Sequential sputtering of Zn/Cu/Sn/Cu by magnetron sputtering	Rapid annealing at 250-325 °C for 10 min	8.56-9.75	Lu et al., 2021

CZTSSe	RF sputter using CZTS quaternary target	Two stage selenization with Se at 230 °C for 5 min followed by 540 °C for 15 min	7.9	Cheng et al., 2021
CZTSSe	Stack Cu-Zn-Sn by DC magnetron sputtering	Annealed at 300 °C for 1 hr followed by 520 °C for 7.5 in S and Se atm	9.82	Jeong et al., 2021
CZTS	RF sputtered CZTS by quaternary target	In-situ annealing at 450 °C	2.6	Simya et al., 2022

REFERENCES

http://www.un.org/climatechange/mitigation/reducing-emissions/

https://www.nrel.gov/pv/cell-efficiency.html

Amal, M.I., Kim, K.H., 2013. Crystallization of kesterite Cu_2ZnSnS_4 prepared by the sulfurization of sputtered Cu–Zn–Sn precursors. Thin Solid Films 534, 144–148.

Atasoy, Y., Olgar, M. A., Bacaksiz., E., 2019. Structural, optical and schottky diode properties of CZTS thin films grown by two-stage method, J. Mater. Sci. Mater. Electro., 30, 10435-10442.

Aydin, R., Akyuz, I., 2020. Two-stage production and characterization of Cu-poor kesterite CZTS absorber layers. Optik (Stuttg). 200, 163407.

Baca, A.G., Ren, F., Zolper, J.C., Briggs, R.D., Pearton, S.J., 1997. A survey of ohmic contacts to III-V compound semiconductors. Thin Solid Films 308–309, 599–606.

Bansal, N., Pandey, K., Singh, K., Mohanty, B.C., 2019. Growth control of molybdenum thin films with simultaneously improved adhesion and conductivity via sputtering for thin film solar cell application. Vacuum 161.

Pandey, K., Mohanty, B.C., 2021. Influencing mechanism of post-sulfurization with sulfur flakes on phase evolution and Schottky diode characteristic of Cu_2ZnSnS_4 thin films sputter deposited from a single target. Solar Energy, 228, 333-338.

Bansal, N., Singh, K., Mohanty, B.C., 2020. Studies of various alkali metal oxides containing calcium silicate glasses as substrate for solar cell application, Thesis.

Barkhouse, D.A.R., Gunawan, O., Gokmen, T., Todorov, T.K., Mitzi, D.B., 2012. Device characteristics of a 10.1% hydrazine-processed $Cu_2ZnSn(Se,S)_4$ solar cell. Prog. Photovoltaics Res. Appl. 20, 6–11.

Ben-Chorin, M., Möller, F., Koch, F., 1995. Band alignment and carrier injection at the porous-silicon-crystalline- silicon interface. J. Appl. Phys. 77, 4482–4488.

Bernardini, G.P., Borrini, D., Caneschi, A., Di Benedetto, F., Gatteschi, D., Ristori, S., Romanelli, M., 2000. EPR and SQUID magnetometry study of Cu_2FeSnS_4 (stannite) and Cu_2ZnSnS_4 (kesterite). Phys. Chem. Miner. 2000 277 27, 453–461.

Bodeux, R., Mollica, F., Delbos, S., 2015. Growth of $Cu_2ZnSnSe_4$ by cosputtering and reactive annealing atmosphere. Sol. Energy Mater. Sol. Cells 132, 67–73.

Boutebakh, F. Z., Zeggar, M. L., Attaf, N. M., Aida, S., 2017. Electrical properties and back contact study of CZTS/ZnS hetrojunction, Optik 144, 180-190.

Brammertz, G., Buffière, M., Mevel, Y., Ren, Y., Zaghi, A.E., Lenaers, N., Mols, Y., Koeble, C., Vleugels, J., Meuris, M., Poortmans, J., 2013. Correlation between physical, electrical, and optical properties of Cu 2ZnSnSe4 based solar cells. Appl. Phys. Lett. 102.

Chalapathi, U., Uthanna, S., Sundara Raja, V., 2015. Growth of Cu_2ZnSnS_4 thin films by a two-stage process - Effect of incorporation of sulfur at the precursor stage. Sol. Energy Mater. Sol. Cells 132, 476–484.

Chalapathy, R. B. V., Biccari, F., Chierchia, R., Valentini, M., Mangiapane, P., Salza, E., Malerba, C., Leonor, C., Ricardo, A., Mannarino, L., Scardi, P., Mittiga, A., 2011. Fabrication of Cu_2ZnSnS_4 solar cells by sulfurization of evaporated precursors. Energy Procedia 10, 187–191.

Chalapathy, R. B. V., Gwang Sun Jung, and Byung Tae Ahn. "Fabrication of CZTS films by sulfurization of Cu/ZnSn/Cu precursor layers in sulfur atmosphere for solar cells." Sol. Energy Mater. Sol. Cells 95.12 (2011): 3216-3221.

Chandel, T., Thakur, V., Halaszova, S., Prochazka, M., Haško, D., Velic, D., Poolla, R., 2018. Growth and Properties of Sprayed CZTS Thin Films. J. Electron. Mater. 47.

Chen, S., Yang, J.-H., Gong, X.-G., Walsh, A., Wei, S.-H., 2010. Intrinsic point defects and complexes in the quaternary kesterite semiconductor Cu2ZnSnS4. Phys. Rev. B. 81, 245204.

Choudhari, J. N., Raviprakash, Y., Bellarmine, F., Rao, M. S.,Pinto, R., 2020. Investigation on the sulfurization temperature dependent phase and defect formation of sequentially evaporated Cu-rich CZTS thin films. Solar Energy, 201,348-361.

Chen, S., Gong, X., Walsh, A., Wei, S.-H., 2010. Defect physics of the kesterite thin-film solar cell absorber Cu_2ZnSnS_4. Appl. Phys. Lett. 96, 021902.

Chen, G., Liu, W., Jiang, G., Pan, B., Zhu, C., 2013. Effect of compact structure on the phase transition in the oxides derived Cu2ZnSnSe4 thin films. Sol. Energy 92, 172–175.

Chen, S., Walsh, A., Gong, X. G., Wei, S. H.,2013. Classification of Lattice Defects in the Kesterite Cu_2ZnSnS_4 and $Cu_2ZnSnSe_4$ Earth-Abundant Solar Cell Absorbers. Adv.Mater. 25, 1522–1539.

Chen, G., Yuan, C., Liu, J., Deng, Y., Jiang, G., Liu, W., Zhu, C., 2014. Low cost preparation of Cu2ZnSnS4 and Cu2ZnSn(SxSe1-x)4 from binary sulfide nanoparticles for solar cell application. J. Power Sources 262, 201–206.

Chen, S.Y., Zheng, C., Fuhrer, M. S., Yan, J., 2015. Helicity-Resolved Raman Scattering of MoS2, MoSe2, WS2, and WSe2 Atomic Layers. Nano Lett. 15, 2526−2532.

Cheng, K., Suo, H., Gao, X., Zhang, Z., Liu, Z., Shen, Q., Liu, J., Liu, X., Du, Z., 2021. Performance enhancement of $Cu_2ZnSn(S, Se)_4$ solar cells by post-selenization of absorber layer in thermal-cracked selenium atmosphere. Sol. Energy Mater. Sol. Cells 219.

Chernomordik, B.D., Béland, A.E., Deng, D.D., Francis, L.F., Aydil, E.S., 2014. Microstructure evolution and crystal growth in Cu_2ZnSnS_4 thin films formed by annealing colloidal nanocrystal coatings. Chem. Mater. 26, 3191–3201.

Chernomordik, B.D., Ketkar, P.M., Hunter, A.K., Béland, A.E., Deng, D.D., Aydil, E.S., 2016. Microstructure Evolution during Selenization of Cu_2ZnSnS_4 Colloidal Nanocrystal Coatings. Chem. Mater. 28, 1266–1276.

Cheung, S.K., Cheung, N.W. 1986. Extraction of Schottky diode parameters from forward current- voltage Characteristics. Appl. Phys. Lett. 49, 85-87.

Cho, J.W., Ismail, A., Park, S.J., Kim, W., Yoon, S., Min, B.K., 2013. Synthesis of Cu_2ZnSnS_4 thin films by a precursor solution paste for thin film solar cell applications. ACS Appl. Mater. Interfaces 5.

Choudhary, G., Hansen, H., 1998. Human health perspective of environmental exposure to hydrazines: A review. Chemosphere 37, 801–843.

Cui, H., Liu, X., Sun, L., Liu, F., Yan, C., Hao, X., 2017. Fabrication of Efficient Cu_2ZnSnS_4 Solar Cells by Sputtering Single Stoichiometric Target. Coatings 2017, Vol. 7, Page 19 7, 19.

Dalapati, G.K., Batabyal, S.K., Masudy-Panah, S., Su, Z., Kushwaha, A., Wong, T.I., Liu, H.F., Bhat, T., Iskander, A., Lim, Y.F., Wong, L.H., Tripathy, S., Chi, D., 2015. Sputter grown sub-micrometer thick Cu_2ZnSnS_4 thin film for photovoltaic device application. Mater. Lett. 160, 45–50.

Dalapati, G.K., Zhuk, S., Masudy-Panah, S., Kushwaha, A., Seng, H.L., Chellappan, V., Suresh, V., Su, Z., Batabyal, S.K., Tan, C.C., Guchhait, A., Wong, L.H., Wong, T.K.S., Tripathy, S., 2017. Impact of molybdenum out diffusion and interface quality on the performance of sputter grown CZTS based solar cells. Sci. Reports 2017 71 7, 1–12.

Delrue H., Vermeersch R., Bosscher W. De, Aps Freddy, 2005. Method to reduce thermal stresses in a sputter target, US Patent WO2005090631A1,.

Demir, K.Ç., 2021. The investigation of the corrosion behavior of CZTS thin films prepared via electrodeposition. Mater. Sci. Semicond. Process. 123, 105553.

Devi, R. A., Latha, M., Velumani, S., Cruz, J. S., Murali, B., Chavez-Carvayar, J. A., Pulgarın-Agudeloe F. A., and Vigil-Galan, O., 2019. $Cu_2ZnSn(S,Se)_4$ thin-films prepared from selenized nanocrystals ink,. RSC Adv. 9, 18420–18428.

El kissani, A., Nkhaili, L., Ammar, A., Elassali, K., Outzourhit, A., 2016. Synthesis, annealing, characterization, and electronic properties of thin films of a quaternary semiconductor; copper zinc tin sulfide. Spectrosc. Lett. 49, 343–347.

Emrani, A., Vasekar, P., Westgate, C.R., 2013. Effects of sulfurization temperature on CZTS thin film solar cell performances. Sol. Energy 98, 335–340.

Emrani, A., Vasekar, P., Westgate, C.R., 2013. Effects of sulfurization temperature on CZTS thin film solar cell performances. Sol. Energy 98, 335–340.

Ennaoui, A., Lux-Steiner, M., Weber, A., Abou-Ras, D., Kötschau, I., Schock, H.W., Schurr, R., Hölzing, A., Jost, S., Hock, R., Voß, T., Schulze, J., Kirbs, A., 2009. Cu_2ZnSnS_4 thin film solar cells from electroplated precursors: Novel low-cost perspective. Thin Solid Films 517, 2511–2514.

Feng, J., Huang, X., Chen, W., Wu, J., Lin, H., Cheng, Q., Yun, D., Zhang, F., 2016. Fabrication and characterization of Cu_2ZnSnS_4 thin films for photovoltaic application by low-cost single target sputtering process. Vacuum 126, 84–90.

Fernandes, P.A., Salomé, P.M.P., Da Cunha, A.F., 2009. Precursors' order effect on the properties of sulfurized Cu $_2$ZnSnS$_4$ thin films. Semicond. Sci. Technol. 24.

Fernandes, P.A., Salomé, P.M.P., Da Cunha, A.F., 2011. Study of polycrystalline Cu_2ZnSnS_4 films by Raman scattering. J. Alloys Compd. 509.

Fernandes, P.A., Salomé, P.M.P., Sartori, A.F., Malaquias, J., Da Cunha, A.F., Schubert, B.A., González, J.C., Ribeiro, G.M., 2013. Effects of sulphurization time on Cu_2ZnSnS_4 absorbers and thin films solar cells obtained from metallic precursors. Sol. Energy Mater. Sol. Cells 115, 157–165.

Fouad, S.S., El Radaf, I.M., Sharma, P., El-Bana, M.S., 2018. Multifunctional CZTS thin films: Structural, optoelectrical, electrical and photovoltaic properties. J. Alloys Compd. 757.

Frantz, J.A., Bekele, R.Y., Nguyen, V.Q., Sanghera, J.S., Bruce, A., Frolov, S. V., Cyrus, M., Aggarwal, I.D., 2011. $Cu(In,Ga)Se_2$ thin films and devices sputtered from a single target without additional selenization. Thin Solid Films 519, 7763–7765.

Friedlmeier Th. M., Proc 1997. The Effects of Additional KI Salts on Non-vacuum Coated $Cu_2ZnSn(SSe)_4$ Films. Sol. Energy Conf., Bedford . 1242.

Fukano, T., Tajima, S., Ito, T., 2013. Enhancement of conversion efficiency of Cu_2ZnSnS_4 thin film solar cells by improvement of sulfurization conditions. Appl. Phys. Express 6, 62301.

Green, M. A., Dunlop, Ewan D., Hohl-Ebinger, J., Yoshita, M., Kopidakis, N., Hao, X., 2022. Solar cell efficiency tables (version 59). Prog Photovolt Res Appl. 30, 3–12

Gang, M.G., Shin, S.W., Hong, C.W., Gurav, K. V., Gwak, J., Yun, J.H., Lee, J.Y., Kim, J.H., 2016. Sputtering processed highly efficient $Cu_2ZnSn(S,Se)_4$ solar cells by a low-cost, simple, environmentally friendly, and up-scalable strategy. Green Chem. 18, 700–711.

Ge, J., Yan, Y., 2017. Synthesis and characterization of photoelectrochemical and photovoltaic Cu_2BaSnS_4 thin films and solar cells. J. Mater. Chem. C 5, 6406–6419.

Ghobadi, N., 2013. Band gap determination using absorption spectrum fitting procedure. Int. Nano Lett. 3.

Gokmen, T., Gunawan, O., Todorov, T. K., Mitzi, D. B., 2013. Band tailing and efficiency limitation in kesterite solar cells. Appl. Phys. Lett. 103, 103506.

Gopal, V., Gautam, N., Plis, E., Krishna, S., 2015. Modelling of current-voltage characteristics of infrared photo-detectors based on type - II InAs/GaSb super-lattice diodes with unipolar blocking layers. AIP Adv. 5, 97132.

Grenet, L., Bernardi, S., Kohen, D., Lepoittevin, C., Noël, S., Karst, N., Brioude, A., Perraud, S., Mariette, H., 2012. $Cu_2ZnSn(S_{1-x}Se_x)_4$ based solar cell produced by selenization of vacuum deposited precursors. Sol. Energy Mater. Sol. Cells 101, 11–14.

Gunawan, O., Gokmen, T., Mitzi, B.D., 2014. Suns-VOC characteristics of high performance kesterite solar cells. J. Appl. Phys. 116, 084504.

Guo, Q., Ford, G.M., Yang, W.C., Walker, B.C., Stach, E.A., Hillhouse, H.W., Agrawal, R., 2010. Fabrication of 7.2% efficient CZTSSe solar cells using CZTS nanocrystals. J. Am. Chem. Soc. 132, 17384–17386.

Gupta, I., Mohanty, B.C., 2019. Evaluating the role of precursor concentration in facile conformal coating of sub-micrometer thick Cu_2ZnSnS_4 films using non-toxic ethanol based solutions, Appl. Surf. Sci. 494, 795–804.

Gupta, I., Mohanty, B.C., 2019. Eliminating secondary phases: Understanding kesterite phase evolution of Cu_2ZnSnS_4 thin films grown from ethanol based solutions with high photosensitivity. Sol. Energy 181, 214–221.

Gupta, I., Pandey, K., Jain, A.K., Malar, P., Mohanty, B.C., 2021. Critical Influence of Annealing Configuration in Kesterite Phase Evolution During Growth of Cu_2ZnSnS_4 Thin Films from Non-Toxic Environment-Friendly Solutions. J. Electron. Mater. 1–9.

Hall, S. R., Szymanski, J. T., & Stewart, J. M. (1978). Kesterite, Cu< 2)(Zn, Fe) SnS< 4), and stannite, Cu< 2)(Fe, Zn) SnS< 4), structurally similar but distinct minerals. The Canadian Mineralogist, 16(2), 131-137.

He, J., Sun, L., Zhang, K., Wang, W., Jiang, J., Chen, Y., Yang, P., Chu, J., 2013. Effect of post-sulfurization on the composition, structure and optical properties of Cu_2ZnSnS_4 thin films deposited by sputtering from a single quaternary target. Appl. Surf. Sci. 264, 133–138.

Hegedus, S.S., Shafarman, W.N., 2004. Thin-film solar cells: device measurements and analysis. Prog. Photovoltaics Res. Appl. 12, 155–176.

Henry, J., Mohanraj, K., Sivakumar, G., 2016. Electrical and optical properties of CZTS thin films prepared by SILAR method. J. Asian Ceram. Soc. 4, 81–84.

Henry, J., Mohanraj, K., Sivakumar, G., 2017. Effect of pH-induced on the photosensitivity of non-toxic Cu_2ZnSnS_4 thin film by chemical bath deposition. Optik (Stuttg). 141, 139–145.

Henry, J., Mohanraj, K., Sivakumar, G., 2020. Thermally evaporated CZTSe thin films for solar cell application: Study on the effect of annealing time. Part. Sci. Technol. 38.

Huang, S., Luo, W., Zou, Z., 2013. Band positions and photoelectrochemical properties of Cu_2ZnSnS_4 thin films by the ultrasonic spray pyrolysis method. J. Phys. D. Appl. Phys. 46, 235108.

Inamdar A.I., Jeon K.-Y., Woo H. seok, Jung W., Im H., Kim H, (2012) Controlled growth of Cu_2ZnSnS_4 (CZTS) thin films for heterojunction solar-cell applications, J. Korean Phys. Soc. 60 1730–1734.

Inamdar, A.I., Jeon, K.Y., seok Woo, H., Jung, W., Im, H., Kim, H., 2011. Synthesis of a Cu_2ZnSnS_4 (CZTS) absorber layer and metal doped ZnS buffer layer for heterojunction solar cell applications, ECS, 167–175.

Inamdar, A.I., Lee, S., Jeon, K.Y., Lee, C.H., Pawar, S.M., Kalubarme, R.S., Park, C.J., Im, H., Jung, W., Kim, H., 2013. Optimized fabrication of sputter deposited Cu_2ZnSnS_4 (CZTS) thin films. Sol. Energy 91, 196–203.

Islam, M. M., Halim, M. A., Sakurai,T., Sakai, N., kato, T., Sugimoto, H., Tampo, H., Shibata, H., Niki, S., Akimoto, K.,2015. Determination of deep-level defects in Cu2ZnSn(S,Se)4 thin-films using photocapacitance method. Appl. Phys. Lett. 106, 243905

Ito, K., Nakazawa, T., 1988. Electrical and optical properties of stannite-type quaternary semiconductor thin films. Jpn. J. Appl. Phys. 27, 2094–2097.

Jackson, P., Hariskos, D., Wuerz, R., Wischmann, W., Powalla, M., 2014. Compositional investigation of potassium doped Cu(In,Ga)Se_2 solar cells with efficiencies up to 20.8%. Phys. status solidi – Rapid Res. Lett. 8, 219–222.

Jeong, H., Nandi, R., Cho, J.Y., Pawar, P.S., Lee, H.S., Neerugatti, K.R.E., Kim, J.H., Heo, J., 2021. CZTSSe/Zn(O,S) heterojunction solar cells with 9.82% efficiency enabled via (NH4)2S treatment of absorber layer. Prog. Photovoltaics Res. Appl. 29, 1057–1067.

Jiang, J., Zhang, L., Wang, W., Hong, R., 2018. The role of sulphur in the sulfurization of CZTS layer prepared by DC magnetron sputtering from a single quaternary ceramic target. Ceram. Int. 44, 11597–11602.

Jimbo, K., Kimura, R., Kamimura, T., Yamada, S., Maw, W.S., Araki, H., Oishi, K., Katagiri, H., 2007. Cu_2ZnSnS_4-type thin film solar cells using abundant materials. Thin Solid Films 515, 5997–5999.

Jing-Jing, M., Ke-Xin, J., Bing-Cheng, L., Fei, F., Hui, X., Chao-Chao, Z., Chang-Le, C., 2010. Rectifying and Photovoltage Properties of ZnO:Al/p-Si Heterojunction. Chinese Phys. Lett. 27, 107304–107304.

Jo, Y.H., Mohanty, B.C., Yeon, D.H., Lee, S.M., Cho, Y.S., 2015. Single elementary target-sputtered $Cu_2ZnSnSe_4$ thin film solar cells. Sol. Energy Mater. Sol. Cells 132, 136–141.

Joshi, U.A., Maggard, P.A., 2012. CuNb 3O 8: A p-type semiconducting metal oxide photoelectrode. J. Phys. Chem. Lett. 3, 1577–1581.

Katagiri H., Hando, S., Hoshino, S., Ohashi, , Proc. 2003. World Conf. on Photovoltaic Energy Conversion-3, Osaka, 2874.

Katagiri, H., 2005. Cu_2ZnSnS_4 thin film solar cells, Thin Solid Films 480-481, 426-432.

Katagiri, H., Jimbo, K., Maw, W.S., Oishi, K., Yamazaki, M., Araki, H., Takeuchi, A., 2009. Development of CZTS-based thin film solar cells. Thin Solid Films 517, 2455–2460.

Katagiri, H., Jimbo, K., Tahara, M., Araki, H., Oishi, K., 2009. The influence of the composition ratio on CZTS-based thin film solar cells. MRS Online Proc. Libr. 2009 11651 1165, 1–12.

Katagiri, H., Jimbo, K., Yamada, S., Kamimura, T., Maw, W. S., Fukano, T., & Motohiro, T. (2008). Enhanced conversion efficiencies of Cu_2ZnSnS_4-based thin film solar cells by using preferential etching technique. Applied physics express, 1(4), 041201.

Katagiri, H., Saitoh, K., Washio, T., Shinohara, H., Kurumadani, T., Miyajima, S., 2001. Development of thin film solar cell based on Cu2ZnSnS4 thin films. Sol. Energy Mater. Sol. Cells 65, 141–148.

Katagiri, H., Saitoh, K., Washio, T., Shinohara, H., Kurumadani, T., Miyajima, S., 2001. Development of thin film solar cell based on Cu_2ZnSnS_4 thin films. Sol. Energy Mater. Sol. Cells 65, 141–148.

Katagiri, H., Sasaguchi, N., Hando, S., Hoshino, S., Ohashi, J., Yokota, T., 1997. Preparation and evaluation of Cu_2ZnSnS_4 thin films by sulfurization of E-B evaporated precursors. Sol. Energy Mater. Sol. Cells 49, 407–414.

Khanra, A., Gayen, R.N., 2018. Distribution of relaxation time in solution-processed polycrystalline CZTS thin films: Study of impedance spectroscopy. Ceram. Int. 44, 14095–14100.

Kim, G.Y., Kim, J.R., Jo, W., Son, D.H., Kim, D.H., Kang, J.K., 2014. Nanoscale observation of surface potential and carrier transport in $Cu_2ZnSn(S,Se)_4$ thin films grown by sputtering-based two-step process. Nanoscale Res. Lett. 9, 1–5.

Krishnan, A., Rishad Ali, K., Vishnu, G., Kannan, P., 2019. Towards phase pure CZTS thin films by SILAR method with augmented Zn adsorption for photovoltaic applications. Mater. Renew. Sustain. Energy 8, 1–8.

Kubelka, P.; Munk, F., 1931. A Contribution to the Optics of Pigments. Z. Technol. Phys. 12.

Kumar, J., Ingole, S., 2019. Evolution of the microstructural, electrical and optical characteristics of sol-gel derived Cu_2ZnSnS_4 thin films during sulfurization. Mater. Sci. Semicond. Process. 91, 31–40.

Li, J., Mitzi, D.B., Shenoy, V.B., 2011. Structure and electronic properties of grain boundaries in earth-abundant photovoltaic absorber $Cu_2ZnSnSe_4$. ACS Nano 5, 8613–8619.

Li, J., Wang, H., Luo, M., Tang, J., Chen, C., Liu, W., Liu, F., Sun, Y., Han, J., Zhang, Y., 2016. 10% Efficiency $Cu_2ZnSn(S,Se)_4$ thin film solar cells fabricated by magnetron sputtering with enlarged depletion region width. Sol. Energy Mater. Sol. Cells 149, 242–249.

Li, J.B., Chawla, V., Clemens, B.M., 2012. Investigating the Role of Grain Boundaries in CZTS and CZTSSe Thin Film Solar Cells with Scanning Probe Microscopy. Adv. Mater. 24, 720–723.

Li, W., Zhao, L., Zhang, K., Sun, H., Lai, Y., Jiang, Y., Jiang, L., Liu, F., Jia, M., 2017. Fabrication of Cu_2ZnSnS_4 thin film solar cells by annealing of reactively sputtered precursors. J. Alloys Compd. 701, 55–62.

Li, X., Cao, H., Dong, Y., Yue, F., Chen, Y., Xiang, P., Sun, L., Yang, P., Chu, J., 2017. Investigation of Cu_2ZnSnS_4 thin films with controllable Cu composition and its influence on photovoltaic properties for solar cells. J. Alloys Compd. 694, 833–840.

Liao, P., Zhao, X., Li, G., Shen, Y., Wang, M., 2018. A new method for fitting current–voltage curves of planar heterojunction perovskite solar cells. Nano-Micro Lett. 10, 1–8.

Lide, D.R., Baysinger, G., Berger, L.I., Goldberg, R.N., Kehiaian, H. V, Kuchitsu, K., Roth, D.L., Zwillinger, D., 2005. CRC Handbook of Chemistry and Physics Editor-in-Chief. CRC Press, Boca Raton, FL.

Lin, Y.P., Chi, Y.F., Hsieh, T.E., Chen, Y.C., Huang, K.P., 2016. Preparation of Cu_2ZnSnS_4 (CZTS) sputtering target and its application to the fabrication of CZTS thin-film solar cells. J. Alloys Compd. 654, 498–508.

Lin, Y.P., Hsieh, T.E., Chen, Y.C., Huang, K.P., 2017. Characteristics of $Cu_2ZnSn(S_xSe_{1-x})_4$ thin-film solar cells prepared by sputtering deposition using single quaternary Cu_2ZnSnS_4 target followed by selenization/sulfurization treatment. Sol. Energy Mater. Sol. Cells 162, 55–61.

Liu, F., Li, Y., Zhang, K., Wang, B., Yan, C., Lai, Y., Zhang, Z., Li, J., Liu, Y., 2010. In situ growth of Cu_2ZnSnS_4 thin films by reactive magnetron co-sputtering. Sol. Energy Mater. Sol. Cells 94, 2431–2434.

Liu, X., Feng, Y., Cui, H., Liu, F., Hao, X., Conibeer, G., Mitzi, B. D., Green, M., 2016.The current status and future prospects of kesteritesolar cells: a brief review. Prog.Photovolt:Res.Appl. 24, 879–898.

Lopes, T., Andrade, L., Ribeiro, H.A., Mendes, A., 2010. Characterization of photoelectrochemical cells for water splitting by electrochemical impedance spectroscopy. Int. J. Hydrogen Energy 35, 11601–11608.

Lu, X., Xu, B., Qin, X., Chen, Y., Yang, P., Chu, J., Sun, L., 2020. Modification of Back Contact in Cu_2ZnSnS_4 Solar Cell by Inserting Al-Doped ZnO Intermediate Layer. ACS Appl. Mater. Interfaces 12, 58060–58071.

Lu, X., Xu, B., Qin, X., Chen, Y., Yang, P., Chu, J., Sun, L., 2021. Heterojunction post-heat treatment process driving high efficiency for Cu_2ZnSnS_4 solar cell. Sol. Energy Mater. Sol. Cells 230.

Lundin, D., Minea, T., Gudmundsson, T. J., 2019. High Power Impulse Magnetron Sputtering: Fundamentals, Technologies, Challenges and Applications. Elsevier Science Ltd.

Ma, C., Lu, X., Xu, B., Zhao, F., An, X., Li, B., Yue, F., Jiang, J., Chen, Y., Sun, L., Chu, J., 2020. Effect of CZTS/CdS interfaces deposited with sputtering and CBD methods on Voc deficit and efficiency of CZTS solar cells. J. Alloys Compd. 817, 153329.

Malerba, C., Biccari, F., Ricardo, C.L.A., Valentini, M., Chierchia, R., Müller, M., Santoni, A., Esposito, E., Mangiapane, P., Scardi, P., Mittiga, A., 2014. CZTS stoichiometry effects on the band gap energy. J. Alloys Compd. 582, 528–534.

Mamedov, D., Klopov, M., Karazhanov, S.Z., 2017. Influence of Cu_2S, SnS and $Cu_2ZnSnSe_4$ on optical properties of Cu_2ZnSnS_4. Mater. Lett. 202, 70–72.

Miller, D. W., Warren, C.W., Gunawan, O., Gokmen, T., Mitzi, D. B., Cohen, J. D., 2012. Electronically active defects in the Cu2ZnSn(Se,S)4 alloys as revealed by transient photocapacitance spectroscopy. Appl. Phys. Lett. 101, 142106.

Minbashi, M., Ghobadi, A., Yazdani, E., Ahmadkhan Kordbacheh, A., Hajjiah, A., 2020. Efficiency enhancement of CZTSSe solar cells via screening the absorber layer by examining of different possible defects. Sci. Rep. 10.

Mitzi, D.B., Gunawan, O., Todorov, T.K., Wang, K., Guha, S., 2011. The path towards a high-performance solution-processed kesterite solar cell. Sol. Energy Mater. Sol. Cells 95, 1421–1436.

Mitzi, B. D., Gunawan, O., Todorovand, K.T., Barkhouse, R.A.D., 2013. Prospects and performancelimitations forCu–Zn–Sn–S–Se photovoltaictechnology. Phil. Trans. R. Soc. A 371, 20110432.

Moholkar, A. V., Shinde, S.S., Babar, A.R., Sim, K.U., Lee, H.K., Rajpure, K.Y., Patil, P.S., Bhosale, C.H., Kim, J.H., 2011. Synthesis and characterization of Cu_2ZnSnS_4 thin films grown by PLD: Solar cells. J. Alloys Compd. 509, 7439–7446.

Nagoya, A., Asahi, R., Wahl, R., Kresse, G., 2010. Defect formation and phase stability of Cu_2ZnSnS_4 photovoltaic material. Phys. Rev. B - Condens. Matter Mater. Phys. 81, 113202.

Nakamura, R., Tanaka, K., Uchiki, H., Jimbo, K., Washio, T., Katagiri, H., 2014. Cu_2ZnSnS_4 thin film deposited by sputtering with Cu_2ZnSnS_4 compound target. Jpn. J. Appl. Phys. 53, 02BC10.

Nakayama, N., Ito, K., 1996. Sprayed films of stannite Cu_2ZnSnS_4. Appl. Surf. Sci. 92, 171–175.

Nguyen, D.C., Ito, S., Dung, D.V.A., 2015. Effects of annealing conditions on crystallization of the CZTS absorber and photovoltaic properties of $Cu_2(Zn,Sn)(S,Se)_2$ solar cells. J. Alloys Compd. 632, 676–680.

Norde, H. 1979. A modified forward I-V plot for Schottky diodes with high series resistance. J. Appl. Phys. 50, 5052-5053.

Olekseyuk, I.D., Dudchak, I. V., Piskach, L. V., 2004. Phase equilibria in the Cu_2S-ZnS-SnS_2 system. J. Alloys Compd. 368, 135–143.

Olgar, M.A., 2019. Optimization of sulfurization time and temperature for fabrication of Cu_2ZnSnS_4 (CZTS) thin films. Superlattices Microstruct. 126, 32–41.

Olgar, M.A., Tomakin, M., Kucukomeroglu, T., Bacaksiz, E., 2019. Growth of Cu_2ZnSnS_4 (CZTS) thin films using short sulfurization periods. Mater. Res. Express 6, 56401.

Ou, K.L., Fan, J.C., Chen, J.K., Huang, C.C., Chen, L.Y., Ho, J.H., Chang, J.Y., 2012. Hot-injection synthesis of monodispersed $Cu_2ZnSn(S_xSe_{1-x})_4$ nanocrystals: Tunable composition and optical properties. J. Mater. Chem. 22, 14667–14673.

Pandey, K., Mohanty, B.C., 2021. A thin Cu interlayer-mediated control of phase evolution of Cu_2ZnSnS_4 thin films grown by RF magnetron sputtering of a single elementary target with high white light sensitivity. Appl. Surf. Sci. 539, 148149.

Pandiyan, R., Oulad Elhmaidi, Z., Sekkat, Z., Abd-lefdil, M., El Khakani, M.A., 2017. Reconstructing the energy band electronic structure of pulsed laser deposited CZTS thin films intended for solar cell absorber applications. Appl. Surf. Sci. 396, 1562–1570.

Paranthaman, M.P., Wong-Ng, W., Bhattacharya, R.N., 2015. Semiconductor materials for solar photovoltaic cells. Semicond. Mater. Sol. Photovolt. Cells 1–275.

Patil, S.J., Lokhande, V.C., Lee, D.W., Lokhande, C.D., 2016. Electrochemical impedance analysis of spray deposited CZTS thin film: Effect of Se introduction. Opt. Mater. (Amst). 58, 418–425.

Pawar, S.M., Inamdar, A.I., Gurav, K. V., Shin, S.W., Gwak, J., Jo, Y., Yun, J.H., Pak, H., Kwon, S., Kim, H., Kim, J.H., Im, H., 2015. Fabrication of $Cu_2ZnSn(S_xSe_{1-x})_4$ thin film solar cell by single step sulfo-selenization of stacked metallic precursors. Curr. Appl. Phys. 15, 59–63.

Persson, C., 2010. Electronic and optical properties of Cu_2ZnSnS_4 and $Cu_2ZnSnSe_4$. J. Appl. Phys. 107, 53710.

Polizzotti, A., Repins, I. L., Noufi, R., Wei, S.-H., Mitzi,D. B., 2013. The State and Future Prospects of Kesterite Photovoltaics. Energy Environ. Sci. 6, 3171.

Pür, F.Z., Tataroğlu, A., 2012. Analysis of the series resistance and interface states of Au/Si3N4/n-Si (metal–insulator–semiconductor) Schottky diodes using I–V characteristics in a wide temperature range. Phys. Scr. 86, 35802.

Rawat, K., Shishodia, P.K., 2016. Enhancement of photosensitivity in bismuth doped Cu_2ZnSnS_4thin films, Phys. Status Solidi RRL 10, 890–894.

Redinger, A., Berg, D.M., Dale, P.J., Siebentritt, S., 2011. The consequences of kesterite equilibria for efficient solar cells. J. Am. Chem. Soc. 133, 3320–3323.

Ren, G., Zhuang, D., Zhao, M., Wei, Y., Wu, Y., Li, X., Lyu, X., Wang, C., Hu, L., Wei, J., Gong, Q., 2020. Influences of Cu concentration on electrical properties of CZTSSe absorbers and their device performances. Vacuum 173, 109121.

Ren, Y., Richter, M., Keller, J., Redinger, A., Unold, T., Donzel-Gargand, O., Scragg, J.J.S., Platzer Björkman, C., 2017. Investigation of the SnS/Cu2ZnSnS4 Interfaces in Kesterite Thin-Film Solar Cells. ACS Energy Lett. 2, 976–981.

Ren, Y., Ross, N., Larsen, J.K., Rudisch, K., Scragg, J.J.S., Platzer-Björkman, C., 2017. Evolution of Cu_2ZnSnS_4 during Non-Equilibrium Annealing with Quasi-in Situ Monitoring of Sulfur Partial Pressure. Chem. Mater. 29, 3713–3722.

Repins, I., Beall, C., Vora, N., Dehart, C., Kuciauskas, D., Dippo, P., To, B., Mann, J., Hsu, W.C., Goodrich, A., Noufi, R., 2012. Co-evaporated $Cu_2ZnSnSe_4$ films and devices. Sol. Energy Mater. Sol. Cells 101, 154–159.

Roe, F.J.C., Grant, G.A., Millican, D.M., 1967. Carcinogenicity of Hydrazine and 1,1-Dimethylhydrazine for Mouse Lung. Nat. 1967 2165113 216, 375–376.

Samji, S. K., Tiwari, B., Surendra, M. K., and Rao, M. S. R., 2014. Light induced phase change in Cu2−xZn1.3SnS4 thin films. Appl. Phys. Lett. 104, 152106.

Samji, S. K., Maanam, R., Rao, M. S. R., 2016. Do defects get ordered in Cu2ZnSnS4?. Scripta Materialia, 117, 11–15.

Samji, S. K., Rao, M. S. R., 2021. How different are CZTS grain boundaries? Scripta Materialia, 194, 113605

Schorr, S., 2011. The crystal structure of kesterite type compounds: A neutron and X-ray diffraction study. Sol. Energy Mater. Sol. Cells 95, 1482–1488.

Scofield, J. H., Duda, A., Albin, D., Ballard, B.L., Predecki, P.K., 1995. Sputtered molybdenum bilayer back contact for copper indium diselenide-based polycrystalline thin-film solar cells. Thin Solid Films, 260, 26-31.

Scragg, J.J., Dale, P.J., Peter, L.M., 2008. Towards sustainable materials for solar energy conversion: Preparation and photoelectrochemical characterization of Cu_2ZnSnS_4. Electrochem. commun. 10, 639–642.

Scragg, J.J., Ericson, T., Fontané, X., Izquierdo-Roca, V., Pérez-Rodríguez, A., Kubart, T., Edoff, M., Platzer-Björkman, C., 2014. Rapid annealing of reactively sputtered precursors for Cu_2ZnSnS_4 solar cells. Prog. Photovoltaics Res. Appl. 22, 10–17.

Scragg, J.J., Ericson, T., Kubart, T., Edoff, M., Platzer-Björkman, C., 2011. Chemical insights into the instability of cu2znsns4 films during annealing. Chem. Mater. 23, 4625–4633.

Scragg, J.J., Kubart, T., Wätjen, J.T., Ericson, T., Linnarsson, M.K., Platzer-Björkman, C., 2013. Effects of back contact instability on Cu_2ZnSnS_4 devices and processes. Chem. Mater. 25, 3162–3171.

Seol, J.S., Lee, S.Y., Lee, J.C., Nam, H.D., Kim, K.H., 2003. Electrical and optical properties of Cu_2ZnSnS_4 thin films prepared by rf magnetron sputtering process. Sol. Energy Mater. Sol. Cells 75, 155–162.

Servaites, J.D., Ratner, M.A., Marks, T.J., 2011. Organic solar cells: A new look at traditional models. Energy Environ. Sci. 4, 4410-4422.

Shah, J.M., Li, Y.L., Gessmann, T., Schubert, E.F., 2003. Experimental analysis and theoretical model for anomalously high ideality factors ($n \gg 2.0$) in AlGaN/GaN p-n junction diodes. J. Appl. Phys. 94, 2627–2630.

Shi, J.H., Li, Z.Q., Zhang, D.W., Liu, Q.Q., Sun, Z.Z., Huang, S.M., 2011. Fabrication of Cu(In, Ga)Se_2 thin films by sputtering from a single quaternary chalcogenide target. Prog. Photovoltaics Res. Appl. 19, 160–164.

Shin, B., Gunawan, O., Zhu, Y., Bojarczuk, N.A., Chey, S.J., Guha, S., 2013. Thin film solar cell with 8.4% power conversion efficiency using an earth-abundant Cu_2ZnSnS_4 absorber. Prog. Photovoltaics Res. Appl. 21, 72–76.

Sigmund, P., 1969. Theory of sputtering. I. Sputtering yield of amorphous and polycrystalline targets. Phys. Rev. 184, 383–416.

Simon Sze M., Li Y., Kwok Ng K., 2021. Physics of Semiconductor Devices, 4th Edition, (John Wiley and Sons, New York) 1-944.

Simya, O.K., Vijayaraghavan, T., Subramanian, B., Ashok, A.M., 2022. Effect of RF sputter power on deposition of CZTX (XS, Se) active layer without selenization/sulfurization, for solar cell applications. J. Alloys Compd. 898, 162838.

Singh, O.P., Vijayan, N., Sood, K.N., Singh, B.P., Singh, V.N., 2015. Controlled substitution of S by Se in reactively sputtered CZTSSe thin films for solar cells. J. Alloys Compd. 648.

Skromme, B.J., 2003. in Encyclopedia of Materials: Science and Technology.

Son, D.H., Kim, D.H., Park, S.N., Yang, K.J., Nam, D., Cheong, H., Kang, J.K., 2015. Growth and Device Characteristics of CZTSSe Thin-Film Solar Cells with 8.03% Efficiency. Chem. Mater. 27, 5180–5188.

Son, D.H., Kim, Y.I., Kim, S.H., Nam, D., Cheong, H., Kang, J.K., Yang, K.J., Kim, D.H., 2019. Effects of S and Se contents on the physical and photovoltaic properties of $Cu_2ZnSn(S_X, Se_{1-X})_4$ thin films: achieving a PCE of 9.47%. J. Mater. Chem. A 7, 22986–22995.

Sripan, C., Madhavan, V.E., Viswanath, A.K., Ganesan, R., 2017. Sulfurization and annealing effects on thermally evaporated CZTS films. Mater. Lett. 189, 110–113.

Sun, L., He, J., Chen, Y., Yue, F., Yang, P., Chu, J., 2012. Comparative study on Cu_2ZnSnS_4 thin films deposited by sputtering and pulsed laser deposition from a single quaternary sulfide target. J. Cryst. Growth 361, 147–151.

Sun, L., He, J., Kong, H., Yue, F., Yang, P., Chu, J., 2011. Structure, composition and optical properties of Cu_2ZnSnS_4 thin films deposited by Pulsed Laser Deposition method. Sol. Energy Mater. Sol. Cells 95, 2907–2913.

Sun, R., Zhuang, D., Zhao, M., Gong, Q., Wei, Y., Ren, G., Wu, Y., 2018. $Cu_2ZnSnSSe_4$ solar cells with 9.6% efficiency via selenizing Cu-Zn-Sn-S precursor sputtered from a quaternary target. Sol. Energy Mater. Sol. Cells 174, 42–49.

Sun,R., Zhao,M., Zhuang,D., Gong,Q., Xie,M., Ouyang,L., Guo,L., Zhang,L., 2016. Effects of selenization on phase transition and S/(S+Se) ratios of as-deposited Cu_2ZnSnS_4 absorbers sputtered by a quaternary target, Mater. Lett. 164, 140–143.

Suryawanshi, M.P., Ghorpade, U. V., Suryawanshi, U.P., He, M., Kim, J., Gang, M.G., Patil, P.S., Moholkar, A. V., Yun, J.H., Kim, J.H., 2017. Aqueous-solution-processed $Cu_2ZnSn(S,Se)_4$ thin-film solar cells via an improved successive ion-layer-adsorption-reaction sequence. ACS Omega 2.

Suryawanshi, M.P., Shin, S.W., Ghorpade, U. V., Gurav, K. V., Agawane, G.L., Hong, C.W., Yun, J.H., Patil, P.S., Kim, J.H., Moholkar, A. V., 2014. A chemical approach for synthesis of photoelectrochemically active Cu_2ZnSnS_4 (CZTS) thin films. Sol. Energy 110.

Swami, S.K., Chaturvedi, N., Kumar, A., Chander, N., Dutta, V., Kumar, D.K., Ivaturi, A., Senthilarasu, S., Upadhyaya, H.M., 2014. Spray deposited copper zinc tin sulphide (Cu_2ZnSnS_4) film as a counter electrode in dye sensitized solar cells. Phys. Chem. Chem. Phys. 16, 23993–23999.

Sze, S.M., Li, Y., Kwok Ng, K., Physics of Semiconductor Devices, 4th edition, (John Wiley and Sons, New York) (2021) 1-944.

Taberna, P.L., Simon, P., Fauvarque, J.F., 2003. Electrochemical Characteristics and Impedance Spectroscopy Studies of Carbon-Carbon Supercapacitors. J. Electrochem. Soc. 150, A292.

Tajima, S., Umehara, M., Hasegawa, M., Mise, T., Itoh, T., 2017. Cu_2ZnSnS_4 photovoltaic cell with improved efficiency fabricated by high-temperature annealing after CdS buffer-layer deposition. Prog. Photovoltaics Res. Appl. 25, 14–22.

Tanaka, T., Nagatomo, T., Kawasaki, D., Nishio, M., Guo, Q., Wakahara, A., Yoshida, A., Ogawa, H., 2005. Preparation of Cu_2ZnSnS_4 thin films by hybrid sputtering. J. Phys. Chem. Solids 66, 1978–1981.

Tanaka, T., Yoshida, A., Saiki, D., Saito, K., Guo, Q., Nishio, M., Yamaguchi, T., 2010. Influence of composition ratio on properties of Cu_2ZnSnS_4 thin films fabricated by co-evaporation, Thin Solid Films 518, 29-33.

Tang, A., Li, Z., Wang, F., Dou, M., Mao, W., 2018. Preparation of Cu_2ZnSnS_4 thin films with high carrier concentration and high carrier mobility by optimized annealing. J. Mater. Sci. Mater. Electron. 29, 7613–7620.

Temgoua, S., Bodeux, R., Naghavi, N., 2019. Influence of the annealing atmosphere and precursor's thickness on the properties of CZTSSe based solar cells. Sol. Energy Mater. Sol. Cells 191, 123–132.

Thanh, N.T.K., Maclean, N., Mahiddine, S., 2014. Mechanisms of nucleation and growth of nanoparticles in solution. Chem. Rev. 114, 15, 7610–7630.

Thota, N., Gurubhaskar, M., Kasi Reddy, A.C., Hema Chandra, G., Mehta, B.R., Tiwari, A., Venkata Subbaiah, Y.P., 2017. Growth and properties of Cu_2ZnSnS_4 thin films prepared by multiple metallic layer stacks as a function of sulfurization time. J. Mater. Sci. Mater. Electron. 28, 11702–11711.

Thota, N., Gurubhaskar, M., Sunil, M.A., Prathap, P., Subbaiah, Y.P.V., Tiwari, A., 2017. Effect of metal layer stacking order on the growth of Cu_2ZnSnS_4 thin films. Appl. Surf. Sci. 396, 644–651.

Todorov, T.K., Reuter, K.B., Mitzi, D.B., 2010. High-Efficiency Solar Cell with Earth-Abundant Liquid-Processed Absorber. Adv. Mater. 22, E156–E159.

Todorov, T.K., Tang, J., Bag, S., Gunawan, O., Gokmen, T., Zhu, Y., Mitzi, D.B., 2013. Beyond 11% Efficiency: Characteristics of State-of-the-Art $Cu_2ZnSn(S,Se)_4$ Solar Cells. Adv. Energy Mater. 3, 34–38.

Tumbul, A., Aslan, F., Goktas, A., Zarbali, M.Z., Kilic, A., 2021. Highly stable ethanol-based Cu_2ZnSnS_4 (CZTS) low-cost thin film absorber: Effect of solution aging. Mater. Chem. Phys. 258, 123997.

Tung, R.T., 2014. The physics and chemistry of the Schottky barrier height. Appl. Phys. Rev. 1, 11304.

Van der pauw, 1991. A method of measuring specific resistivity and hall effect of discs of arbitrary shape, in: semiconductor devices: pioneering papers.

Von Hauff, E., 2019. Impedance Spectroscopy for Emerging Photovoltaics. J. Phys. Chem. C 123, 11329–11346.

Wallace, S. K., Mitzi, D. B., Walsh, A., 2017. The Steady Rise of Kesterite Solar Cells. ACS Energy Lett. 2, 776-779.

Wang, L., Hu, P., Long, Y., Liu, Z., He, X., 2017. Recent advances in ternary two-dimensional materials: Synthesis, properties and applications. J. Mater. Chem. A.

Wang, W., Wang, G., Chen, G., Chen, S., Huang, Z., 2017. The effect of sulfur vapor pressure on Cu_2ZnSnS_4 thin film growth for solar cells. Sol. Energy 148, 12–16.

Wang, W., Winkler, M.T., Gunawan, O., Gokmen, T., Todorov, T.K., Zhu, Y., Mitzi, D.B., 2014. Device Characteristics of CZTSSe Thin-Film Solar Cells with 12.6% Efficiency. Adv. Energy Mater. 4, 1301465.

Wang, X., Xie, J., Li, C.M., 2014. Architecting smart "umbrella" Bi_2S_3/rGO-modified TiO_2 nanorod array structures at the nanoscale for efficient photoelectrocatalysis under visible light. J. Mater. Chem. A 3, 1235–1242.

Wasa, K., Kitabatake, M., & Adachi, H. (2004). Thin film materials technology: sputtering of control compound materials. Springer Science & Business Media.

Weber, A., Mainz, R., Schock, H.W., 2010. On the Sn loss from thin films of the material system Cu–Zn–Sn–S in high vacuum. J. Appl. Phys. 107, 13516.

Wei, Y., Zhuang, D., Zhao, M., Gong, Q., Sun, R., Ren, G., Wu, Y., Zhang, L., Lyu, X., Peng, X., Wei, J., 2019. An investigation on the relationship between open circuit voltage and grain size for CZTSSe thin film solar cells fabricated by selenization of sputtered precursors. J. Alloys Compd. 773.

Werner, J.H., Güttler, H.H., 1991. Barrier inhomogeneities at Schottky contacts. J. Appl. Phys. 69, 1522–1533.

Winnicki, M., Baszczuk, A., Rutkowska-Gorczyca, M., Jasiorski, M., Małachowska, A., Posadowski, W., Znamirowski, Z., Ambroziak, A., 2017. Microscopic examination of cold spray cermet Sn+In2O3 coatings for sputtering target materials. Scanning 2017.

Xie, M., Zhuang, D., Zhao, M., Li, B., Cao, M., Song, J., 2014. Fabrication of Cu_2ZnSnS_4 thin films using a ceramic quaternary target. Vacuum 101, 146–150.

Yan, C., Huang, J., Sun, K., Johnston, S., Zhang, Y., Sun, H., Pu, A., He, M., Liu, F., Eder, K., Yang, L., Cairney, J.M., Ekins-Daukes, N.J., Hameiri, Z., Stride, J.A., Chen, S., Green, M.A., Hao, X., 2018. Cu_2ZnSnS_4 solar cells with over 10% power conversion efficiency enabled by heterojunction heat treatment. Nat. Energy 39 3, 764–772.

Yan, C., Liu, F., Sun, K., Song, N., Stride, J.A., Zhou, F., Hao, X., Green, M., 2016. Boosting the efficiency of pure sulfide CZTS solar cells using the In/Cd-based hybrid buffers. Sol. Energy Mater. Sol. Cells 144, 700–706.

Yan, C., Sun, K., Liu, F., Huang, J., Zhou, F., Hao, X., 2017. Boost Voc of pure sulfide kesterite solar cell via a double CZTS layer stacks. Sol. Energy Mater. Sol. Cells 160, 7–11.

Yang, G., Li, Y.F., Yao, B., Ding, Z.H., Deng, R., Zhao, H.F., Zhang, L.G., Zhang, Z.Z., 2017. Growth of large grain-size $Cu_2ZnSn(S_xSe_{1-x})_4$ thin films by annealing precursors sputtered from a single quaternary target for solar cells application. Superlattices Microstruct. 109, 480–489.

Yang, K.-J., Sim, J.-H., Son, D.-H., Kim, D.-H., Kim, G.Y., Jo, W., Song, S., Kim, J., Nam, D., Cheong, H., Kang, J.-K., 2015. Effects of the compositional ratio distribution with sulfurization temperatures in the absorber layer on the defect and surface electrical characteristics of Cu_2ZnSnS_4 solar cells. Prog. Photovoltaics Res. Appl. 23, 1771–1784.

Yiğit Gezgin, S., Kiliç, H.Ş., 2019. Determination of electrical parameters of ITO/CZTS/CdS/Ag and ITO/CdS/CZTS/Ag heterojunction diodes in dark and illumination conditions. Opt. Quantum Electron. 51, 360.

Yoo, D., Choi, M., Heo, S.C., Kim, D., Chung, C., Choi, C., 2013. RF-magnetron sputtered kesterite Cu2ZnSnS4 thin film using single quaternary sputtering target prepared by sintering process. J. Nanosci. Nanotechnol. 13, 7734–7740.

Yoo, H., Kim, J., Zhang, L., 2012. Sulfurization temperature effects on the growth of Cu_2ZnSnS_4 thin film. Curr. Appl. Phys. 12, 1052–1057.

Yoshida, T., Yamaguchi, A., Umezawa, N., Miyauchi, M., 2018. Photocatalytic CO2 Reduction Using a Pristine Cu_2ZnSnS_4 Film Electrode under Visible Light Irradiation. J. Phys. Chem. C 122, 21695–21702.

Zhang, J., Long, B., Cheng, S., Zhang, W., 2013. Effects of sulfurization temperature on properties of CZTS films by vacuum evaporation and sulfurization method. Int. J. Photoenergy 2013, Article ID 986076, 6.

Zhao, Y., Han, X., Chang, L., Dong, C., Li, J., Yan, X., 2019. Effects of selenization conditions on microstructure evolution in solution processed $Cu_2ZnSn(S,Se)_4$ solar cells. Sol. Energy Mater. Sol. Cells 195, 274–279.

Zoppi, G., Forbes, I., Miles, R.W., Dale, P.J., Scragg, J.J., Peter, L.M., 2009. $Cu_2ZnSnSe_4$ thin film solar cells produced by selenisation of magnetron sputtered precursors. Prog. Photovoltaics Res. Appl. 17, 315–319.